NIST

National Institute of Standards and Technology
Technology Administration, U.S. Department of Commerce

NIST Technical Note 1536

Measuring the Permittivity and Permeability of Lossy Materials: Solids, Liquids, Metals, Building Materials, and Negative-Index Materials

James Baker-Jarvis
Michael D. Janezic
Bill F. Riddle
Robert T. Johnk
Pavel Kabos
Christopher L. Holloway
Richard G. Geyer
Chriss A. Grosvenor

NIST Technical Note 1536

Measuring the Permittivity and Permeability of Lossy Materials: Solids, Liquids, Metals, Building Materials, and Negative-Index Materials

James Baker Jarvis
Michael D. Janezic
Bill F. Riddle
Robert T. Johnk
Pavel Kabos
Christopher L. Holloway
Richard G. Geyer
Chriss A. Grosvenor

Electromagnetics Division
National Institute of Standards and Technology
Boulder, CO 80305

February 2005

Certain commercial entities, equipment, or materials may be identified in this document in order to describe an experimental procedure or concept adequately. Such identification is not intended to imply recommendation or endorsement by the National Institute of Standards and Technology, nor is it intended to imply that the entities, materials, or equipment are necessarily the best available for the purpose.

Contents

1. Introduction

Many materials used in electromagnetic applications are lossy. The accurate measurement of lossy dielectric materials is challenging since many resonant techniques lose sensitivity when applied to such materials and transmission-line methods are strongly influenced by metal losses. Our goal is to assemble the relevant information needed to perform and interpret dielectric measurements on lossy materials in a single report. Therefore we include sections on the underlying electromagnetics, circuit theory, related physics, measurement algorithms, and uncertainty analysis. We also have included a section on dielectric measurement data we have collected on a wide selection of lossy materials, including building materials, liquids, and substrates. This report should aid in the selection of the most relevant methods for particular applications. With emphasis on metrology, we will introduce the relevant electromagnetic quantities, overview a suite of measurements and methods, develop the relevant equations from first principles, and finally include the uncertainties in the measurement processes.

There is a continual demand for accurate measurements of the dielectric and magnetic properties of lossy solids and liquids [1]. Typical applications range from dielectric measurements of biological tissues for cancer research, building materials, negative index materials, electromagnetic shielding, to propagation of wireless signals. In this report, the term **loss** will refer to materials with loss tangents greater than approximately 0.05.

Measurements without well-characterized uncertainties are of dubious value. Variations in the repeatability of the measurement are not sufficient to characterize the total uncertainty in the measurement. Therefore, in this report, we pay particular attention to uncertainty analysis.

Over the years, there has been an abundance of methods developed for measuring electromagnetic permeability and permittivity. These techniques include free-space methods, open-ended coaxial-probe techniques, cavity resonators, dielectric-resonator techniques, and transmission-line techniques. Each method has its niche. For example, techniques based on cavities are accurate, but not broadband, and are usually limited to low-loss materials. Nondestructive techniques, although not the most accurate, are very attractive since they

maintain material integrity.

Dielectric properties depend on frequency, homogeneity, anisotropy, temperature, surface roughness, and in the case of ferroelectrics and ferromagnetics, applied bias field [2,16]. Field orientation is important for measurements of anisotropic materials. Measurement fixtures where the electromagnetic fields are tangential to the air-material interfaces, such as in TE_{01} cavities, generally yield more accurate results than fixtures where the fields are normal to the interface. Unfortunately, for many applications it is not always possible or even preferable to measure in-plane field orientations. For example, circuit boards and printed-wiring boards operate with the electric field primarily normal to the plane of the panel and therefore this component of the permittivity is of paramount interest. However, measurements with the electric field perpendicular to the specimen face may suffer from the effects of air-gap depolarization. Air gaps around the electrodes in transmission-line measurements produce a large systematic uncertainty since they introduce a series capacitance that results in a severe bias in the calculated permittivity. In cases such as in coaxial matched-load termination measurements, the effects of air gaps can be reduced by metalization of the specimen surfaces or application of conductive pastes to the sections of the specimen in contact with the electrodes; otherwise they may be corrected by numerical techniques [3,4]. The characterization of anisotropic materials generally requires two techniques, one for the normal component of permittivity and one for the in-plane component. However, the loss measurement is usually not strongly anisotropic and one accurate measurement usually suffices.

In recent years, research into negative index materials (NIM) has increased. These lossy materials support negative permittivity and permeability over narrow-bands of frequencies. In this report we will address a number of metrology issues related to this field of study.

We begin with an overview of relevant electrical parameters in Section 2 and with an overview of constitutive relationships and the local, applied, evanescent, and macroscopic fields in Section 3. We then discuss calibration issues, sample holders, and sample preparation in Section 4. Next, we proceed with an overview of measurement methods in Section 5 and transmission-line methods in Sections 6 through 8. Some of this was given in Reference [1], but we have rewritten this for lossy materials. We then overview the measurement of the

permeability and resistivity of ferrites and metals in Section 9. In Section 10 we discuss two-port and short-circuited coaxial probes. Liquid measurement methods are overviewed in section 11. Finally, we overview the measurement of phantom and biological tissues in Section 12.

2. Electrical Properties of Lossy Materials

2.1 Electromagnetic Concepts for Lossy Materials

In this section, we overview the most basic concepts needed to study and interpret dielectric response in lossy materials. We use the following notation for the permittivity, $\epsilon^* = \epsilon_0(\epsilon_r' - j\epsilon_r'')$, where $\epsilon_0 = 8.85 \times 10^{-12}$ (F/m) is (approximately) the permittivity of vacuum and $\tan \delta_d = \epsilon_r''/\epsilon_r'$ is the loss tangent in the material. A similar relationship holds for the permeability, $\mu^* = \mu_0(\mu_r' - j\mu_r'')$, where $\mu_0 = 4\pi \times 10^{-7}$ (H/m) is the (exact) permeability of vacuum and the magnetic loss tangent is $\tan \delta_m = \mu_r''/\mu_r'$.

In the time domain, the most general causal linear relationship between the displacement and electric fields is

$$\mathbf{D}(\mathbf{r}, t) = \epsilon_0 \mathbf{E}(\mathbf{r}, t) + \int_0^\infty f(\tau)\mathbf{E}(\mathbf{r}, t - \tau)d\tau, \tag{1}$$

where f is the impulse-response function. The permittivity is defined in terms of the Fourier transform of the impulse-response function $\epsilon(\omega) = \epsilon_o(1 + \mathcal{F}[f](\omega))$. An analogous equation can be written between the induction and magnetic fields.

Electric and magnetic fields are attenuated as they travel through lossy materials. The plane-wave attenuation coefficient in an infinite medium is denoted by the quantity α and the phase by β. The propagation coefficient is $\gamma = \alpha + j\beta = jk = j\omega\sqrt{\epsilon\mu}$. For waves in a guided structure $\gamma = j\sqrt{k^2 - k_c^2}$, where $k_c = \omega_c/c = 2\pi/\lambda_c$ is the cutoff wave number. The attenuation is given by

$$\alpha = \frac{\omega}{\sqrt{2}c}\sqrt{\epsilon_r'\mu_r'}\sqrt{\left((\frac{k_c^2}{k_r^2} - 1 + \tan \delta_d \tan \delta_m)^2 + (\tan \delta_d + \tan \delta_m)^2\right)^{1/2} + \frac{k_c^2}{k_r^2} - 1 + \tan \delta_d \tan \delta_m}, \tag{2}$$

where $k_r = \omega\sqrt{\epsilon'\mu'}$. In a dielectric medium where $k_c \to 0$, we have

$$\alpha = \frac{\omega}{c\sqrt{2}}\sqrt{\epsilon'_r\mu'_r}\sqrt{\sqrt{1+\tan^2\delta_d}-1}. \tag{3}$$

In low-loss dielectric media, $\tan_d\delta \ll 1$, α reduces in the limit to $\alpha \to \omega\sqrt{\epsilon'_r\mu'_r}(\tan\delta_d)/2c$. The phase coefficient β is given by

$$\beta = \pm\frac{\omega}{\sqrt{2}c}\sqrt{\epsilon'_r\mu'_r}\sqrt{\left((\frac{k_c^2}{k_r^2}-1+\tan\delta_d\tan\delta_m)^2+(\tan\delta_d+\tan\delta_m)^2\right)^{1/2}-(\frac{k_c^2}{k_r^2}-1+\tan\delta_d\tan\delta_m)}. \tag{4}$$

Note that at cutoff, β is a function only of the loss factors. In dielectric media this reduces to

$$\beta = \pm\frac{\omega}{c\sqrt{2}}\sqrt{\epsilon'_r\mu'_r}\sqrt{\sqrt{1+\tan^2\delta_d}+1}. \tag{5}$$

The imaginary part of the propagation coefficient defines the phase of an electromagnetic wave and is related to the refractive index $n = \pm\sqrt{\epsilon'_r\mu'_r}$. In normal dielectrics the positive square root is taken in eq. (4). In NIM, which have effective negative ϵ'_r and μ'_r, we take negative square root in eq. (4). This is the origin of the term NIM. This keeps the real part of the wave impedance positive. The wave impedance for a transverse electric and magnetic mode (TEM) is $\sqrt{\mu/\epsilon}$, transverse electric mode (TE) is $j\omega\mu/\gamma = \mu\omega(\beta+j\alpha)/(\beta^2+\alpha^2)$, and for a transverse magnetic mode (TM) is $\gamma/j\omega\epsilon$. As a consequence of conservation of energy, α must positive. Below cutoff the propagation coefficient becomes $\gamma = \sqrt{k_c^2-k^2}$, since a factor of j is factored out from under the square root.

The wavelength in a material is influenced by the permittivity; for example, for a TEM mode, $\lambda_m \approx c_{vac}/\sqrt{\epsilon'_r\mu'_r}f$.

The skin depth, the distance a plane wave travels where it decays to $1/e$ of the initial amplitude, is related to the attenuation coefficient by $\delta_s = 1/\alpha$. The wave amplitude decays due to losses as $|\mathbf{E}| \propto \exp(-\alpha z)$. The power in a plane wave, $E(z,t) = E_0\exp(-\alpha z)\exp(j\omega t - j\beta z)$, attenuates as $P \propto \exp(-2\alpha z)$. In metals, where the conductivity is large, the skin depth reduces to

$$\delta_s = \frac{1}{\sqrt{\pi f\mu_0\mu'_r\sigma_{dc}}}, \tag{6}$$

5

where σ_{dc} is the dc conductivity and f is the frequency. We see that the frequency, conductivity, and permeability of the material determine the skin depth in metals. The surface resistance for metal is

$$R_s = \frac{1}{\delta_s \sigma_{dc}} = \sqrt{\frac{\pi f \mu_0 \mu_r'}{\sigma_{dc}}}. \tag{7}$$

When the conductors on a substrate are very thin, the fields can penetrate through the conductors into the substrate. This increases the resistance because the field is in both the metal and the dielectric. As a consequence of the skin depth, the internal inductance decreases with increasing frequency, whereas the surface resistance R_s increases with frequency in proportion to $\sqrt{\omega}$.

Some materials exhibit ionic conductivity, so that when a static (dc) electric field is applied, a current is induced. This behavior is modeled by the dc conductivity σ_{dc}, which produces a low-frequency loss ($\propto 1/\omega$) in addition to polarization loss (ϵ_r''). In some materials, such as semiconductors and disordered solids, the conductivity is complex and is frequency dependent. This will be discussed in Section 2.3.

The effective permittivity for linear, isotropic materials, that includes dc conductivity is defined from the Fourier transform of Maxwell's equation: $j\omega \mathbf{D} + \mathbf{J} \equiv j\omega\epsilon\mathbf{E} + \sigma_{dc}\mathbf{E} \equiv j\omega\epsilon_{eff}^*\mathbf{E} = \nabla \times \mathbf{H}$, so that

$$\epsilon_{eff}^* = \epsilon_r'\epsilon_0 - j(\epsilon_r''\epsilon_0 + \frac{\sigma_{dc}}{\omega}). \tag{8}$$

The group velocity in a transmission line of length L is

$$v_g = \frac{\partial \omega}{\partial \beta} = -L/\frac{\partial \phi}{\partial \omega} = \frac{c}{n + \omega\frac{\partial n}{\partial \omega}}, \tag{9}$$

where n is the index of refraction, ϕ is the phase, and the group delay is $-\frac{\partial \phi}{\partial \omega}$. For anomalous dispersion such as in NIM the index of refraction becomes negative, predicting a group velocity faster than c. This result is traced to the approximations made in deriving eq. (9) and a detailed anlaysis shows this is no longer a problem. The phase velocity is defined from the definition of a constant phase $\theta = \omega t - \beta z$ so that the time derivative yields

$$\frac{dz}{dt} = v_p = \frac{\omega(k)}{\beta} = \frac{c}{n(k)}. \tag{10}$$

Waves where the group and phase velocity are in the same direction are called forward waves. If they are opposite in sign then they are called backward waves as shown in Figure 1. Backward waves occur in regions of strong dispersion such as in NIM materials near resonant frequencies where the effective permittivity and permeability can become negative. A typical backward wave may have anomalous dispersion of the form $\omega^2 = 1/k^2 \mathcal{L}C$, with phase velocity $\omega/k = 1/k^2\sqrt{\mathcal{L}C}$, and group velocity $d\omega/dk = -1/k^2\sqrt{\mathcal{L}C}$. NIM are formed by resonant structures embedded in a matrix, which form regions where the effective permittivity and permeability become negative at specific frequencies. The derivative of the refractive index in eq. (9) is needed in calculating the behavior of backward waves. The effective permittivity and permeability of resonant systems and backward waves can be characterized by harmonic oscillators. Since the polarization satisfies the driven harmonic oscillator proble and $\mathbf{P}(\omega) = \chi\mathbf{E} = (\epsilon(\omega) - 1)\mathbf{E}$, we have

$$\epsilon(\omega) = \epsilon_0 \left(C_1 + \frac{\omega_e^2}{\omega_{oe}^2 - \omega^2 + j\Gamma_e\omega} \right) \tag{11}$$

$$\mu(\omega) = \mu_0 \left(C_2 + \frac{\omega_m^2}{\omega_{om}^2 - \omega^2 + j\Gamma_m\omega} \right), \tag{12}$$

where the constants are determined by fits to the resonance curve. In the special case where $\epsilon_r = \mu_r = -1$, Pendry and Maslovski et al. [90] have conjectured that nearly perfect-lens properties are possible. Using the effective permittivity and permeability in the form of eqs. (11) and (12), the the dispersion relations, phase, and group velocities can be obtained.

2.2 Overview of Relevant Circuit Theory

The phase velocity in a transmission line with distributed capacitance C and inductance $\mathcal{L}$ is given by $v_p = \omega/\beta$. At cutoff the phase velocity becomes infinite (whereas the physical speed, $v_g \leq c$). For a uniform lossless line, $v_p = 1/\sqrt{\mathcal{L}C}$. For a lossy line

$$v_p \approx \frac{1}{\sqrt{\mathcal{L}C}} \frac{1}{1 - \frac{R^2}{8\omega^2\mathcal{L}^2}}. \tag{13}$$

Therefore, because of the relationship between $\epsilon \leftrightarrow C$ and $\mu \leftrightarrow \mathcal{L}$, the propagation velocity varies as a function of the permittivity, permeability, and frequency. In lossy low-temperature

7
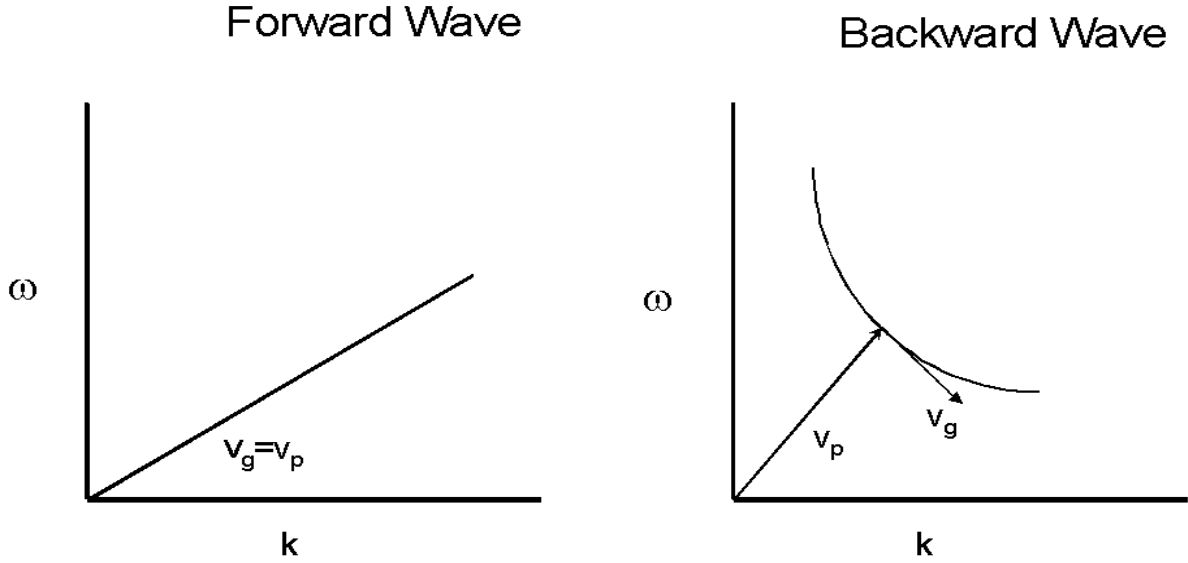
Figure 1. Forward and backward wave dispersion curves.

co-fired ceramics (LTCC) and printed wiring board (PWB) applications signals with high harmonic content, such as pulsed waveforms, will exhibit dispersion as they propagate along the line. The propagation delay per unit length found from eq. (13) is $t_d \approx \sqrt{\mathcal{L}C}(1 - R^2/(8\omega^2\mathcal{L}^2))$.

The characteristic impedance of a transmission line is given by $[5,6]$

$$Z_C = \sqrt{\frac{R + j\omega\mathcal{L}}{G + j\omega C}}, \tag{14}$$

where G is the conductance, $\omega = 2\pi f$, and $\mathcal{L}$ and R are the distributed inductance and resistance that may be frequency dependent. For a TEM transmission line this would reduce the characteristic impedance to $\sqrt{\mu/\epsilon}$. The capacitance C for low-loss dielectrics depends very weakly on frequency. The reason $\mathcal{L}$ is a function of frequency is that it can be expressed as $\mathcal{L} = \mathcal{L}_{int} + \mathcal{L}_{ext}$, where $\mathcal{L}_{int}$ is the internal self inductance of the conductors and $\mathcal{L}_{ext}$ is the external inductance between the conductors. R and $\mathcal{L}_{int}$ depend on the skin depth.

8

In an ideal lossless transmission line at typical wireless frequencies, we can approximate eq. (14) as

$$Z_{c(ideal)} \approx \sqrt{\frac{\mathcal{L}}{C}} \Leftrightarrow \sqrt{\frac{\mu}{\epsilon}}. \tag{15}$$

In eq. (15) the characteristic impedance of the lossless transmission line is real and depends only on $\mathcal{L}$ and C. Z_c can be complex [7,8]. An approximation for the characteristic impedance at high frequencies can be obtained by a Taylor-series expansion in R. Assuming $G = 0$,

$$Z_c \approx \sqrt{\frac{\mathcal{L}}{C}} \left[1 - j \frac{R}{2\omega\mathcal{L}} + \frac{R^2}{8\omega^2\mathcal{L}^2} \right]. \tag{16}$$

The propagation coefficient γ is also important in transmission-line performance because it describes the attenuation and phase response of the line

$$\gamma = \alpha + j\beta = \sqrt{(R + j\omega\mathcal{L})(G + j\omega C)} \approx \frac{R}{2Z_0} + j\omega\sqrt{\mathcal{L}C} \left[1 - \frac{R^2}{8\omega^2\mathcal{L}^2} \right], \tag{17}$$

where $C, G, \mathcal{L}, R$ are measured distributed circuit parameters per unit length. The last expression in eq. (17) is a Taylor-series expansion of γ with $G = 0$ in powers of R. In eq. (17), α and β are the attenuation and phase coefficients, where α includes loss due to the conductors, dielectric, and radiation: $\alpha = \alpha_c + \alpha_d + \alpha_r$. Here, α_c can be approximated by [6]

$$\alpha_c = \frac{R(\omega)}{2Z_{c(ideal)}}. \tag{18}$$

Equation (18) is very approximate, and in microstrip, stripline, coplanar and other waveguides, there are significant corrections [9]. The dielectric attenuation is

$$\alpha_d = \frac{\omega}{2} \sqrt{\frac{\mu_0\mu_r'}{\epsilon_0\epsilon_r'}} \epsilon_r'' = \frac{\omega}{2} \sqrt{\epsilon_0\epsilon_r'\mu_0\mu_r'} \tan\delta_d. \tag{19}$$

Note that α_d increases linearly with frequency, whereas α_c increases as the square root of frequency. The bulk dc resistance is given by

$$R_{dc} = \frac{1}{\sigma_{dc}} \frac{L_e}{A_e}, \tag{20}$$

where L_e and A_e are the length and effective area of the conductor where the current passes. Using eq. (6), we see that resistance increases with frequency, approximately as $R \approx R_{dc} + R_f\sqrt{f}$, where R_f is the increment of the alternating current (ac) resistance per square root

Table 1. Conductivities of metals. The skin depths are for 10 GHz.

Material	Conductivity, $\sigma_{dc}/10^7$(S/m)	Skin depth $\delta \times 10^7$(m)
Cu	5.80	6.60
Al	3.72	8.26
Ag	6.17	6.42
Au	4.10	7.85
In	0.87	17.0
70-30 brass	1.57	12.70
Typical solder	0.71	19.0

Table 2. Resistivities of metals [10, 11].

Material	Cu	Ag	Au	Mo	Pb	Al	Sn	Pd	Pt
Bulk resistivity ($\mu\Omega\cdot$ cm)	1.7	1.6	2.3	5.2	20.6	2.65	11	10.8	10.6
Thick-film resistivity ($\mu\Omega\cdot$ cm)	4	5	5	12	-	-	-	-	-
Maximum temperature (^{o}C)	950	950	950	1500	327	660	230	1550	1768

of frequency from dc. Bulk electrical conductance and resistivity of commonly used metals are given in tables 1 and 2 [5].

The conductance G of the transmission line depends on the loss in the dielectric substrate. At low gigahertz frequencies or below, these losses are smaller than conductor losses. However, the dielectric losses increase roughly in proportion to ω or faster, as given in eq. (19), whereas conductor losses increase as $\sqrt{\omega}$. Therefore, at high frequencies, above approximately 10 GHz to 30 GHz, the dielectric loss can exceed metal losses. This is a reason why low-loss substrates are used at high frequencies.

The dielectric and magnetic loss tangents can in some cases be expressed in terms of circuit parameters and frequency f: $\tan \delta_d = G/(2\pi f C)$. For magnetic materials the effective loss tangent is $\tan \delta_m = R/(2\pi f \mathcal{L})$.

Lossy dielectric and magnetic materials are dispersive. As a consequence, $\partial u/\partial t = \mathbf{E} \cdot \partial \mathbf{D}/\partial t + \mathbf{H} \cdot \partial \mathbf{B}/\partial t \neq 1/2(\epsilon \partial |\mathbf{E}|^2/\partial t + \mu \partial |\mathbf{H}|^2/\partial t)$. The energy stored in a dispersive material is [12]

$$u_{eff} = Re\left(\frac{d(\omega\epsilon)}{d\omega}(\omega_0)\right) < \mathbf{E}(\mathbf{r},t) \cdot \mathbf{E}(\mathbf{r},t) > + Re\left(\frac{d(\omega\mu)}{d\omega}(\omega_0)\right) < \mathbf{H}(\mathbf{r},t) \cdot \mathbf{H}(\mathbf{r},t) > . \quad (21)$$

The time average $<>$ is over the period of the carrier frequency ω_0. Equation (21) reduces to the normal stored-energy expression when the material parameters are independent of frequency; also, in this limit $u_{eff} = u$. The conservation of internal equation u_{eff}, for the Poynting vector $\mathbf{S} = \mathbf{E} \times \mathbf{H}$ in linear, dispersive media is given by

$$\frac{\partial u_{eff}}{\partial t} + \nabla \cdot \mathbf{S} = -\mathbf{J} \cdot \mathbf{E} - 2\omega_0 Im[\epsilon(\omega_0) < \mathbf{E} \cdot \mathbf{E} > + \mu(\omega_0) < \mathbf{H} \cdot \mathbf{H} >]. \quad (22)$$

2.3 DC and AC Conductivity

The alternating current (ac) conductivity $\sigma_{tot}^* \equiv \sigma_{dc} + j\omega(\epsilon(\omega) - \epsilon_0)$ has been used in the literature to model either the ac effects of the free charge and partially bound free charge in hopping and tunneling conduction, or as another way of expressing the complex permittivity. Since some charge is only partially bound, the distinction between conductivity and permittivity can, at times, get blurred. This is particularly an issue in quantum-mechanical

analysis where energy states are discrete. In this section we consider the ac complex conductivity $\sigma_{tot}^* = \sigma' - j\sigma''$ of the free, bound, and partially bound charge. Most models of ac conductivity are based on charged particles in potential wells, yielding a percolation threshold, where energy fluctuations determine whether the particle can surmount the barrier and thereby contribute to the conductivity.

Semiconductors are materials where ac conductivity is commonly used. Gallium arsenide and gallium nitride are highly insulating and therefore have less loss. Figures 2 and 3 show measurement results on the permittivity of high-resistivity gallium arsenide as a function of frequency. These measurements were made by a mode-filtered TE_{01} X-band cavity. As the frequency of measurement increases to the gigahertz range, the free-charge loss in many semiconductors decreases. At high frequencies, lossy semiconductors and metals have a complex free-charge ac conductivity, explained by the Drude model. This can cause the effective permittivity to be negative [12]. To understand this, consider Maxwell's equation

$$\frac{\partial \mathbf{D}}{\partial t} + \mathbf{J} = \nabla \times \mathbf{H}. \tag{23}$$

Usually the constitutive relations for the free-current density and displacement are $\mathbf{J} = \sigma \mathbf{E}$ and $\mathbf{D} = \epsilon \mathbf{E}$, where σ is the conductivity due to the motion of free charge and not the bound-charge polarization, either through ionic movement, hopping, or tunneling phenomena. As frequency increases the conductivity can be complex, where the real part is approximately the dc conductivity and the imaginary part relates to the phase of the charge movement. Combining σ_{dc} with the displacement field produces an effective real part of the permittivity that can be negative over a region of frequencies

$$\epsilon_{eff(r)} = \epsilon_r' - \frac{\sigma''}{\epsilon_0 \omega} - j\left(\epsilon_r'' + \frac{\sigma'}{\epsilon_0 \omega}\right), \tag{24}$$

where $\sigma' \approx \sigma_{dc}$.

There are a number of distinct models for σ_{tot}^*. The Drude model for the complex conductivity of metals results in $\sigma_{tot}^* = f_0 N e^2 / (m(\gamma_0 + j\omega)) = \sigma' - j\sigma''$, where γ_0 is the collision frequency, $f_0 N$ is the electron density, m is the ion mass, and e is the electronic charge [12]. Note that the dc conductivity is $\sigma_{dc} = f_0 N e^2 / m\gamma_0$. The net dielectric response is a sum of
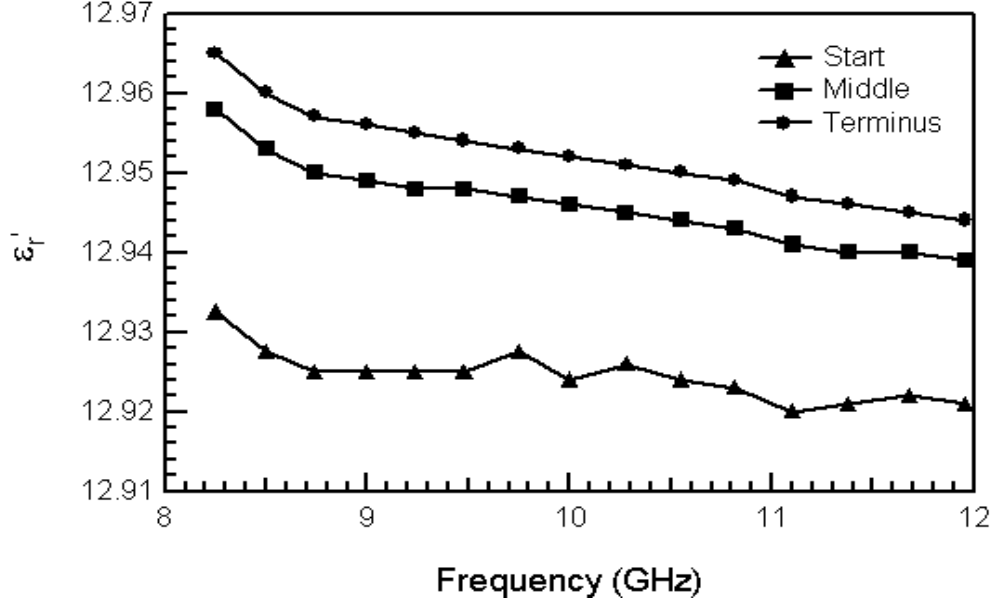
Figure 2. ϵ'_r of gallium arsenide measured by an X-band cavity [13]. Start, middle, and terminus refer to different specimens taken from the same boule.

the dipolar contribution and that due to the ions where $\epsilon' = \epsilon'_1 - f_0 Ne^2/m(\gamma_0^2 + \omega^2)$, and $\epsilon'' = Ne^2\gamma_0/m\omega(\gamma_0^2 + \omega^2)$. Therefore, for metals, the real part of the permittivity is negative for frequencies near the plasma frequency, $\omega_p = \sqrt{f_0 Ne^2/\epsilon_0 m}$. The plasma frequency in metals is usually well above 100 GHz; in gases it can be lower since the density of charged particles is lower.

For disordered solids, where hopping and tunneling conduction takes place with a relaxation time τ_e, the ac conductivity can be expressed as [14, 15]

$$\sigma^*_{tot}(\omega) = \sigma_0 j\omega\tau_e / \ln(1 + j\omega\tau_e)$$
$$= \sigma_0 \left[\frac{\omega\tau_e \arctan(\omega\tau_e)}{\frac{1}{4}\ln^2(1 + \omega^2\tau_e^2) + \arctan^2(\omega\tau_e)} - j\frac{\omega\tau_e \ln(1 + (\omega\tau_e)^2)}{\frac{1}{2}\ln^2(1 + \omega^2\tau_e^2) + 2\arctan^2(\omega\tau_e)} \right]. \quad (25)$$

For complex conductivity the combination of permittivity and conductivity in ϵ_{eff} satisfies the Kramers-Kronig causality condition. In Section 5, we discuss the Kramers-Kronig relation with dc conductivity included.

13
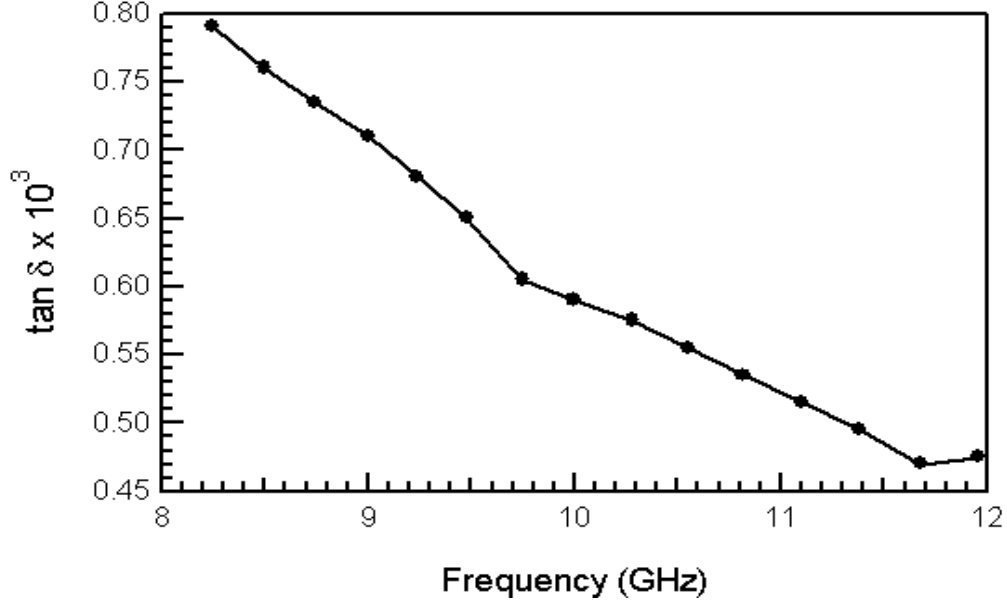
Figure 3. Loss tangent of gallium arsenide measured by an X-band cavity [13].

3.   Applied, Macroscopic, Evanescent, and Local Fields

In this section, we overview a number of pertinent concepts used in dielectric analysis. This includes the electromagnetic fields in materials, field behavior, NIM materials, and types of material property averaging in disordered solids.

3.1   Microscopic, Local, Evanescent, and Macroscopic Fields

If an electromagnetic field is applied to a semi-infinite media, the fields in the material include the effects of both the applied field and the particle back-reaction fields. The charges and spins in a medium interact with the local fields and not necessarily with the total applied field. For example, when an applied electromagnetic field interacts with a dielectric material, the macroscopic and local fields in the material are modified by surface-charge dipole-depolarization fields that oppose the applied field. When considering time-dependent high-frequency fields, this interaction is more complex. In addition, the internal energy affects the resulting electromagnetic behavior. For example, depolarization, demagnetization, thermal expansion, exchange, and anisotropy interactions can influence the dipole orientations and therefore the fields. Usually these effects of internal energy are modeled by an

14

effective field that modifies the applied field. In constitutive modeling in Maxwell's equations, we must express the material properties in terms of the macroscopic field, not the applied or local fields and therefore we need to make clear distinctions between the fields [16].

Fields may be propagating, of form $e^{j(\omega t - \beta z)}$, damped propagating $e^{j(\omega t - \beta z) - \alpha z}$, or evanescent $e^{j\omega t - \alpha z}$. Evanescence occurs at frequencies below cutoff, that is in a waveguide, where transverse resonance occurs [17]. Below cutoff, $\gamma = \sqrt{k_c^2 - k^2}$, where k_c is the cutoff wave number calculated from the transverse geometry and $k = \omega \sqrt{\epsilon \mu}$. Evanescent electromagnetic fields also occur at apertures and in the near fields of antennas. Near (evanescent) fields consist of stored energy and there is no net energy transport over a cycle unless there are losses in the medium. In the case of an antenna the evanescent fields are called the near field. Evanescent fields can be detected only if they are perturbed and converted into propagating waves or transformed by dielectric loss. Electromagnetic waves may convert from evanescent to propagating. For example, in coupling to dielectric resonators, the evanescent waves from the coupling loops produce propagating waves in the dielectric resonator.

The relationships between the applied, macroscopic, local, and the microscopic fields are important for constitutive modeling. The applied field originates from external charges, whereas the macroscopic fields are averaged quantities in the medium. The macroscopic fields within the material region in Maxwell's equations are implicitly defined through the constitutive relationships and boundary conditions. The macroscopic field that satisfies Maxwell's equations with appropriate boundary conditions and constitutive relationships is generally not the same as the applied field. The macroscopic field is approximately the applied field minus the field due to surface depolarization. In a homogeneous, semi-infinite slab, illuminated by an applied field, the macroscopic field is generally of smaller magnitude than the applied field. The local field is the averaged electromagnetic field at a particle site due to both the applied field and the fields from all of the other sources, such as dipoles [18, 19]. The microscopic field represents the atomic-level electromagnetic field where particles interact with the field from discrete charges. At the first level of homogenization, particles interact with the local electromagnetic field. The spatial and temporal resolution contained in the macroscopic variables are directly related to the spatial and temporal detail incorporated

15

in the material parameters obtained when the charge density is homogenized and expanded in a Taylor series. If Maxwell's equations are solved precisely at the microscale level with exact constitutive relationships, then the macroscopic electromagnetic field is the same as the microscopic field.

Theoretical analysis of the effective local electromagnetic field is important in dielectric modeling of single-molecule measurements and thin films, since at this level we need to know some, but not all, the details of the molecular structure. The electromagnetic fields at this level are local, but not atomic scale. Since electrical measurements can now be performed to very small spatial resolutions and the elements of electrical circuits approach the molecular level, we require good models of the macroscopic and local fields at all spatial scales. This is particularly important since we know that the Lorentz theory of the local field is not always adequate for predicting polarizabilities [20, 21]. Also, when solving Maxwell's equations at the molecular level, definitions of the macroscopic field and constitutive relationships are important. The formation of the local field is a very complex process whereby the applied electric field polarizes dipoles in a specific molecule and the applied magnetic field causes precession of spins. Then the molecule's dipole field modifies the dipole orientations of other molecules in close proximity, which then reacts back to produce a correction to the molecule's field in the given region. This process gets more complicated for time-dependent behavior. We define the local electromagnetic field as the effective, averaged field at a specific point in a material, which is a function of both the applied and multipole fields in the media. The local field is related to the average macroscopic and microscopic electromagnetic fields in that it is a sum of the macroscopic field and effects of the near-field. In ferroelectric materials, the local electric field can become very large and hence there is a need for comprehensive field models.

Mandel and Mazur developed a static theory for the local field in terms of the polarization response of a many-body system using a T-matrix formalism [22]. Gubernatis extended the T-matrix formalism [23]. Keller's [24] review article on the local field uses an electromagnetic propagator approach. Kubo's linear-response theory has also been used for electromagnetic correlation studies [18, 25].

16

In the literature of dielectric materials, a number of specific fields have been introduced to analyze polarization phenomena. The electric field acting on a nonpolar dielectric is commonly called the internal field, whereas the field acting on a permanent dipole moment is called the directing field. The difference between the internal field and directing fields is the averaged reaction field. The reaction field is the result of a dipole polarizing its environment.

Electromagnetic fields in materials can either be freely propagating, propagating with attenuation, or evanescent. At a macroscopic level the effects of the material are modeled by an effective permittivity and permeability. The formation of the permittivity or permeability from the basic charges and atoms can be modeled using a complicated statistical-mechanical averaging procedure that contains microstructural effects. However, in general the constitutive modeling is less ambitious and places the microstructural effects into the definition of the impulse-response function in the time domain or the permittivity and permeability in the frequency domain. In nonhomogeneous random composite materials the modeling of the permittivity depends on whether the wavelength in the material is long or short relative to material inclusions. In long wavelength approximations, the material can be modeled with an effective permittivity and permeability. If there is a periodicity in composite materials, then the electromagnetic propagation will manifest this in the scattering response and there may be band gaps. If the applied field has a wavelength short in relation to particle size then the material parameters are spatially dependent and resonances can occur in the inclusions.

If resonances occur in the medium, then the effective real parts of the permittivity and permeability can exhibit anomalous behavior; for example, they may obtain negative values (see eqs. (11) and (12)). If only the effective permittivity or permeability have negative values, then evanescent fields are produced, analogous to fields below cutoff in a waveguide [26].

Evanescent and near fields in dielectric measurements are very important. These fields do not propagate and therefore can be used to measure materials of very small spatial dimensions; for example, in evanescent microwave probing [27].

The various types of wave propagation in heterogeneous materials are summarized in Figure 4. Region 1 in Figure 4 corresponds to the quasistatic region. This implies low
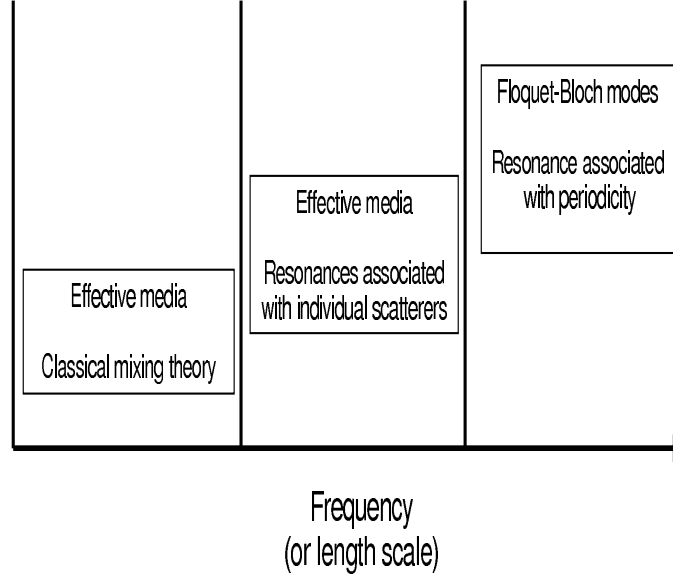
Figure 4. Length scales in effective medium.

frequencies or, more importantly, frequencies where the wavelength is much larger then the periodicity of the scatterers that compose the composite media. These scatterers may possess induced or permanent dipole moments, as is the case for atoms or molecules of classical materials, or these scatterers could be generic in shape and placed in a host matrix to obtain a man-made composite material having some desired property. Using asymptotic techniques we can show that the electromagnetic field, in the low-frequency limit, behaves as if the composite material is an equivalent effective medium with homogenous material properties. The effective materials properties are derived from a quasistatic solution of the periodic structure. The basic result is that the effective permittivity is obtained by taking a ratio of some averaged displacement field to an averaged electric field. The effective permeability is obtained by taking a ratio of some averaged induction field to an averaged magnetic field. Region 2 in Figure 4 corresponds to a region where the scatterers are designed in such a manner such that the scatterers themselves can resonate. This occurs in NIM materials. In Region 3 in Figure 4, we see that as the wavelength approaches the dimensions of the inclusions, the fields no longer longer respond as in an effective medium. At these frequencies, a more complicated field behavior exists and more elaborate techniques to analyze the electromagnetic field interaction with the composite periodic structures must be used; that

18

is, usually a full-wave approach. The classical approach that is used to analyze periodic structures is the Floquet-Bloch mode approach, where the fields are expanded in an infinite sum of plane waves.

3.2   Averaging

If we consider electromagnetic wave propagation from macroscopic to molecular to submolecular scales, the effective response at each level is related to different degrees of homogenization. The wavelengths of applied fields can be comparable to particle size either for molecules, at very high frequencies, or in macroscopic composites, when the inclusion size is of the order of a wavelength. In microelectrodynamics, there have been many types of ensemble and volumetric averaging methods used to define the macroscopic fields obtained from the microscopic fields [12,22,28,29]. For example, in the most commonly used theory of microelectromagnetics, materials are averaged at a molecular level to produce effective molecular dipole moments. The microscopic electromagnetic theories developed by and Jackson, Mazur, Robinson [12,28,29] average multipoles at a molecular level and replace the molecular multipoles, with averaged point multipoles usually located at the center-of-mass position. This approach works well down to near the molecular level, but breaks down at the molecular to submolecular level. The next level is the averaging of molecular moments to produce effective dipole moments on the supramolecular scale [26].

In the different theories, the homogenized fields are formed in different ways. The averaging is always volumetric and not over time. In a number of approaches, the volumetric averaging is accomplished by convolving the unit step function with the fields. Jackson uses a truncated averaging test function to proceed from microscale to the macroscale fields [12]. Robinson and Mazur use ensemble averaging [28, 29] and statistical mechanics. Ensemble averaging assumes there is a probability that the system is in a specific state. In the volumetric averaging approach, the averaging function is never explicitly determined, but the function is assumed to be such that the averaged quantities vary in a manner smooth enough to allow a Taylor-series expansion to be performed. In the approach of Mazur, Robinson, and Jackson [12, 28, 29] the charge density is expanded in a Taylor series and the multipole

moments are identified. These moments are calculated about each molecular center of mass and are treated as point multipoles. However, this type of molecular averaging limits the scales of the theory to above the molecular level and limits the modeling of induced-dipole molecular moments [16]. Usually the averaging approach uses a test function f_t where

$$\mathbf{E} = \int d\mathbf{r}' \mathbf{e}(\mathbf{r} - \mathbf{r}') f_t(\mathbf{r}'). \tag{26}$$

However, the distribution function f_t is seldom explicitly needed or determined in the analysis. In general, this distribution function must depend on the material properties since it is the constitutive relations that determine f_t. The averaging function must also be a function of the level of homogenization used.

3.3   Constitutive Relations

In materials, Maxwell's equations are not complete until we specify the constitutive relationships between the macroscopic polarization, magnetization, and current density as functions of the macroscopic electric and magnetic fields. The relationship of the polarization, magnetization, and current density to the applied and macroscopic electric, magnetic fields can be expressed as $\{\mathbf{P}, \mathbf{M}, \mathbf{J}\} \leftrightarrow \{\mathbf{E}_a, \mathbf{H}_a\} \leftrightarrow \{\mathbf{E}, \mathbf{H}\}$ where subscript $_a$ denotes applied. The double-headed arrow in this relation indicates that the relationship could be nonlocal in time and space and the constitutive relation may be a linear or nonlinear function of the driving fields [30, 31], and contain the contributions from both the electrical and the mechanical properties such as stress-strain, as well as thermal contributions such as temperature. When used in Maxwell's equations, the displacement field $\mathbf{D}$, the induction field $\mathbf{B}$, and current density $\mathbf{J}$ must be expressed in terms of the macroscopic electromagnetic fields.

The fields and material-related quantities in Maxwell's equations must satisfy underlying symmetries. For example, the dielectric polarization and electric fields are odd under parity and even under time-reversal transformations. The magnetization and induction fields are even under parity transformation and odd under time reversal. These symmetry relationships place constraints on the nature of the allowed constitutive relationships and requires the constitutive relations to manifest related symmetries [28, 32–38]. The evolution equations

20

for the constitutive relationships need to be causal and in linear approximations must satisfy time-invariance properties.

In any complex lossy system, there is conversion of energy from one form to another; for example, electromagnetic to thermal energy through photon-phonon interactions. The coupling of electromagnetic fields to phonons, that is, lattice vibrations, is through the polariton quasiparticle. Magnetic coupling is mediated through magnons and spin waves. These effects are manifest in the constitutive relations and the resultant permittivity and permeability.

Fields $\mathbf{E}$ and $\mathbf{B}$ have been well established as the fundamental electromagnetic fields, which originate from charge and spin. However, when free charge is present, there are both free and bound currents, and we feel it is more instructive to deal with $\mathbf{E}$ and $\mathbf{H}$ as fields that drive $\mathbf{D}$ and $\mathbf{B}$. This approach separates the free-charge current density ($\mathbf{J}$) from the bound-charge current density ($\partial \mathbf{P}/\partial t$).

The macroscopic displacement and induction fields $\mathbf{D}$ and $\mathbf{B}$ are related to the macroscopic electric field $\mathbf{E}$ and magnetic fields: $\mathbf{H}$, $\mathbf{M}$, and $\mathbf{P}$ by

$$\mathbf{D} = \epsilon_0 \mathbf{E} + \widetilde{\mathbf{P}} - \nabla \cdot \overleftrightarrow{\mathbf{Q}} + ... \equiv \epsilon_0 \mathbf{E} + \mathbf{P} \tag{27}$$

and

$$\mathbf{B} = \mu_0 \mathbf{H} + \mu_0 \mathbf{M}. \tag{28}$$

In addition,

$$\mathbf{J} = \mathcal{J}(\mathbf{E}, \mathbf{H}), \tag{29}$$

where $\mathcal{J}$ is a function of the electric and magnetic fields, ϵ_0 and μ_0 are the permittivity and permeability of vacuum, and $\overleftrightarrow{\mathbf{Q}}$ is the macroscopic quadrupole moment density. $\widetilde{\mathbf{P}}$ is the dipole-moment density, whereas $\mathbf{P}$ is the effective macroscopic polarization that also includes the macroscopic quadrupole-moment density [12, 28, 29, 31, 39]. The polarization and magnetization for time-domain linear response are convolutions.

3.4 Local Electromagnetic Fields in Materials

In the literature, the effective local field is commonly modeled by the Lorentz field, which is defined as the field in a cavity that is carved out of a material around a specific site, but excludes the field of the observation dipole. A well-known example of the relationship between the applied, macroscopic, and local fields is given by an analysis of the Lorentz spherical cavity in a static electric field. In this example, the applied field, depolarization field, and macroscopic field are related by

$$\mathbf{E} = \mathbf{E}_a - \frac{1}{3\epsilon_0}\mathbf{P}. \tag{30}$$

For a Lorentz sphere the local field is well known to be a sum of applied, depolarization, Lorentz, and atomic fields [24, 40]

$$\mathbf{E}_l = \mathbf{E}_a + \mathbf{E}_{depol} + \mathbf{E}_{Lorentz} + \mathbf{E}_{atom}. \tag{31}$$

For cubic lattices in a sphere, the applied field is related to the macroscopic field and polarization by

$$\mathbf{E}_l = \mathbf{E} + \frac{1}{3\epsilon_0}\mathbf{P}. \tag{32}$$

In the case of a sphere, the macroscopic field equals the applied field. Onsager [18] generalized the Lorentz theory by distinguishing between the internal field that acts on induced dipoles and the directing field that acts on permanent dipoles. Some of the essential problems encountered in microscopic constitutive theory center around the local field. Note that recent research indicates that the Lorentz local field does not always lead to the correct polarizabilities in some materials [20]. Near interfaces we expect the Lorentz local field to break down.

The field that polarizes a molecule is the local field $\mathbf{p} \approx \alpha\mathbf{E}_l$. In order to use this expression in Maxwell's equations, the local field needs to be expressed in terms of the macroscopic field $\mathbf{E}_l = \beta\mathbf{E}$, where β is some function. Calculation of this relationship is not always simple. Since the local field is related to the macroscopic field, the polarizabilities, permittivity, and permeability absorb parts of the local field; for example, $\mathbf{p} \approx \alpha\beta\mathbf{E}$. The local field is composed of the macroscopic field and a material-related field, as in eq. (32).

Part of the local field is contributed by effects of additional parameters such as thermal expansion and quantum effects. These additional degrees of freedom are contained in the internal energy.

3.5   Effective Electrical Properties and Mixture Equations

Composite media consist of two or more materials combined in various ways. Usually, in order to define an effective permittivity and permeability, the inclusions must be smaller than the wavelength. Examples of mixing are periodic arrays of spherical particles, layered media, or mixtures materials. The calculation of the effective material electrical properties depends on the frequency of the application and the periodic or random state of the mixture. Over the distance of a wavelength, the material may contain many inclusions or particles.

Various mixture equations for composites have been derived over the years for specific symmetries and material properties. Equations for the effective permittivity or permeability of composites are summarized in Appendix D. Lewin's mixing theory [41] is valid for wavelengths on the order of the inclusion size. Metamaterial behavior can occur when the wavelength approaches the inclusion size. At frequencies corresponding to one-half wavelength across the inclusion, resonances occur that can produce negative permittivity and permeability.

3.6   Structures that Exhibit Effective
Negative Permittivity and Permeability

Evanescent or near fields originate from electromagnetic fields below cutoff near antennas or in waveguides. The evanescent field behavior can be modeled exactly by solving the boundary value problem. Structure-related evanescent field behavior can effectively be obtained from a structure filled with a bulk negative permittivity since for negative permittivity, $\omega\sqrt{\epsilon\mu}$ is pure imaginary and therefore the fields are damped. As a trivial example, consider a waveguide below cutoff. This is an approximation since it uses an effective material property to characterize elements in an electromagnetic boundary-value problem. However, this type of analysis works on the scale of the waveguide. NIM electromagnetic material properties

are effective in that they are not separated from effects due the guiding structures.

The electromagnetic foundations of NIM materials are very simple. Consider a plane wave where the Poynting vector is in direction $\mathbf{k}$. If we take time and spatial transforms of Maxwell's equations we get

$$\mathbf{k} \times \mathbf{E} = \omega \mu \mathbf{H} \tag{33}$$

and

$$\mathbf{k} \times \mathbf{H} = -\omega \epsilon \mathbf{E}. \tag{34}$$

Therefore, for a material with positive permittivity and permeability, $\mathbf{E}$ and $\mathbf{H}$ form a right-handed coordinate system and the phase and group velocities are in the same direction, consistent with the propagation direction of the Poynting vector. Now, if the permittivity and permeability are effectively negative, then we have a left-handed coordinate system and the group velocity is in the direction of $\mathbf{k}$ and phase velocity is in the opposite direction (due to the negative square root for the index of refraction). However, the permittivity and permeability cannot be negative for all frequencies since causality, modeled by the Kramers-Kronig relations, would be violated. Anomalous behavior can occur over limited, dispersive, bands as long as energy-momentum is conserved and causality is maintained.

Whereas the imaginary part of the permittivity must always be positive for energy conservation ($e^{j\omega t}$ sign convention), the real part of the effective permittivity can take on negative values through various resoances. We must emphasize that in NIM the permittivity and permeability are effective quantities and not intrinsic properties, which are negative at the frequencies and regions near structure resonances. The most common way is when the complex current density in Maxwell's equations is combined with the permittivity to form an effective permittivity $\epsilon - \sigma'' - j\sigma'$. This approach has been studied in plasma motion in the ionosphere. It also occurs in semiconductors in the millimeter range, and in superconductors. The Drude model in metals is a Lorentzian-based model of this type of effective negative permittivity (see Figure 5) The permittivity for a plasma has a high-frequency behavior that can be negative. Another way of producing an effective negative permittivity is with an array of inclusions embedded in a media. The inclusions resonate at a specific frequency related to their size [26]. Lorentzian-based models of a resonator can produce negative permittivity. In

24
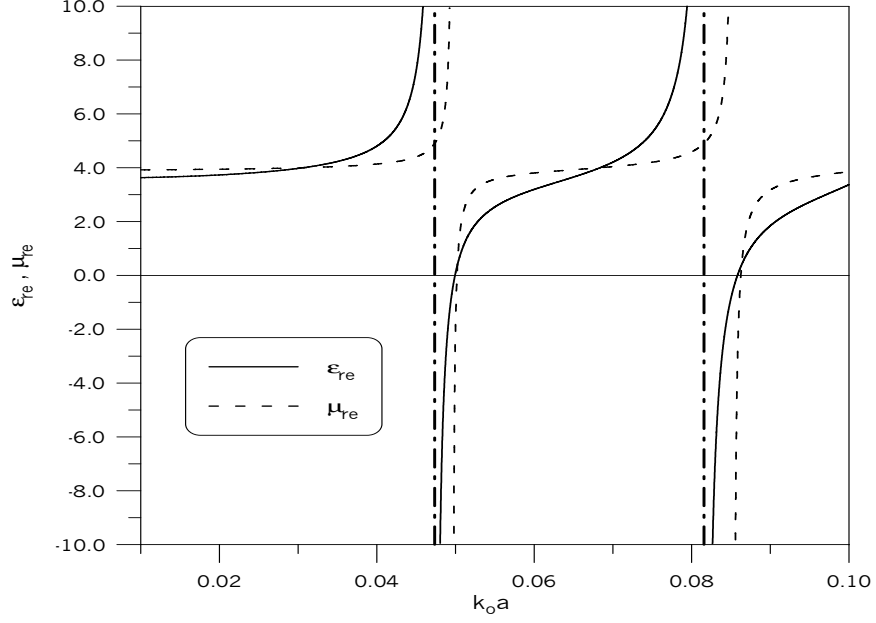
Figure 5. A material where the permittivity and permeability are both simultaneously negative (NIM) [26].

lumped $\mathcal{L} - C$ circuit parameter models, the effective capacitance and inductance can also become negative.

In periodic structures, the eigenvalue spectrum is well known to have propagating and cutoff regions. This is analogous to cavity resonators, where there are propagating and evanescent modes. Propagating cavity modes are analogous to the propagating modes in a periodic structure whereas the cutoff modes are analogous to the evanescent cavity modes and the stop bands in models of semiconductors. When both effective permittivity and permeability are negative simultaneously then propagation is again possible in —. The contribution to the permittivity from microscopic dipoles should not be confused with the effective permittivity that is a bulk effect and not an intrinsic characteristic of the material.

The polarization is usually modeled by a damped harmonic oscillator equation that in the frequency domain yields eq. (11). The simple harmonic oscillator equation for the polarization $\mathbf{P}$ for single-pole relaxation is

$$\underbrace{\frac{d^2\mathbf{P}}{dt^2}}_{\text{inertial}} + \underbrace{\gamma\frac{d\mathbf{P}}{dt}}_{\text{damping}} + \underbrace{\frac{1}{\tau}\mathbf{P}}_{\text{restoring}} = \underbrace{\frac{c_0}{\tau}\mathbf{E}(t)}_{\text{driving}}, \tag{35}$$

25

where γ is a damping coefficient, τ is a relaxation time, and c_0 is a constant. In the Debye model the inertial term is absent. The effective permittivity has the form in eq. (11), which can become negative.

Since no intrinsic magnetic charge exists, an approach to realize negative effective magnetic permeability has to be different from that for the negative effective permittivity. Here again, we can consider intrinsic magnetic material properties or proceed with construction of the electrical circuit configuration that would give an effective permeability containing a negative real part in a certain frequency range. Thin metallic ferromagnetic materials have a large saturation magnetization that yield reasonable values of permeabilities in the gigahertz frequency range.

The constitutive relation for the magnetization of materials is given by the Landau-Lifshitz equation of motion

$$\frac{\partial \mathbf{M}(\mathbf{r}, t)}{\partial t} \approx -\underbrace{\mu_0 |\gamma| \mathbf{M}(\mathbf{r}, t) \times \mathbf{H}(\mathbf{r}, t)}_{\text{precession}} - \underbrace{\frac{\mu_0 \alpha |\gamma|}{|M|} \mathbf{M}(\mathbf{r}, t) \times (\mathbf{M}(\mathbf{r}, t) \times \mathbf{H}(\mathbf{r}, t))}_{\text{damping}}, \qquad (36)$$

where $\mathbf{H}$ is the magnetic field α is a damping constant and γ is the gyromagnetic ratio. This equation models the intrinsic response of spins to applied magnetic fields. In NIM materials, instead of obtaining the magnetization and permeability from eq. (36), effective properties are identified for a resonant system modeled by eq. (12) [26]. The field averaging used in NIM analysis is based on the magnetic field and material properties components along the axes of a unit cell. In his analysis of NIM, Pendry averages the magnetic field in a cube [42]. For each magnetic field component, he gets

$$< \mathbf{H} >_i = \frac{1}{a} \int_{r_i} \mathbf{H} \cdot d\mathbf{r}. \qquad (37)$$

The induction field is averaged as

$$< \mathbf{B} >_i = \frac{1}{a^2} \int_{S_i} \mathbf{B} \cdot d\mathbf{S}, \qquad (38)$$

where i takes on x, y, and z. Following these averaging definitions, the effective relative permeability is then defined as:

$$\mu_{eff(i)} = \frac{< \mathbf{B} >_i}{\mu_0 < \mathbf{H} >_i}. \qquad (39)$$

26

In order to obtain a negative permeability in NIM applications, the circuit has to be resonant, which requires the introduction of capacitance into the inductive system. Pendry [42–44] introduced the capacitance through gaps in coupled-ring resonators. The details of the calculation of effective permeability are discussed in Reference [42]. In principle, any microwave resonant device passive and/or active can be used as a source of effective permeability in the periodic structure designed for NIM applications [45].

We should note that the composite materials developed by Pendry have a scalar permeability. However, in general, the permeability is tensorial.

4. Instrumentation, Specimen Holders, and Specimen Preparation

4.1 Network Analyzers

Automatic network analyzers (ANAs) have become the preferred data acquisition system for many researchers. When making material measurements we need to understand the errors associated with the scattering parameters measured by the network analyzers. Network analyzer systems have various error sources. These include [46]:

- Imperfect matching at connectors

- Imperfect calibration standards

- Nonlinearity of mixers, gain and phase drifts in IF amplifiers, noise introduced by the analog to digital converter

- Imperfect tracking in dual-channel systems

Generally, the manufacturer furnishes specifications for its measuring system. The choice of network analyzer is crucial for accurate phase data over the frequency band of interest.

4.2 ANA Calibration

4.2.1 Coaxial Line Calibration

Various components of the ANA introduce phase and magnitude uncertainties. Calibration of the ANA removes the systematic uncertainties through measurements of a set of standards; for example, shielded open-circuited termination, short-circuited termination, or load. Information on the difference between a specific measurement of these standards and the expected values that are stored in the ANA system generates a set of error-correction coefficients. The calibration coefficients are determined by solving a set of simultaneous equations generated from the linear fractional transformation. After calibration, when the system is operated with the errors correction, the measurements are updated by the calibration information.

The 7 mm line calibration kit contains the following standards:

- Open-circuited termination

- Short-circuited termination

- Low-and high-frequency loads

- Sliding load

4.2.2 The Waveguide Calibration Kit

For calibration of waveguides we can construct a calibration kit for the ANA. The transmission-through-line (TRL) calibration consists of measuring a *through*, a *reflect*, and a section of *line*. The length of line to be used as the *through* is calculated as follows: the phase delay (ϕ) in waveguide is related to line length (ℓ) and guided wavelength (λ_g) by

$$\ell = \frac{\phi \lambda_g}{2\pi}, \tag{40}$$

where the guided wavelength is related to the free-space wavelength by:

$$\lambda_g = \frac{\lambda}{\sqrt{1 - (\frac{\lambda}{\lambda_c})^2}}. \tag{41}$$

A procedure for calculating *line* length is to calculate ℓ for a phase delay of 20° at the lowest frequency of interest, and again for a phase delay of 160° at the highest frequency of interest,

and then choose a line length between these extreme values; typically, $\lambda/4$ at a geometric center frequency ($f_{center} = \sqrt{f_{min}f_{max}}$).

When using waveguide for measurements we can insert sections of waveguide, each approximately two wavelengths in length, between the coax-to-waveguide adapter and the specimen holder. The function of the waveguide sections is to damp out any evanescent modes generated at the coaxial-line to waveguide adapters. The X-band calibration kit contains the following items:

- Coax to waveguide adapters

- Short-circuited termination

- A section of waveguide line to be used as a specimen holder

- A section of calibration line

- Two lengths of X-band waveguide approximately two wavelengths long acting as mode filters

- load

- Calibration coefficients provided on an appropriate computer disk

4.2.3 On-Wafer Calibration, Measurement, and Measurement Verification

Work at NIST led to the development of accurate multiline through-reflect-line calibrations for on-wafer measurement. The method uses multiple transmission-line measurements to improve both the accuracy and bandwidth of the calibration over that of conventional TRL techniques [7].

The multiline method is implemented in the NIST MultiCal software suite. The software also determines the complex frequency-dependent characteristic impedance of the transmission lines used in the calibration and allows the user to set the calibration reference impedance to the characteristic impedance of the line, typically 50 Ω, or to any other real value. The calibration comparison method assesses the accuracy of a working calibration

by comparing it to an accurate reference calibration, usually the multiline TRL calibration. This method has led to an understanding of the systematic uncertainties present in many common on-wafer calibrations. The calibration comparison method has also proved to be a valuable tool for the development of working calibrations with an accuracy comparable to the multiline TRL calibration [7, 47].

4.3   Specimen-Holder Specifications

4.3.1   Specimen Holder

The specimen holder for transmission-reflection (TR) measurements should consist of high-precision waveguide or coaxial line. There should be a length of waveguide between the waveguide-to-coaxial line adapter and specimen holder to damp out evanescent waves generated at these discontinuities. The length of the specimen holder should be measured with a high degree of precision. Nicks and other abrasions in the specimen holder will, of course, degrade performance by increasing the surface resistance. When a 7 mm coaxial beadless air line is used, APC-7 connectors are usually preferred. The specimen holder should be treated with extreme care and stored in a protected area.

Figure 6. Cross section of a coaxial line and specimen.
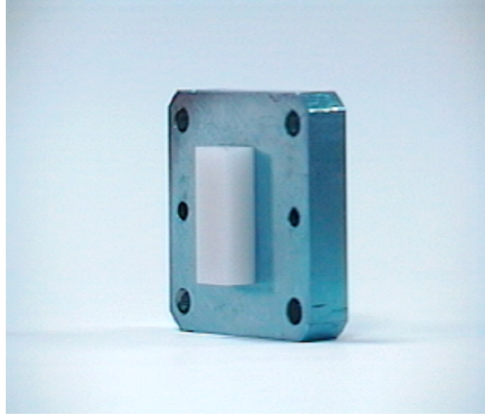
Figure 7. Cross section of a waveguide with specimen.

The real part of the surface impedance determines the loss in the line and is given by

$$Z_s = \frac{1+j}{2\pi} \left[\frac{1}{b(\sigma_{dc}\delta)_{oc}} + \frac{1}{a(\sigma_{dc}\delta)_{ic}} \right],$$

(42)

where b is the inner radius of the outer conductor, a is the outer radius of the inner conductor, σ_{dc} is the conductivity, $\delta = 1/\sqrt{\pi f \mu}, and \sigma_{dc}$ is the skin depth [48].

Wong has shown that the impedance of a precision 7 mm coaxial air line, with uniformity of approximately $\pm 2~\mu m$, varies slightly with frequency from 50.25 Ω at 0.1 GHz to 49.95 Ω at 20 GHz [48].

4.3.2   Specimen Preparation

Specimens intended for measurements must be carefully, prepared. Scratches, nicks and cracks may alter the measured dielectric properties. Minimize any unnecessary wear and tear on the specimen by placing it in a secure area between measurement sessions. The specimen length measurement is critical and should be performed carefully with a precision micrometer at laboratory temperatures. Dimensions for 7 mm line and X-band waveguide specimens are given in Figures 8 and 9.

The following list summarizes the preparation procedure:
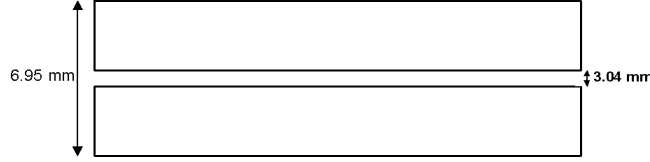
Figure 8. Machining details for a 7 mm coaxial-line specimen. Uncertainties in dimensions approximately ±0.02 mm.

- Carefully select a piece of material free of unusual inhomogeneities or cracks.

- Have the specimen machined to fit as tightly as possible into the specimen holder. The machining process should not leave metallic residue on the specimen. Note that gaps near the center conductor of a coaxial line are more serious than gaps near the outer conductor (by a factor of 2.3). Specimens that fit very tightly on the outer conductor can be inserted more easily by prior cooling.

- Measure the specimen length with a high degree of precision at a temperature very close to that realized in the laboratory. The resulting strain, $\Delta L/L$, from increased temperature can be calculated from the linear thermal expansion coefficient α_T by using the relation $\Delta L/L = \alpha_T \Delta T$.

- Keep the specimen very clean and store in a secure area with required humidity. If the specimen requires cleaning, an ultrasonic cleaner will suffice and be careful to avoid the effects of absorbed water. Alcohol usually works better than distilled water.

- Keep the gap between specimen and guide walls to a minimum. We have found that clearances of 2-7 μm (0.0001 to 0.0003 in.) are acceptable for low-permittivity materials. However, even with these tolerances the measurement of high-permittivity
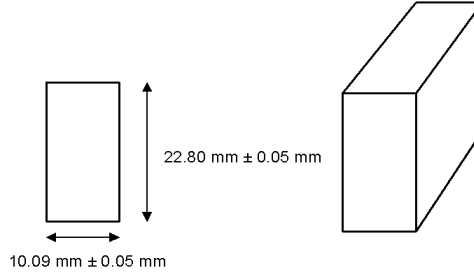
Figure 9. Dimensions of a waveguide specimen. Uncertainties in dimensions approximately ± 0.02 mm.

> materials is limited. For better results the specimen faces should have copper or another conductor deposited on them, or the specimen should be soldered into the line.

5.   Overview of Measurement Methods for Solids

Each dielectric measurement method has its frequency range of applicability. Each method also utilizes a specific electric-field orientation. Since there is such variability in measurement fixtures, frequencies of interest, field orientation, and temperature dependence, we will give a broad-brush overview here of many of the important features of the most important measurement techniques. These features are summarized in Tables 3, 4, and 6.

The full characterization of anisotropic materials generally requires two measurement techniques, one for the component of permittivity normal to the specimen face, and one for the in-plane permittivity. The loss tangent measurement is not usually as strongly affected as ϵ'_r by anisotropy, and a single measurement of loss tangent usually suffices. For example, resonant transmission-line methods can be used for ϵ'_r and the loss could be obtained by more accurate in-plane techniques such as a TE_{01} resonator (for modes see Figure 5). However, there are materials where the loss is significantly anisotropic, and therefore two independent methods for loss must be applied.

Measurement of magnetic materials requires a strong applied magnetic field. Magnetic

33

Table 3. Dielectric measurement categories for medium-high-loss materials compared with typical uncertainties for each method [49].

Technique	Field	Advantages	$\Delta\epsilon_r'/\epsilon_r'$,	$\Delta\tan\delta_d$
Coaxial line, waveguide	TEM,TE$_{10}$	Broadband	± 1 to 10	± 0.005
Slot in waveguide	TE$_{10}$	Broadband	± 1 to 10	± 0.005
Capacitor	Normal E-field	Low frequency	± 1	$\pm 10^{-4}$
Cavity	TE$_{01}$	Very accurate	$\pm 0.2\%$	$\pm 5\times 10^{-5}$
Cavity	TM$_{0m}$	ϵ_{rz}'	± 0.5	$\pm 5\times 10^{-4}$
Dielectric resonator	TE$_{01}$	Very accurate	$\pm 0.2\%$	$\pm 1\times 10^{-5}$
Coaxial Probe	TEM, TM$_{01}$	Nondestructive	± 2 to 10	± 0.02
Fabry-Perot	TEM	High frequency	± 2	± 0.0005

Table 4. Magnetic measurement methods compared with typical uncertainties.

Technique	Field	Advantages	$\Delta\mu_r'/\mu_r'$, %	$\Delta\tan\delta_d$
Coaxial line, waveguide or waveguide	TEM,TE$_{10}$	Broadband	± 2	± 0.01
Cavity	TE$_{011}$	Very accurate	± 0.5	$\pm 5\times 10^{-4}$
Cavity	TM$_{110}$	μ_{rz}'	± 0.5	$\pm 5\times 10^{-4}$
Dielectric resonator	TE$_{011}$	Very accurate	± 0.5	$\pm 1\times 10^{-5}$
Whispering-gallery	Hybrid	Very accurate	± 1	$\pm 5\times 10^{-6}$
Courtney	TE$_{01}$	Very accurate	± 1	$\pm 5\times 10^{-5}$

materials can be measured in coaxial lines and waveguides, split-post magnetic resonators, TM$_{110}$ [50] or TE$_{011}$ cavities, whispering-gallery modes, or other dielectric resonators (see Table 4).

Over the years certain methods have been identified as particularly good for various classes of measurements, and these have been incorporated as standards of the ASTM (American Society for Testing and Materials) [51] and the European Committee for Electrotechnical Standardization (CENELEC). However, the list is rather dated and doe not include some of the more highly-accurate, recently developed methods. The ASTM standard techniques applicable to thin materials are summarized in Table 6.

Measurement fixtures where the electromagnetic fields are tangential to the air-material interfaces, such as in TE$_{01}$ cavities and dielectric resonators, generally yield more accurate results than fixtures where the fields are normal to the interface. This is because the tan-

Table 5. Cavity Fields

Cylindrical TE$_{01}$ Cavity	E$_\phi$	H$_\rho$, H$_z$
Coaxial TEM Line and Cavity	E$_\rho$	H$_\phi$
Cylindrical TM$_{01}$ Cavity	E$_\rho$, E$_z$	H$_\phi$
Rectangular Waveguide TE$_{10}$	E$_y$	H$_x$, H$_z$

Table 6. ASTM standard techniques for dielectric measurements.

ASTM No.	Applicability	Method	Frequency
D150	discs	capacitor	1 Hz to 10 MHz
D1531	thin sheeting	bridge network	1 kHz to 1 MHz
D1673-94	polymers	capacitor	10 kHz to 100 MHz
D2149	discs	capacitor	50 Hz to 10 MHz
D2520	small rods	rectangular resonator	1 GHz to 50 GHz
D3380	clad substrates	stripline	8 GHz to 12 GHz
D5568	cylindrical specimens	coaxial line	1 MHz to 20 GHz

gential electric field vanishes on a conductor, so any air gap will be in a low-field region. In contrast, if the field is normal to the electrode, the air gap is in a region of strong electric field. In fact the electric field is more intense in the air gap region (E_a, ϵ_a) than in the specimen region (E_s, ϵ_s), since the continuity of the normal component of the displacement field yields: $E_a = \epsilon_s E_s / \epsilon_a$. If the electric field is tangential to a gap between a material and a metallic wall of a measurement fixture, then the measurement of ϵ'_r is minimally influenced by the gap and no gap correction is usually required. Unfortunately, for many applications, in-plane field measurements are not the preferred one. For example, circuit boards and PWBs using microstrip or stripline, operate with the electric field primarily normal to the plane of the sheet and, therefore, this component of the permittivity is of primary interest. However, measurements with the electric field perpendicular to the specimen face suffer from air-gap depolarization. In such cases, the effects of the air gap must be either accepted or mitigated by metalization of specimen surfaces or application of conductive pastes, or corrected for by numerical techniques [3, 4]. The gap correction is due to the capacitance of air in the gap and effectively depends on frequency only through the dependence of ϵ_r in the gap-correction
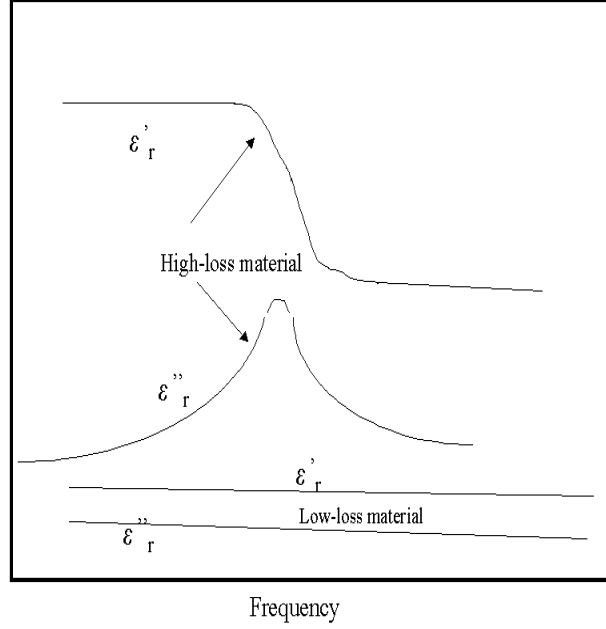
Figure 10. Typical frequency dependence in low loss and Debye materials.

formula. TM_{0n} resonators are particularly good for measuring the permittivity along the axis of a rod specimen (see ASTM D2520).

The real and imaginary parts of the permittivity, excluding the contribution of the dc conductivity, are related by the Kramers-Kronig dispersion relations [52]. This relationship is a requirement of causality that the fields are turned on at some time and are not static fields. Kramer-Kronig relations are an integral relationship between the real and imaginary parts of the permittivity. A consequence of these relations is that frequency-dependent changes in the real and imaginary parts of the permittivity are correlated (see, for example, the correlation in Figure 10). One example of a Kramers-Kronig relation is

$$\epsilon_r''(\omega_0) = \frac{\sigma_{dc}}{\epsilon_0 \omega_0} + \frac{2}{\pi} P \int_0^\infty [\epsilon_r'(\omega) - 1] \frac{\omega_0}{\omega_0^2 - \omega^2} d\omega. \tag{43}$$

Although eq. (43) is exact, it requires very broad frequency information and is relatively complicated to use. A few simple consequences of Kramers-Kronig are the following. The static value of the permittivity, for a material with no dc loss, is $\epsilon_s = 1 + (2/\pi) P \int_0^\infty (\epsilon''(\omega)/\omega) d\omega$.

36
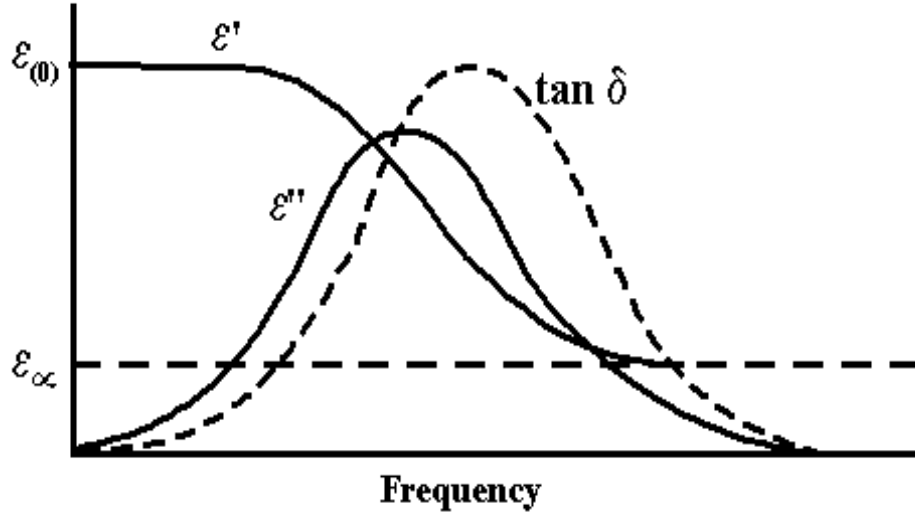
Figure 11. Typical permittivity variation for polar materials.

If there is no dc conductivity, $\epsilon''(0) = 0$. Lynch [53] developed a simplified version of this relationship that relates changes in permittivity between frequency points to the expected loss tangent. His analysis allows a consistency check on measurements in the radio-frequency to low microwave bands for measurements where the loss tangent changes slowly with frequency and the loss contains no appreciable contribution from the dc conductivity. If we have two measurements of the permittivity at different frequencies, then

$$\frac{|\epsilon_1 - \epsilon_2|}{\epsilon_1} \approx m \tan \delta \log_{10} \left(\frac{f_2}{f_1} \right). \tag{44}$$

In this equation, $1.0 \leq m \leq 2.3$, and Lynch determined $m = 1.5$ is usually optimal.

In the radio-frequency and microwave bands, ϵ'_r is almost always a monotonically decreasing function of increasing frequency (see Figures 11 and 10). The permittivity of low-loss materials decreases slower (dispersion) with frequency than high-loss materials. In the radio-frequency and low microwave bands, any increase in measured ϵ'_r as the frequency increases is almost always due to a fixture geometrical resonance or other fixture-dependent artifacts. On the other hand, ϵ''_r does not necessarily decrease as frequency increases. It may increase as frequency increases or form a Debye loss peak. The loss tangent in the radio-frequency and microwaves bands of most ceramics, fused silica, some plastics and glasses, increases nearly

37
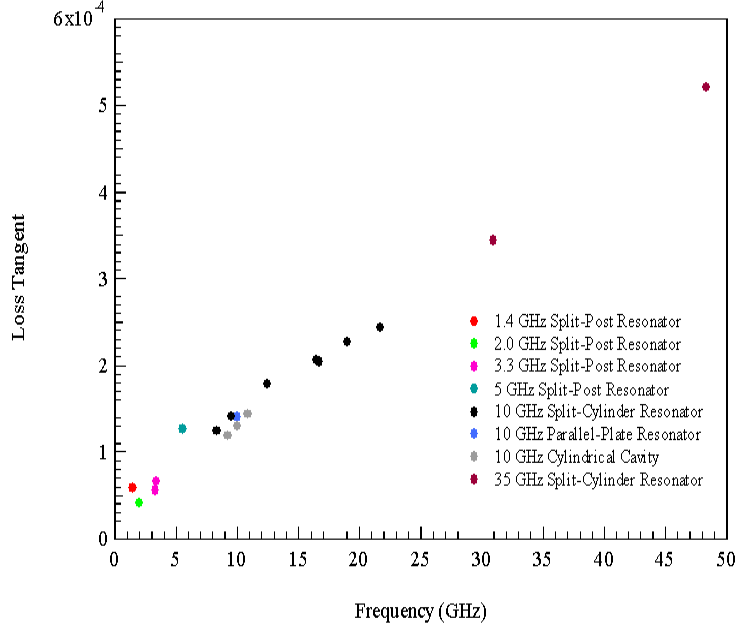
Figure 12. The loss tangent of fused silica for various fixtures operating at different frequencies. Notice a nearly linear dependence on frequency

linearly as frequency increases. In such cases, we can extrapolate loss-tangent measurement data from one frequency range to another (see Figure 12). Materials of very low-loss have loss tangents and permittivity in the microwave spectrum that are nearly frequency independent (see, for example, Figure 13)). This is a direct consequence of Kramers-Kronig relations since the changes in the loss and the real part of the permittivity are strongly correlated over a band of frequency. In materials with a finite dc conductivity, ϵ_r'' increases at low frequencies as $1/\omega$ as frequency decreases, where $f = 2\pi\omega$ is frequency. Conducting materials are difficult to measure at low frequencies ($f < 1$ MHz). This is because the boundary layer between the specimen and electrode produces an electrode-polarization double-layer capacitance that biases the measurement result.

There are many mathematical models used for extracting permittivity and permeability.

38
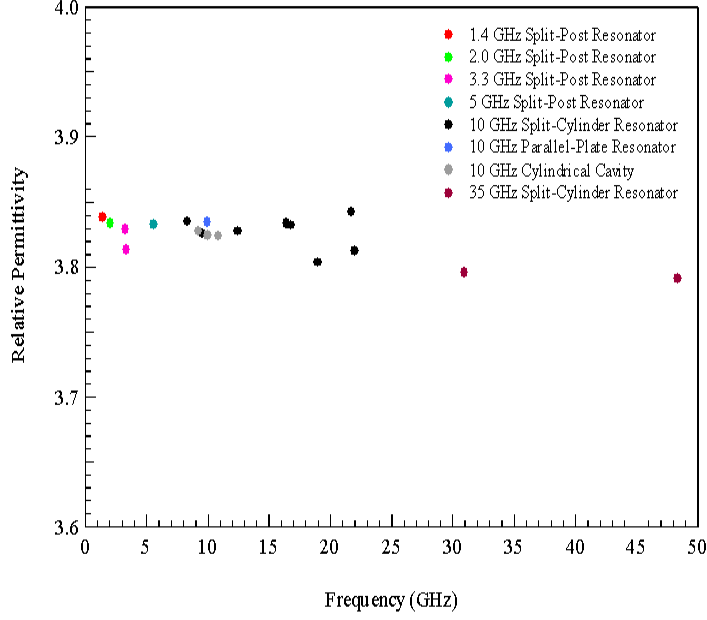
Figure 13. The permittivity of fused silica for various fixtures operating at different frequencies.

Methods based on Maxwell's equations use single- or full-mode models that relate the resonant frequency or transmission and reflection coefficients to functions of the permittivity (see Table 7). These types of models are accurate, but require complicated solutions to Maxwell's equations and can be computationally intensive.

At lower frequencies, dielectric and magnetic material properties can be extracted from a transmission-line model using the impedance Z_c and propagation coefficient γ (see Figure 14). For cases where both dielectric and magnetic properties are required we must use both the impedance and propagation coefficient simultaneously [4, 54].

For dielectrics, either the impedance or propagation coefficient may be used in isolation for determining the permittivity. In both cases, a model of the transmission-line structure is required that relates the material properties to the reflection and transmission coefficients.

39

Table 7. Models used for the permittivity extraction.

Model	Advantage	Disadvantage
Lumped element	simple	limited to low frequency
Distributed element	simple	medium-low frequency
Single-mode	based on Maxwell's eqs	cannot handle discontinuities
Full-mode	based on Maxwell's eqs	can handle discontinuities
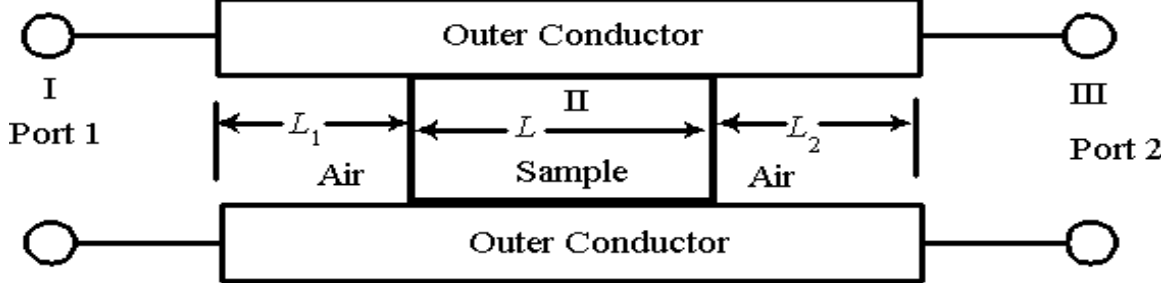
Figure 14. Waveguide transmission line with specimen

The models may be based on lumped circuits or distributed elements. For distributed-element models, we usually use an approximation to Maxwell's equations in terms of current and voltage waves on the transmission line.

Surface roughness of the conductor increases the capacitance, resistance, and inductance. The capacitance is increased because the effective thickness of the rough material between two conductors is less than the measured thickness [55]. The roughness of the surface of the conductors can also affect the resistance due to the increased surface area.

6. Transmission-Line Techniques

Transmission-line methods can be broadly grouped into categories where (a) the cross section of specimen and holder is constant and (b) fixtures where the cross section of the specimen holder or specimen contains discontinuities. The first category is easier to treat since the electromagnetic modes decouple. Usually a dominant mode analysis is sufficient for these types of problems. The second category requires a full-modal solution due to mode generation at interfaces. Fixtures without discontinuities include coaxial and waveguide two-port

systems. Examples of fixtures with discontinuities include shielded coaxial line, open-ended waveguide, and open-ended coaxial probes.

In many cases, transmission-line techniques require specimen preparation such as machining or removal of copper cladding. In the case of printed-wiring boards the copper cladding can be etched to form the specimen into a microstrip for measurements. Bulk specimens must be machined to fit tightly into a waveguide or coaxial line.

Transmission-line measurements use various terminations that produce different resonant behavior in the transmission line. Maximal electric field is required for good permittivity measurements. This can be achieved by an open-circuited or other capacitive termination. Magnetic permeability measurements should be carried out in regions of high magnetic field. This can be achieved by a short-circuited or other inductive termination.

6.1 Coaxial Line, Rectangular, and Cylindrical Waveguides

6.1.1 Overview of Waveguides Used in Transmission/Reflection Dielectric Measurements

Due to their relative simplicity, the off-resonance waveguide and coaxial line transmission or reflection and short-circuit line methods are widely used broadband measurement techniques [3, 54, 56]. In these methods, a precisely machined specimen is placed in a section of waveguide or coaxial line, and the scattering parameters are measured, preferably by an automatic network analyzer. The relevant scattering equations relate the measured scattering parameters to the permittivity and permeability of the material. Network analyzers have improved over the years to a point where broad frequency coverage and accurate measurement of scattering parameters are possible.

Transmission-line measurements usually are made in rectangular or circular waveguide or coaxial lines. The three major problems encountered in transmission line measurements are air gaps between the sample and fixture electrodes, half-wavelength resonances, and overmoding.

Coaxial lines are broadband in the TEM mode and therefore are attractive for permittivity and permeability measurements of lossy materials. Coaxial-line measurements can be

made using short-circuited, open-circuited, or matched-load terminations. The short-circuit line (SCL) method was used by Roberts and von Hippel [57] over 50 years ago as an accurate broadband measurement procedure. Shielded open-circuited line (SOCL) methods are used for measurements of powders and liquids. Full-scattering matched-load methods, where the transmission line is open on both ends, are usually used to measure solids.

Coaxial lines can also be used as permeameters for measurements of the magnetic properties of ferrites. In this approach, measurements are obtained by placing a specimen in a coaxial line terminated in a short-circuit and measuring the change in inductance and resistance using an impedance analyzer. This procedure is summarized in Reference [58]. The permeability of metals can be determined by winding around a metal toroid of the material under test with a fine wire and measuring the change in inductance compared to a measurement in free space. Open-circuited terminations are useful for dielectric one-port measurements of liquids and powders.

Corrections for the effects of air gaps between the specimen holder and the sample can be made by analytical formulas or mitigated by use of conducting pastes or solder that is applied to the external surfaces of the specimen before insertion into the specimen holder [54, 59].

The field model for closed waveguide structures usually assumes a single mode of propagation in the specimen. Propagation of higher-order modes becomes possible in inhomogeneous specimens of higher permittivity. Air gaps play an important role in mode conversion. Higher-order modes require a coupling mechanism in order to begin propagating. In waveguide and coaxial line the asymmetry of the specimen and machining precision promotes higher-order mode propagation. Generally, the appearance of higher-order modes manifest themselves as sudden dips in the reflection coefficient, which is a result of resonance of the excited higher-order TM, or TE modes. The TEM mode will also resonate at integral multiples of one half wavelength in the sample. The single-mode model, developed in the next section, can handle the higher-order TEM resonances in dielectrics, but not the TE or TM resonances. We can expect point-by-point numerical reduction techniques to break down for single mode models near higher-order mode resonances. These modes propagate in materials of high-permittivity or inhomogeneous specimens [56]. Optimized, multifrequency

Table 8. Rectangular waveguide dimensions and operating frequencies in air.

EIA WR	Band	a (cm)	b (cm)	TE_{10} Operating Frequency(GHz)
650	L	16.510	8.255	1.12 - 1.70
430	W	10.922	5.461	1.70 - 2.60
284	S	7.710	3.403	2.60 - 3.95
187	C	4.754	2.214	3.95 - 5.85
90	X	2.286	1.016	8.20 - 12.4
42	K	1.067	0.432	18.0 - 26.5
22	Q	0.569	0.284	33.0 - 50.0

solutions fare better in this respect [60] since these frequencies can be given less weight. In order to minimize the effects of higher-order modes, shorter specimens can be used to maintain the electrical length less than one-half the guided wavelength in the material. Also, well-machined specimens produce fewer spurious modes.

Effects due to unwanted higher-order modes can be minimized by mode filters. This can be particularly helpful in cylindrical waveguides. One way to construct a mode filter is to helically wind a fine wire about the inner surface of the waveguide specimen holder, thus eliminating longitudinal currents. Another approach is to insert cuts in the waveguide walls to minimize axial currents along the waveguide. These types of mode filters do not work for TEM-mode structures.

6.1.2   sections of Waveguides Used as Specimen Holders

TE and TM waveguides can be only used over a band of frequencies. Therefore the selection of a waveguide depends on the frequencies to be measured. The cutoff frequency is a lower bound on frequencies that can be transmitted in the guide without the fundamental mode becoming evanescent. At cutoff, the long transverse dimension of the rectangular waveguide encompasses one half wavelength, which is a resonant condition. Whereas coaxial lines have no cutoff, at low frequencies the effects of skin depth can affect the measurement of the TEM mode.

A list of operational frequencies for various waveguide sizes are given in Table 8 and for various coaxial line sizes in Table 9.   The cutoff frequency for either TE or TM waves in

Table 9. Air-filled coaxial cable operating frequencies.

Coaxial cable outer diameter(mm)	Upper operating frequency (GHz)
3.5	34.5
7.0	18.2
14.0	8.6

rectangular waveguide is given by

$$(f_c)_{mn} = \frac{1}{2\sqrt{\mu'\epsilon'}}\sqrt{(\frac{m}{a})^2 + (\frac{n}{b})^2}, \tag{45}$$

where a is the long dimension of the guide, b is the short dimension of the guide, and $m, n = 0, 1, 2....$ For the TE_{10} mode the cutoff frequency is:

$$(f_c)_{mn} = \frac{1}{2\sqrt{\mu'\epsilon'}a} = \frac{c}{2a}. \tag{46}$$

Rectangular waveguide operated in the TE_{10} mode becomes overmoded at twice the cutoff frequency. Operating frequencies and waveguide dimensions are given in Tables 8 and 9.

For a circular waveguide of radius a the attenuation is given by [5]

$$\alpha_{TM_{mn}} = \frac{R_s}{a\eta}\frac{1}{\sqrt{1 - (\frac{f_c}{f})^2}}, \tag{47}$$

$$\alpha_{TE_{mn}} = \frac{R_s}{a\eta}\frac{1}{\sqrt{1 - (\frac{f_c}{f})^2}}\left[(\frac{f_c}{f})^2 + \frac{m^2}{(p'_{mn})^2 - m^2}\right], \tag{48}$$

where p'_{mn} are the roots of $J'_m(p'_{mn}) = 0$ and $\eta = \sqrt{\mu_0/\epsilon_0}$.

The cutoff frequencies for TM_{mn} in circular waveguide are given by

$$(f_c)_{mn} = \frac{p_{mn}}{\sqrt{\epsilon\mu}2\pi a}, \tag{49}$$

where p_{mn} are the nth roots of $J_m(p_{mn}) = 0$. For TE_{mn} waves we have

$$(f_c)_{mn} = \frac{p'_{mn}}{\sqrt{\epsilon\mu}2\pi a}, \tag{50}$$

where p'_{mn} are the nth roots of $J'_m(p'_{mn}) = 0$. Coaxial line has the distinct advantage of having no cutoff frequency. However, coaxial line becomes multimoded above the cutoff

frequencies of the TE and TM modes (for a review of cutoff frequencies in TEM structures see Weil [61]). Higher-modes can be formed by bead inhomogeneities, discontinuities, and mismatches that couple to the TE_{11} and higher modes. The approximate upper frequency limit is given in Table 9. The propagation of the TE and TM modes in addition to the TEM mode is possible at higher frequencies. The cutoff wave numbers for higher TM waves in coaxial line are given by the roots of the equation [5, 61],

$$\frac{N_n(k_c a)}{J_n(k_c a)} - \frac{N_n(k_c b)}{J_n(k_c b)} = 0, \tag{51}$$

and for TE waves in coaxial line by

$$\frac{N_n'(k_c a)}{J_n'(k_c a)} - \frac{N_n'(k_c b)}{J_n'(k_c b)} = 0, \tag{52}$$

where J_n and N_n denote the Bessel functions of the first and second kind, and a and b are the inner and outer radii, respectively [5]. The cutoff wavelengths are given approximately by

$$\lambda_c \approx \frac{2}{q}(b - a) \ , \ q = 1, 2, 3, \cdots. \tag{53}$$

For example, the TM mode cutoff frequency in 7 mm coaxial line for eq. (53) is approximately 34 GHz. For beadless air line it is possible to exceed the frequencies given in Table 9.

6.2   Slots in Waveguide

A useful method for both low- and high-loss substrates is the slot-in-a-waveguide technique where the material is inserted as shown in Figure 15. The material is parallel to the TE_{10} electric field; therefore the effects of air gaps are minimal. The slots are in the center of the wide wall of the waveguide. The sample is inserted into the slots and protrudes out both sides. To minimize radiation from the slot, the slot should be kept as narrow as possible [62].

6.3   Microstrip, Striplines, and Coplanar Waveguide

In the previous section we considered closed transmission lines. However, in many applications the transmission lines are planar with open surfaces. For example, conductors may be
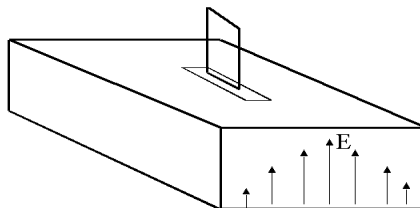
Figure 15. Measurement of substrates using a slot in a waveguide.

deposited directly on thin films or substrates to form transmission lines. Open structures can radiate and have a complicated field structure. Measuring the permittivity of lossy materials, circuit boards, thin films, and substrates nondestructively is frequently of interest [63]. These materials may be thin and may be clad in copper, making measurements with closed transmission lines difficult. Generally, an effective permittivity is defined by relating the measured capacitance with and without air filling. Therefore ϵ_{eff} depends on the fields in the specimen and the fringing fields. Since the structures are open, approximate permittivity models are usually used. The effective permittivity ϵ_{eff} maps complicated field structure into a single parameter. If the effective permittivity is used in isolation then it has little fundamental significance. However, if effective permittivity is coupled to more extensive fixture models, as Getsinger and Wheeler have done [64,65], then it can be used to obtain the permittivity [66–68]. Loss is usually difficult to measure in transmission lines and the cases of microstrip, coplanar waveguide, and stripline are no exceptions. Resonant microstrips or striplines allow a more accurate calculation of the loss tangent than do nonresonant methods.

The permittivity is obtained from the shift in resonant frequency. In microstrip as depicted in Figure 16, the total conductor loss has contributions from both the strip conductor and the ground plane. For narrow microstrip, the ground plane loss is a small part of the total loss, whereas for wide microstrip, the ground-plane loss becomes more important, see References [69] and [70]. In fact, for $w/h >> 1$, the ground-plane loss nearly equals the strip

46
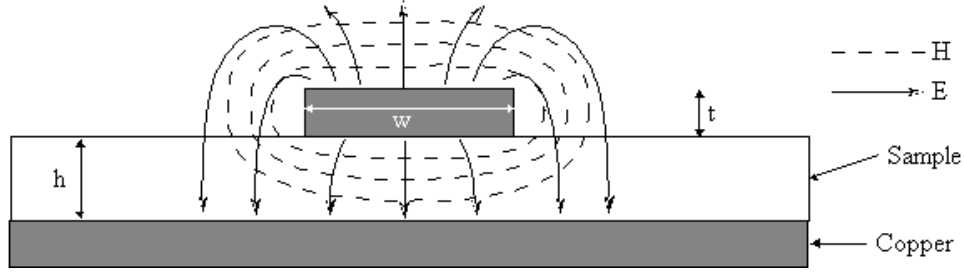
Figure 16. Cross section of a microstrip.

loss. The conductor loss can be obtained from [71]

$$\alpha_r = \frac{R_s}{2Z_o I^2} \int_{-\infty}^{\infty} |J_r(x)|^2 \ dx \ ,$$ (54)

where J_{sr} is the current density on the strip given in reference [69], and R_s is the Leontovich surface resistance [72] and is given by eq. (7). This integral can be evaluated to yield

$$\alpha_{gr} = \frac{R_s}{w\pi Z_0} \left\{ \arctan \frac{w}{2h} - \frac{h}{w} \ln \left(1 + \left(\frac{w}{2h} \right)^2 \right) \right\}.$$ (55)

Thus, the total conductor loss is given by

$$\alpha_{T(micro)} = \alpha_{strip} + \alpha_{gr}.$$ (56)

For a microstrip line, the attenuation constant associated with the strip conductor is expressed as

$$\alpha_{strip} = \frac{R_{sm}}{Z_0} \frac{\ln \left(\frac{w}{t} \frac{t}{\Delta} - 1 \right)}{2\pi^2 w},$$ (57)

where w is the strip width, t is the strip thickness, and Δ is the limit for the integrations, as defined in Reference [69].

Reference [73] gives values of Δ for superconductors. R_{sm} is the modified Horton impedance boundary condition as discussed in [69] and given by

$$R_{sm} = \omega\mu_c t \ Im \left(\frac{\cot (k_c t) + \csc (k_c t)}{k_c t} \right),$$ (58)

where k_c is the wavenumber in the conductor. Z_o is the characteristic impedance given by [74]

$$Z_o = \frac{\eta_o}{4\pi} \sqrt{\frac{2}{\epsilon_r + 1}} \ln \left\{ 1 + \frac{32h}{w} \left[\frac{h}{w} r_\epsilon + \sqrt{\left(\frac{hr_\epsilon}{w} \right)^2 + \left(\frac{\pi(\epsilon_r + 1)}{16\epsilon_r} \right)^2} \right] \right\},$$ (59)

47

where h is the height of the substrate, η_0 is the impedance of free space and

$$r_\epsilon = \sqrt{0.4052 + \frac{0.5160}{\epsilon_r} + \frac{0.0788}{\epsilon_r}}. \tag{60}$$
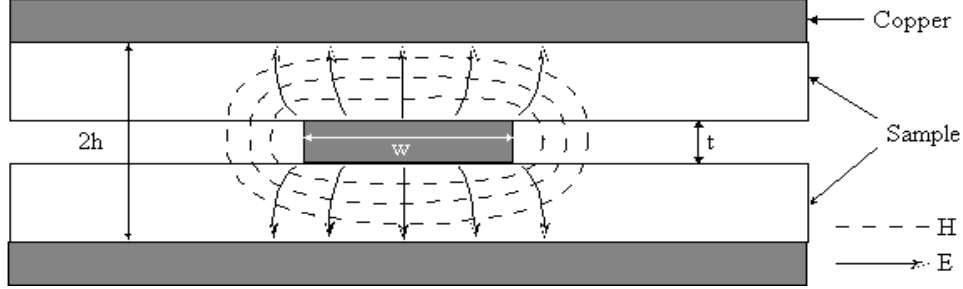
Figure 17. Cross section of a covered stripline [75].

As with the microstrip, the line loss for a stripline consists of components from both the strip and its ground planes. Holloway has calculated the attenuation constant for stripline [69, 70], which is

$$\alpha_{T(stripline)} = \alpha_{strip} + \alpha_{ground}, \tag{61}$$

where

$$\alpha_{strip} = \frac{R_{sm}}{2\pi^2 Z_0 w} \ln\left(\frac{w}{\Delta} - 1\right). \tag{62}$$

Once again, Δ is the stopping distance and is given in Reference [69, 70]. R_{sm} is given by eq. (58) and Z_0 is the impedance

$$Z_0 = \sqrt{\frac{\mu_0}{16\epsilon}} \frac{K(k)}{K(k')}, \tag{63}$$

where K is the elliptical integral of the first kind, $k = \mathrm{sech}(\pi w/4h)$, $k' = \sqrt{1 - k^2}$, w is the width of strip, and h is the distance between the inner and outer conductors. The ground-plane losses are

$$\alpha_{ground} = \frac{R_s}{Z_0 w} F\left(\frac{w}{h}\right), \tag{64}$$

where $R_s = 1/\sigma_{dc}\delta$ is the surface impedance, σ_{dc} is the metal conductivity, δ is the conductor skin depth, and

$$F\left(\frac{w}{h}\right) = \frac{2h}{\pi^2 w} \int_{-\infty}^{\infty} \left[\tan^{-1}(e^{(y-w\pi/4h)}) - \tan^{-1}(e^{(y+w\pi/4h)})\right]^2 dy. \tag{65}$$

48
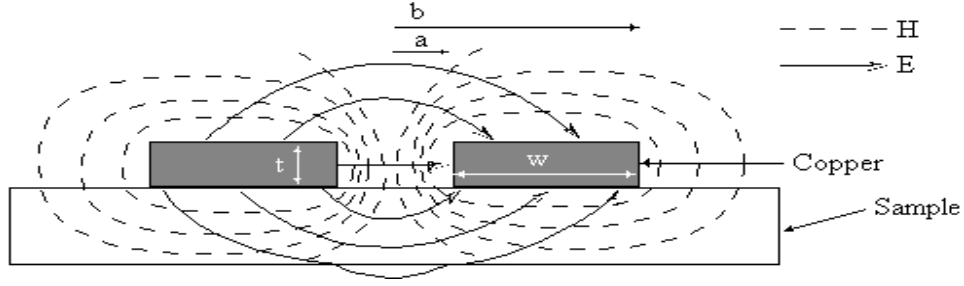
Figure 18. Coplanar slot cross section.

In coplanar slot waveguide (CPS), as shown in Figure 18, the characteristic impedance for a thin stripline is given by [70]

$$Z_0 = \sqrt{\frac{2\mu_0}{\epsilon_0(\epsilon_r + 1)}} \frac{K(k)}{K(\sqrt{1 - k^2})}. \tag{66}$$

The attenuation is [70]:

$$\alpha_{CPS} \approx \frac{R_{sm}b^2}{4Z_0 K^2(k')(b^2 - a^2)} \left[\frac{1}{a} \ln\left(\frac{2a + \Delta}{\Delta} \frac{b - a - \Delta}{b + a - \Delta}\right) + \frac{1}{b} \ln\left(\frac{2b - \Delta}{\Delta} \frac{b - a - \Delta}{b + a + \Delta}\right) \right]. \tag{67}$$

The variation of the attenuation with frequency for stripline, microstrip, CPS, and CPW lines is given in reference [9]. The attenuation in coplanar waveguide (CPW) (see Figure
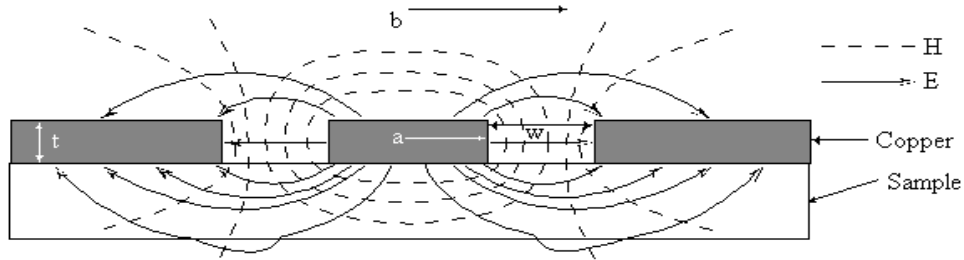
Figure 19. Coplanar waveguide fixture cross section.

(19)) was calculated by Holloway [73, 76]

$$\alpha_{CPW} \approx Re\left[\frac{F}{Z_0} \frac{2}{1 + \sqrt{1 + \frac{4F}{Z_0 \gamma_{mo}}}} \right], \tag{68}$$

49

where

$$F = \frac{(Z_s + Z_m)b^2}{16K^2(k)(b^2 - a^2)} \left[\frac{1}{a} \ln\left(\frac{2a}{\Delta}\frac{b-a}{b+a}\right) + \frac{1}{b} \ln\left(\frac{2b}{\Delta}\frac{b-a}{b+a}\right) \right], \tag{69}$$

with

$$\gamma_{mo} = j\omega\sqrt{\epsilon\mu_0}\sqrt{\frac{\epsilon_r + 1}{2}}, \tag{70}$$

$$Z_0 = \sqrt{\frac{\mu_0}{16\epsilon_0\epsilon_{eff}}}\frac{K(k')}{K(k)}, \tag{71}$$

$$\epsilon_{eff} = \frac{\epsilon_r + 1}{2}, \tag{72}$$

$$Z_s = -j\sqrt{\frac{\mu_0}{\epsilon_c - j\sigma_{dc}/\omega}}cot(k_c t), \tag{73}$$

$$Z_m = -j\sqrt{\frac{\mu_0}{\epsilon_c - j\sigma_{dc}/\omega}}csc(k_c t). \tag{74}$$

σ_{dc} is the conductor's conductivity, and ϵ_c is the conductor's permittivity that is small in comparison to σ and can be neglected. Also,

$$k' = \sqrt{1 - k^2}. \tag{75}$$

6.4   Ground-Penetrating Radar

Specialized antenna systems have been used to detect buried objects. The use of the reflection coefficient allows the dielectric measurement of buried material and possibly the reconstruction of the geometry of buried objects such as archaeological artifacts, pipes, conduit, or land mines [77–83].

6.5   Free-Space Measurements

Free-space measurements are commonly performed using antennas, as shown in Figures 20 and 21. The Styrofoam pylons have a permittivity close to that of freespace, roughly 1.05. Multiple reflections from the room walls are commonly suppressed by use of absorbing tiles. Free-space measurements, depending on the type of antenna, generally operate in the band from 50 MHz to 30 GHz. In these methods the TEM mode transmission and reflection coefficients are measured using algorithms similar to those used in closed transmission lines to obtain the material properties [84–87]. The calibration method used is generally a variation
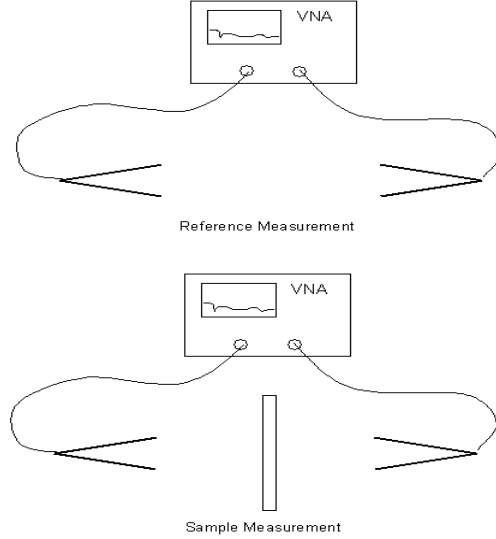
Figure 20. Free-space measurement setup of a planar sample.

of through-reflect-line (TRL). The short-circuited termination is a metal plate. Although the wave front is spherical, Muscil and Zacek [87] suggest that the electromagnetic fields can be assumed to be plane waves in the antenna far field. This assumption simplifies the inversion algorithm. The measurement may involve reflection-only data using a short circuit termination or reflection and transmission data using a specimen open on both sides. For electrically thin specimens a short-circuit termination is not useful since the tangential electric field component approaches 0 on the metal. In the case of electrically thin materials, a transmission measurement is preferred since both S_{11} and S_{21} can be used [4]. The technique lends itself well to elevated temperature measurements. In Figure 22 we show time-domain data collected on a sheet of Rexolite material.

7. Coaxial Line and Waveguide Measurement Algorithms for Permittivity and Permeability

The goal of this section is to present various approaches for obtaining both the permeability and permittivity from transmission-line scattering data. We will also overview transmission-

51
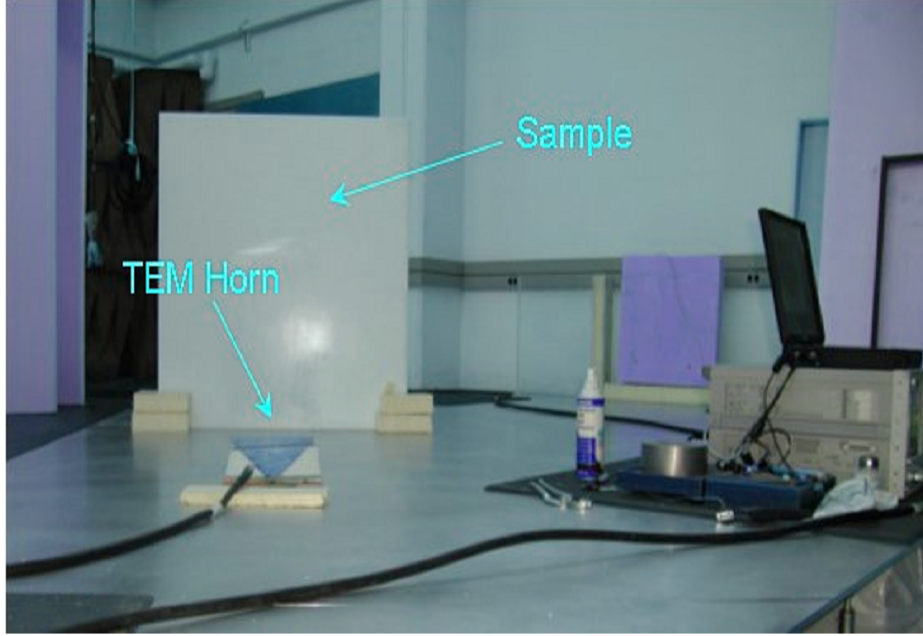
Figure 21. Picture of horn system for free-space measurement of a planar sample.

line theory for NIM materials. In the transmission/reflection (TR) measurement, a specimen is inserted into either a waveguide or a coaxial line, and the specimen is subjected to an incident electromagnetic field [see Figure 14]. The scattering equations are determined by analyzing the electric field at the specimen interfaces. In order to determine the material properties from scattering data, we must solve the electromagnetic boundary-value problem in waveguides and coaxial lines. In developing the scattering equations, only the fundamental waveguide mode (TE_{10} in waveguide and TEM in coaxial line) is assumed to propagate. Various transmission-line techniques are compared in Table 10.

7.1   Specimen Geometry and Modal Expansions

In the case of perfectly homogeneous and isotropic specimens and holders, γ is independent of the transverse coordinates. Therefore, the eigenfunctions for the transverse components in the air and specimen regions are orthogonal. In such cases, we can match fields, mode by mode, and the modal coefficients decouple. However, when the specimens and specimen holder are not perfectly formed or are slightly inhomogeneous, both μ and ϵ depend weakly on
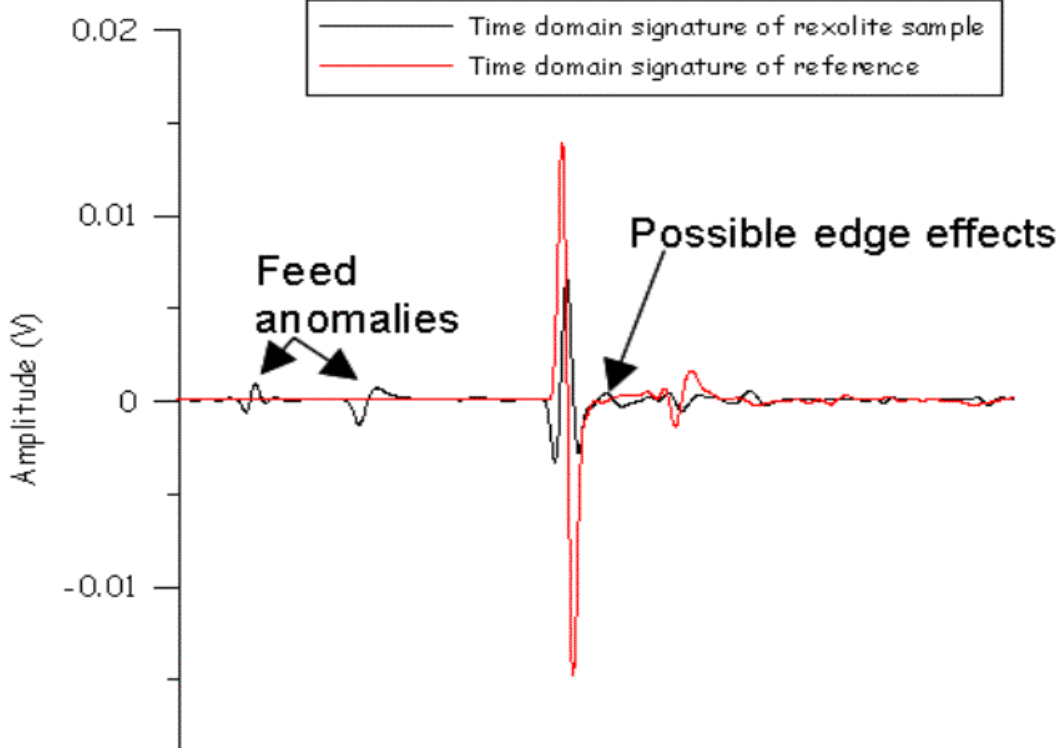
Figure 22. Time-domain data on a Rexolite slab.

the transverse coordinates of the guide and therefore the different transverse eigenfunctions in the specimen are not completely orthogonal to the transverse eigenfunctions in the air section. In such cases, the modes of imperfect specimens cannot be exactly separated and matched mode by mode. The imperfections in the specimen generate evanescent waves at the specimen-material interface. These modes may propagate in the specimen and are noticeable when they resonate, but they decay exponentially outside of the specimen. However, minor imperfections can be treated by an effective single-mode approximation we can correct for air gaps.

The fields in Regions I, II, and III of Figure 14 are found by analyzing of the electric field at the specimen interfaces. We assume that the incident electric field is the TE_{10} mode in rectangular waveguide and the TEM mode in coaxial line. If the specimen has air gaps near the electrodes or is inhomogeneous, then some of the energy carried in the wave will be converted into higher-order modes. In the following we assume that gaps or other imperfections can exist in and around the specimen. We further assume that the

53

Table 10. Dielectric and magnetic transmission/reflection (TR) measurement techniques for lossy materials.

Technique	Applicability	Advantages	Disadvantages
Full 2-port (ϵ only)	ϵ_r^* (1 MHz-30 GHz)	Requires one specimen	ϵ_r^* only
Full 2-port, one specimen	ϵ_r^*, μ_r^*	Requires one specimen	Unstable at $n\lambda_m/2$
	(1 MHz to 30 GHz)		for low-loss materials
Open-ended coaxial probe	ϵ_r^* (500 MHz to 30 GHz)	Dominant electric field	ϵ_r^* only
Capacitor	ϵ_r^* (dc to 50 MHz)	Dominant electric field	Low frequency
Shielded open circuit	ϵ_r^* (1 MHz to 30 GHz)	Dominant electric field	ϵ_r^* only
Short circuit	ϵ_r^*, μ_r^*	Dominant magnetic field	μ_r^* only
	(100 MHz to 20 GHz)		
Permeameter	μ_r^* (dc to 50 MHz)	Dominant magnetic field	Low frequency
Free space	ϵ_r^*, μ_r^* (GHz)	Nondestructive	low frequency

imperfections are limited and are such that the Laplacian can be separated into transverse and longitudinal components. If we assume that the vector component of the normalized radial electric fields E_I, E_{II}, and, E_{III}[1] in the Regions I, II, and III, we can write for N modes

$$E_I = \underbrace{\exp(-\gamma_{o1}x)}_{\text{incident wave}} + S_{11}\exp(\gamma_{o1}x) + \sum_{i=2}^{N} \underbrace{C_i\exp(\gamma_{oi}x)]}_{\text{evanescent}}, \qquad (76)$$

$$E_{II} = \sum_{i=1}^{N}[D_i\exp(-\gamma_{mi}x) + E_i\exp(\gamma_{mi}x)], \qquad (77)$$

$$E_{III} = S_{21}\underbrace{\exp(-\gamma_{o1}(x-L))}_{\text{transmitted wave}} + \sum_{i=2}^{N} \underbrace{[F_i\exp(-\gamma_{oi}(x-L))]}_{\text{evanescent}}. \qquad (78)$$

We assume that we are operating the waveguide at a frequency where only the fundamental mode is a propagating mode in the air section of the guide. The higher modes are evanescent in the air section of the guide, but may be propagating in the material-filled section. There may be additional modes produced by mode conversion for the other components of the electric field, but these are not necessary for specification of the boundary conditions. In general, the amplitudes in eqs. (76) to (78) are functions of the transverse coordinates. To find the coefficients, we must match tangential electric and magnetic fields

---

[1]TEM mode in a coaxial line or the TE_{10} mode in a waveguide (with a time dependence of $\exp(j\omega t)$ suppressed).

at the interfaces and integrate over the cross-sectional area. Various cutoff frequencies and operating frequencies are given in Tables 8 and 13.

7.2   Completely Filled Waveguide

7.2.1   Materials with Positive Permittivity and Permeability

As a special case of the formalism developed in the previous section we consider a perfectly homogeneous, isotropic specimen in a perfectly formed waveguide, as shown in Figure 14. In this case no mode conversion occurs because the eigenfunctions in the air and specimen regions are orthogonal with respect to cross-sectional coordinates. Therefore, the modes may be decoupled and the evanescent modes are not of concern. In this case we need to be concerned only with the fundamental mode in the guide. The normalized electric fields in the specimen region $x \in (0, L)$ for a coaxial line with a matched load are

$$E_I = \exp(-\gamma_o x) + S_{11} \exp(\gamma_o x), \tag{79}$$

$$E_{II} = C_2 \exp(-\gamma_1 x) + C_3 \exp(\gamma_1 x), \tag{80}$$

$$E_{III} = S_{21} \exp(-\gamma_o(x - L)). \tag{81}$$

The tangential component can be calculated from Maxwell's equations, given an electric field with only a radial component with the following boundary conditions:

$$E_I(x = 0) = E_{II}(x = 0), \tag{82}$$

$$E_{II}(x = L) = E_{III}(x = L). \tag{83}$$

The boundary condition on the magnetic field requires the additional assumption that no surface currents are generated. If this condition holds, then the tangential component of the magnetic field is continuous across the interface. The tangential component can be calculated from Maxwell's equations for an electric field with only a radial component:

$$\frac{1}{\mu_o} \frac{\partial E_I}{\partial x}(x = 0) = \frac{1}{\mu} \frac{\partial E_{II}}{\partial x}(x = 0), \tag{84}$$

$$\frac{1}{\mu} \frac{\partial E_{II}}{\partial x}(x = L) = \frac{1}{\mu_o} \frac{\partial E_{III}}{\partial x}(x = L). \tag{85}$$

For a two-port device the expressions for the measured scattering parameters are obtained by solving eqs. (76) through (78) subject to the boundary conditions.

When these equations are integrated over the cross-sectional surface area, the radial dependence is the same for each region of the waveguide.

The constants in the field equations are again determined from the boundary conditions. The boundary condition on the electric field is the continuity of the tangential component at the interfaces. The tangential component can be calculated from Maxwell's equations given an electric field with only a radial component. The higher modes in eqs. (76) to (78) are evanescent in the air-filled section of the guide. TM modes can be treated similarly. The details of the boundary matching for the TE_{10} case are described in a previous report on dielectric materials [54]. For a two-port device the expressions for the measured scattering parameters are obtained by solving eqs. (76) through (78), subject to the boundary conditions. We assume we have isotropic materials so that $S_{12} = S_{21}$. The explicit expressions for a specimen in a waveguide a distance L_1 from the port-1 reference plane to the specimen front face and L_2 from the specimen back face to the port-2 calibration plane are related by a phase rotation. The S-parameters are defined in terms of the reflection coefficient Γ and transmission coefficient Z by

$$S_{11} = R_1^2 \left[\frac{\Gamma(1 - Z^2)}{1 - \Gamma^2 Z^2} \right], \tag{86}$$

$$S_{22} = R_2^2 \left[\frac{\Gamma(1 - Z^2)}{1 - \Gamma^2 Z^2} \right], \tag{87}$$

$$S_{21} = R_1 R_2 \left[\frac{Z(1 - \Gamma^2)}{1 - \Gamma^2 Z^2} \right], \tag{88}$$

where

$$R_1 = \exp(-\gamma_o L_1) \tag{89}$$

$$R_2 = \exp(-\gamma_o L_2) \tag{90}$$

are the respective reference plane transformations. We also have an expression for the effective transmission coefficient Z:

$$Z = \exp(-\gamma L). \tag{91}$$

56

We define an effective reflection coefficient for TE and TEM modes using

$$\Gamma = \frac{\frac{\mu}{\gamma} - \frac{\mu_0}{\gamma_0}}{\frac{\mu}{\gamma} + \frac{\mu_0}{\gamma_0}} \equiv \frac{z - z_0}{z + z_0}. \tag{92}$$

For TM modes in eq. (92), replace μ/γ by γ/ϵ. For a coaxial line, the cutoff frequency approaches 0, ($\omega_c \to 0$) and therefore Γ reduces to

$$\Gamma = \frac{\frac{c_{vac}}{c_{lab}}\sqrt{\frac{\mu_r^*}{\epsilon_r^*}} - 1}{\frac{c_{vac}}{c_{lab}}\sqrt{\frac{\mu_r^*}{\epsilon_r^*}} + 1}. \tag{93}$$

Additionally, S_{21} for the empty specimen holder yields additional information

$$S_{21}^0 = R_1 R_2 \exp(-\gamma_0 L_a). \tag{94}$$

For nonmagnetic materials, eqs. (86) through (88) contain variables ϵ_r', ϵ_r'', L, and L_a, and the reference plane transformations R_1, R_2. Equations for S_{12} and S_{21} are theoretically equivalent for isotropic nongyromagnetic materials; however due to specimen inhomogeneities the measurements will not be exactly the same. We have five complex equations, eqs. (86) through (88), plus (94), plus the equation for the length of the air line $L_a = L_1 + L_2 + L$, or equivalently, 11 real equations for the 6 unknowns: ϵ_r', ϵ_r'', μ_r', μ_r'', L_1, and L_2. The equations consist of an overdetermined system for the unknowns. This abundance of information will be exploited in the next section. However, since we are dealing with isotropic materials and S_{11} and S_{22} are nearly redundant, and if we know the reference planes and sample length, then we have four equations for the four materials parameters: ϵ_r', ϵ_r'', μ_r', μ_r''.

7.2.2 Negative-Index Materials

For materials with negative real parts of the permittivity and permeability there are only slight changes from the results in the previous subsection. When the propagation coefficient $\gamma = \alpha + j\beta$ is calculated, normally the positive square root is taken for β (see eq. (4)). The real part of the impedance is always positive (note: there are very special cases where this is not true, see Reference [12], pp. 266), since the real part of the integral of the time-harmonic Poynting vector over the surface, where the energy flows through, is related to the dissipated power in the media and the radiation resistance. γ can be imaginary for propagating modes,

57

and real for evanescent modes or a combination of these. However, in NIM, if we consider the wave impedance $Z_w = j\omega\mu/\gamma = \omega(\beta\mu + j\alpha\mu)/(\alpha^2 + \beta^2)$, since the real part of the impedance is positive semi-definite and the real part of the permeability is negative, the negative square root for β in the propagation constant must be used. This is the origin of the term *negative-index materials*. However, α, which contains the material loss plus cutoff behavior, must always be positive. α can contain both effects from stored energy in the evanescent modes and losses due to dielectrics. Therefore, we require the physical solutions to have

$$Re(Z_w) \geq 0, \tag{95}$$

$$Re(\gamma) \geq 0. \tag{96}$$

Evanescent waves traveling in the $+z$ direction to ∞ must be damped. Evanescent waves in a slab may travel in both directions due to reflections. At an interface between materials the evanescent waves may be reflected and then travel in the $-z$ direction. In addition, there can be interference between attenuated waves traveling in opposite directions. The energy flow is in the direction of the Poynting vector. The phase velocity in NIM is opposite to the group velocity (backward waves). Another issue encountered when measuring NIM materials, since the material is very inhomogeneous, the thicknesses of the slab and the unit cell are not apparent. This presents a metrology problem in defining specimen thickness [88].

Pendry [89, 90] has shown that for evanescent waves entering a NIM with $\epsilon_r = \mu_r = -1$, and of thickness d, the transmission coefficient is $S_{21} = \exp(\alpha d)$. This can be obtained from eq. (88) where α for a cutoff TE waveguide is $\alpha = Re(\sqrt{k_c^2 - \omega^2\epsilon\mu})$. Therefore, for a lossless slab, energy is stored at resonance. This stored energy could be used for enhanced lens focusing. However, any loss in the material will retard this effect. This effect of stored energy is commonly called amplification of evanescent waves, but it is probably more accurate to say that there is an increase in stored energy due to resonance.

7.3 Methods for the Numerical Determination of Permittivity

7.3.1 Iterative Solutions

There are various ways of solving the scattering equations depending on the information available to the experimenter. In cases where the specimen's length and reference plane positions are known to high accuracy, taking various linear combinations of the scattering equations and solving the equations in an iterative fashion yields a very stable solution for specimens of arbitrary length. However higher-mode resonances may occur at specific frequencies. A useful combination for dielectric materials is

$$\frac{1}{2}\{[S_{12} + S_{21}] + \beta[S_{11} + S_{22}]\} = \frac{Z(1 - \Gamma^2) + \beta_1\Gamma(1 - Z^2)}{1 - Z^2\Gamma^2}, \tag{97}$$

$$S_{11}S_{22} - S_{21}S_{12} = \exp\{-2\gamma_0(L_{air} - L)\}\frac{\Gamma^2 - Z^2}{1 - \Gamma^2 Z^2}. \tag{98}$$

In eq. (97), the S-parameters to be used need to be transformed from the calibration plane to the specimen face by use of eqs. (89) and (90). Here, β_1 is a constant that varies as a function of the specimen length, plus the uncertainty in scattering parameters and loss characteristics of the material. The constant β_1 is a weighting function for the S-parameters. For low-loss materials, the S_{21} signal is strong and so we can set $\beta_1 = 0$, whereas for materials of high loss, S_{11} dominates and a large value of β_1 is appropriate. A general relation for β_1 is given by the ratio of the uncertainty in S_{21} divided by the uncertainty in S_{11}.

For cases when the positions of the reference plane are uncertain, we find that eq. (98) is robust. When we use eq. (98), no reference plane transformation need be performed since it has been eliminated by use of the relation $L_{air} = L_1 + L_2 + L$. Equation (98) works well for both low-loss and high-loss materials. That is, we have four real equations for the four unknowns: ϵ'_r, ϵ''_r, L, L_{air}.

When both the permittivity and permeability are solved for in materials with both low-loss magnetic and dielectric properties, the solutions for both permittivity and permeability will be unstable at integral multiples of one-half wavelength in the material due to TEM mode resonance.

7.3.2 Explicit Method for Nonmagnetic Materials

In the last sections we detailed an iterative method for determination of permittivity. There also are explicit methods for the case $\mu_r = 1$. Each method has its advantages and disadvantages. For the case of nonmagnetic materials there are two independent transmission-line expressions for the permittivity (see Section 7.5, eqs. (114) and (122)). Boughriet [91] has studied the second equation for permittivity. This equation is relatively stable for low-loss materials

$$\epsilon_r^* = \frac{\lambda_0^2}{\mu_r^*} \left[\frac{1}{\lambda_c^2} - \left[\frac{1}{2\pi L} \ln(\frac{1}{z}) \right]^2 \right]. \tag{99}$$

The alternative solution, which is relatively stable for high-loss materials is

$$\epsilon_r^* = \frac{c^2}{\omega^2} \left[(\frac{z+1}{z-1})^2 + \left(\frac{2\pi}{\lambda_c} \right)^2 \right], \tag{100}$$

where

$$z = \frac{\Gamma + 1}{\Gamma - 1} \tag{101}$$

7.4 Corrections to Data

Once a set of measurements is obtained we need to correct the data, taking into account systematic uncertainties. These known uncertainty sources include air gaps around specimens, waveguide wall imperfections, short-circuit and waveguide losses. Air gaps corrections are particularly important for coaxial specimens; in particular, the gap near the center conductor is important since the electric field is higher in this region. The outer air gap also contributes, but to a lesser extent. In order to make corrections we need to make precise measurements of both the specimen and the specimen holder; air gauging equipment is used to measure the air line dimensions.

7.4.1 Influence of Gaps Between Specimen and Holder

Air gaps around specimens affect the measured value of permittivity. In waveguide, the air gap along the wide side of the guide has the primary influence on the calculated permittivity since this region has a higher electric field. For the same reason as in coaxial line, the gap near the center conductor contributes more to the permittivity correction than a gap of the

same thickness near the outer conductor. These correction formulas are approximate, and generally under-correct for the effects of the air gap. Formulas for correction are given in Appendix B.

7.4.2 Attenuation Due to Imperfect Conductivity of Specimen Holders

Since no waveguide at ambient temperature is perfectly conducting, all propagating modes are attenuated to some degree. The finite conductivity of waveguide walls promotes power loss in the guide. Waveguide and coaxial line losses can be probed by measuring the scattering parameters of the empty waveguide.

The power flow propagating down the waveguide can be expressed in terms of the Poynting vector

$$P = \frac{1}{2} \int_s Re[\mathbf{E} \times \mathbf{H}^*] \cdot d\vec{S} = \frac{Z_w}{2} \int_s |\mathbf{H}_t|^2 dS, \tag{102}$$

where Z_w is the wave impedance and subscript $(_t)$ denotes the tangential component [5]. The power loss in the guide is

$$P_L = \int_c \frac{R_s}{2} |\vec{J_z}|^2 ds = \frac{R_s}{2} \int_c |\vec{H_t}|^2 ds, \tag{103}$$

where $R_s = \sqrt{\pi f \frac{\mu}{\sigma}}$ is the effective surface resistance, σ is the conductivity, and c is a closed integration path. The effective attenuation coefficient of the waveguide can be defined as

$$\alpha = \frac{P_L}{2P}. \tag{104}$$

For rectangular waveguide the integrals in eq. (103) can be performed to obtain [5]

$$\alpha_{TE_{mn}} = \frac{2R_s}{b\eta\sqrt{1 - (\frac{f_c}{f})^2}} \left[(1 + \frac{b}{a}) \left(\frac{f_c}{f}\right)^2 + \left(1 - \left(\frac{f_c}{f}\right)^2\right) \frac{\frac{b}{a}(m^2(\frac{b}{a}) + n^2)}{m^2(\frac{b}{a})^2 + n^2} \right], \tag{105}$$

where a and b are the guide dimensions, f_c is the cutoff frequency, $m, n = 0,1,2,. . .$ and η is the impedance of free space. For $n = 0$ the attenuation is

$$(\alpha)_{TE_{m0}} = \frac{R_s}{b\eta\sqrt{1 - (f_c/f)^2}} \left[1 + \frac{2b}{a}\left(\frac{f_c}{f}\right)^2\right]. \tag{106}$$

The attenuation coefficient in coaxial line is

$$\alpha_c = \frac{\epsilon'}{2}\sqrt{\frac{\omega}{2\sigma}}\left(\frac{1}{a} + \frac{1}{b}\right). \tag{107}$$

61

7.4.3 Appearance of Higher Order Modes

The field model developed in this section assumes a single mode of propagation in the specimen. At frequencies corresponding to one-half wavelength in low-loss specimens the fundamental mode will resonant. In addition, due to cutoff conditions, higher modes of propagation become possible in inhomogeneous specimens of high permittivity (usually for relative permittivities greater than about 10). Air gaps also play an important role in mode conversion. If mode conversion does occur due to some type of perturbation, then the theoretical model expounded in this section breaks down to varying degrees, particularly at resonant frequencies of these modes. The degree of breakdown of the model depends on the power coupled to the higher modes. Generally, the appearance of higher modes manifests itself as a sudden dip in $|S_{11}|$. This dip is a result of resonance of the excited higher mode. We can expect the general transmission/reflection models to break down (including the one developed in this section) for inhomogeneous specimens materials of high permittivity.

In order to minimize the effects of higher modes, shorter specimens can be used. Higher-order mode resonances have little effect if the specimen length is less than one-half guided wavelength in the material. They may still propagate in the specimen at any frequency above the cutoff of the mode.

7.4.4 Mode Suppression in Waveguides

The higher-order modes can be suppressed by mode filters. This would be particularly helpful in cylindrical waveguide. One way to do this is to helically wind a fine wire about the inner surface of a waveguide specimen holder, thus eliminating longitudinal currents and therefore TM and for example TE_{11} modes. Another approach is to insert grooves in the waveguide walls. These methods however do not work for coaxial line.

7.4.5 Uncertainty Sources and Analysis

Errors are the difference between the **true value** of a measurement and the measurement result. The **true value** is a theoretical construct. The **uncertainty** is an estimate of the region around the true value where a measurement will fall. In this section the uncertainty

incurred when using the equations expounded in this section will be estimated. The sources of error in the TR measurement include

- **Random uncertainties and error sources**
  (a) Errors in measuring the magnitude and phase of the scattering parameters
  (b) Error in specimen length
  (c) Error in reference plane positions

- **Systematic uncertainties**
  (a) Gaps between the specimen and specimen holder and specimen holder dimensional variations
  (b) Line losses and connector mismatch

Correction for errors arising from gaps around the specimen are obtained from equations available in the literature [3, 92, 93]. We assume that all measurements of permittivity have been corrected for the effects of air gaps around the specimen before the following uncertainty analysis is applied. In order to evaluate the uncertainty introduced by the measured scattering parameters, a differential uncertainty analysis is applicable with the uncertainty due to S_{11} and S_{21} evaluated separately. We assume that the total uncertainty can be written as

$$\frac{\Delta \epsilon_r'}{\epsilon_r'} = \frac{1}{\epsilon_r'} \sqrt{\left(\frac{\partial \epsilon_r'}{\partial |S_\alpha|}\Delta|S_\alpha|\right)^2 + \left(\frac{\partial \epsilon_r'}{\partial \theta_\alpha}\Delta\theta_\alpha\right)^2 + \left(\frac{\partial \epsilon_r'}{\partial L}\Delta L\right)^2 + \left(\frac{\partial \epsilon_r'}{\partial d}\Delta d\right)^2}, \qquad (108)$$

$$\frac{\Delta \epsilon_r''}{\epsilon_r''} = \frac{1}{\epsilon_r''} \sqrt{\left(\frac{\partial \epsilon_r''}{\partial |S_\alpha|}\Delta|S_\alpha|\right)^2 + \left(\frac{\partial \epsilon_r''}{\partial \theta_\alpha}\Delta\theta_\alpha\right)^2 + \left(\frac{\partial \epsilon_r''}{\partial L}\Delta L\right)^2 + \left(\frac{\partial \epsilon_r''}{\partial d}\Delta d\right)^2}, \qquad (109)$$

where $\alpha = 11$ or 21, $\Delta\theta$ is the uncertainty in the phase of the scattering parameter, $\Delta|S_\alpha|$ is the uncertainty in the magnitude of the scattering parameter, Δd is the uncertainty in the air gap around the specimen, and ΔL is the uncertainty in the specimen length. The uncertainties used for the S-parameters depend on the specific ANA used for the measurements.

The measurement bounds for S-parameter data are obtained from specifications for a network analyzer. The dominant uncertainty is in the phase of S_{11} as $|S_{11}| \to 0$. The uncertainty in S_{21} is relatively constant until $|S_{21}| \leq$ -40 dB and then increases abruptly.

In Figs. 23 and 24 the total uncertainty in ϵ_r^* computed from S_{21} and S_{11} is plotted as a function of normalized specimen length for low-loss and high-loss materials at 3 GHz with various values of ϵ_r^*, and the guided wavelength in the material given by

$$\lambda_m = \frac{2\pi}{\sqrt{\omega^2 \frac{(\sqrt{\epsilon'^2+\epsilon''^2}+\epsilon')}{2}\mu' - \left(\frac{2\pi}{\lambda_c}\right)^2}}.$$ (110)

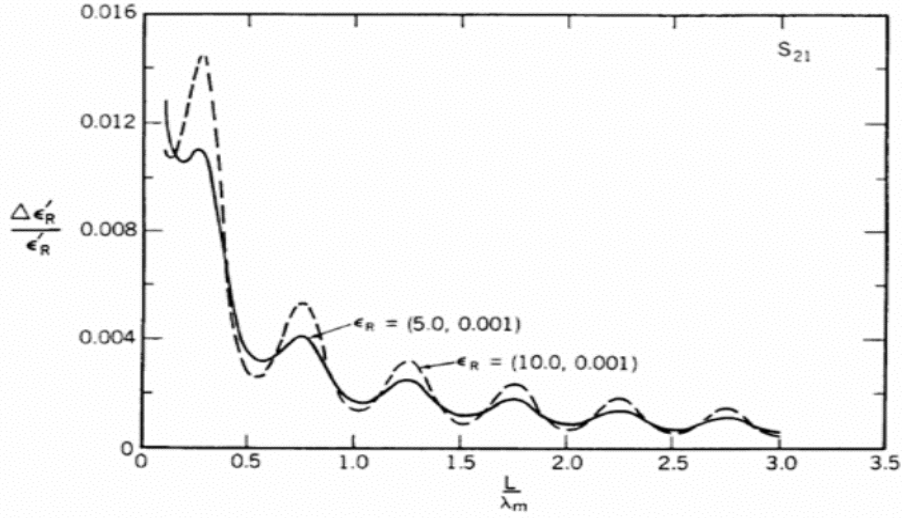In Figures 23 through 25 the uncertainty in permittivity determination is presented.

Figure 23. The uncertainty in permittivity as a function of normalized length for a low-loss specimen.

We see that the minimum uncertainty in the permittivity for low-loss dielectric materials, using the iterative procedure developed here, occurs at multiples of one-half wavelength. The reason for this can be determined by examining eqs. (86), (88) in the limit that $S_{11} \rightarrow 0, S_{21} \rightarrow 1$ with $\Gamma \neq 0$. These equations then reduce to

$$Z^2 - 1 \rightarrow 0.$$ (111)

Generally, we see a decrease in uncertainty as a function of increasing specimen length. This increase occurs because ΔS_{21} increases when the transmitted signal is less than -40 dB from the reference value. For the case of high loss the uncertainty in S_{11} approaches a constant value. This is so because for high-loss materials where the wavelength is much
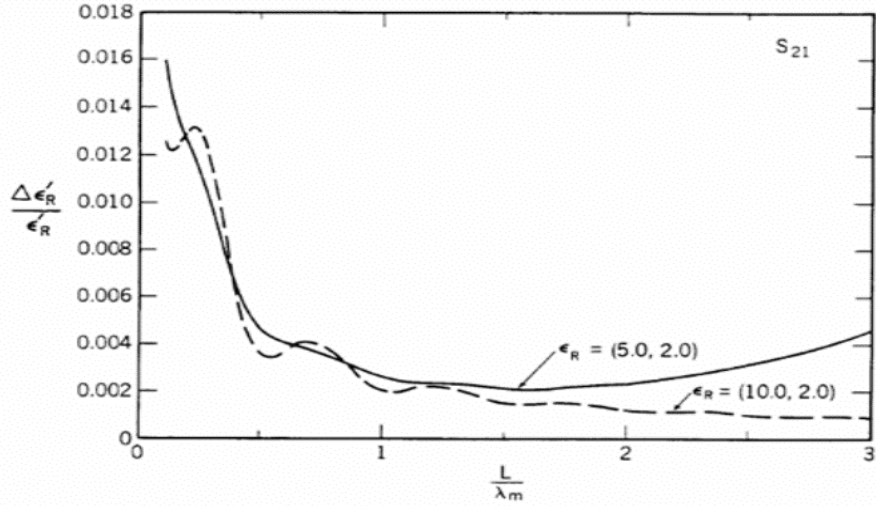
64

Figure 24. The uncertainty in permittivity as a function of normalized length for a high-loss specimen.

smaller than the specimen length; only weak signals penetrate through the specimen, and thus the front face reflection dominates the S_{11} parameter.

Also, the uncertainties in the S-parameters have some frequency dependence with higher frequencies having larger uncertainties in phase.

7.4.6 Systematic Uncertainties in Permittivity Data Related to Air Gaps

Once a set of measurements has been made, we need to correct the data for known uncertainties. Known error sources include air gaps around specimens, short-circuit and waveguide wall imperfections, together with waveguide and short-circuit losses. The wall losses can be taken into account by attenuation measurements in the guide.

Gap correction formulas that are relatively easy to implement [3, 92, 93] can be found in the literature and in Appendix B. An electrical measurement of the air gap correction can be made by using a additional resonator measurement of the same material in the frequency band of the waveguide measurement. This measurement is then used to determine the required gap in the correction formulas to match the data at that particular frequency. Waveguide losses can be corrected for by measuring the scattering parameters of the empty
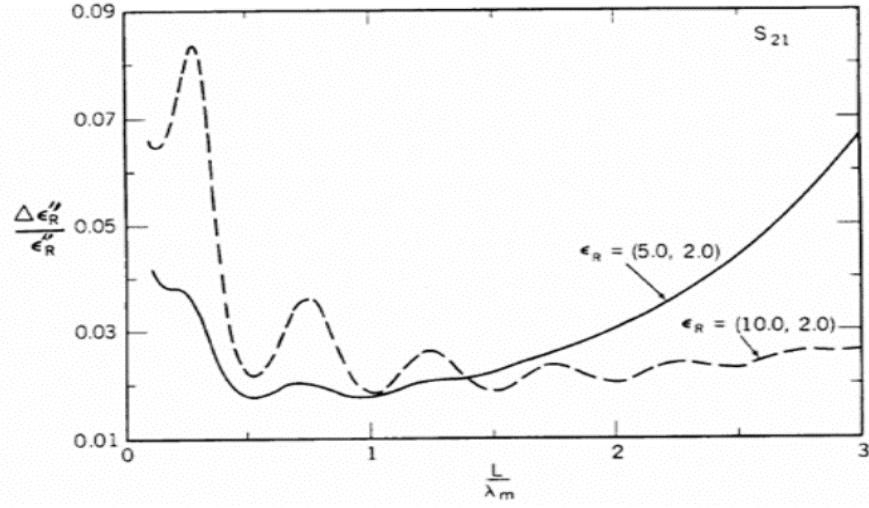
65

Figure 25. The uncertainty in imaginary part of the permittivity as a function of normalized length for a lossy specimen.

waveguide and calculating the appropriate attenuation coefficient of the guide. Also, the calculated permittivity data can be smoothed.

7.5 Permeability and Permittivity Calculation

7.5.1 Nicolson-Ross-Weir Solutions (NRW)

Nicolson and Ross [94], and Weir [56] combined the equations for S_{11} and S_{21} and developed a formula for the permittivity and permeability. Their procedure works well for frequencies away from the TEM mode resonances where the specimen length is not a multiple of one-half wavelength in the material. Near resonance, however, the method loses sensitivity for low-loss materials.

We will now develop the equations for this method.

$$Z_1 = \exp(-\gamma L). \tag{112}$$

We define a reflection coefficient for TEM and TE modes:

$$\Gamma_1 = \frac{\frac{\mu}{\gamma} - \frac{\mu_0}{\gamma_0}}{\frac{\mu}{\gamma} + \frac{\mu_0}{\gamma_0}} \equiv \frac{z - z_0}{z + z_0}. \tag{113}$$

66

For TM modes in eq. (113), replace μ/γ by γ/ϵ. Therefore

$$\frac{\mu_r^*}{\epsilon_r^*} = \left(\frac{1+\Gamma_1}{1-\Gamma_1}\right)^2. \tag{114}$$

In the NRW algorithm, the reflection coefficient is

$$\Gamma_1 = X \pm \sqrt{X^2 - 1}. \tag{115}$$

The square root sign is determined from causality in eqs. (95) and (96). Also X is given explicitly in terms of the scattering parameters where

$$X = \frac{1 - V_1 V_2}{V_1 - V_2} \tag{116}$$

and

$$V_1 = S_{21} + S_{11}, \tag{117}$$

$$V_2 = S_{21} - S_{11}. \tag{118}$$

Note that in the Nicolson-Ross solution, the S-parameters must be rotated to the plane of the specimen faces in order for the correct group delay to be calculated. The correct root is chosen in eq (115) by requiring $|\Gamma_1| \leq 1$. The transmission coefficient Z_1 for the NRW procedure is given by

$$Z_1 = \frac{S_{11} + S_{21} - \Gamma_1}{1 - (S_{11} + S_{21})\Gamma_1}. \tag{119}$$

If we define

$$\frac{1}{\Lambda^2} = -[\frac{1}{2\pi L}\ln(\frac{1}{Z_1})]^2, \tag{120}$$

then we can solve for the permeability using

$$\mu_r^* = \frac{1+\Gamma_1}{(1-\Gamma_1)\Lambda\sqrt{\frac{1}{\lambda_0^2} - \frac{1}{\lambda_c^2}}}, \tag{121}$$

where λ_0 is the free space wavelength and λ_c is the cutoff wavelength.

The permittivity is given by

$$\epsilon_r^* = \frac{\lambda_0^2}{\mu_r^*}[\frac{1}{\lambda_c^2} - [\frac{1}{2\pi L}\ln(\frac{1}{Z_1})]^2]. \tag{122}$$

In magnetic materials, eq. (120) has an infinite number of roots, because the logarithm of a complex number is multivalued. In order to pick out the correct root we need to compare

the measured group delay to the calculated group delay (L/v_g). The calculated group delay is related to the change of the wave number k with respect to the angular frequency, by analogy with the general group-velocity formula $d\omega/dk$

$$\tau_{calc.group} = L\frac{d}{df}\sqrt{\frac{\epsilon_r^*\mu_r^*f^2}{c^2} - \frac{1}{\lambda_c^2}} = \frac{1}{c^2}\frac{f\epsilon_r^*\mu_r^* + f^2\frac{1}{2}\frac{d(\epsilon_r^*\mu_r^*)}{df}}{\sqrt{\frac{\epsilon_r^*\mu_r^*f^2}{c^2} - \frac{1}{\lambda_c^2}}}L. \tag{123}$$

The measured group delay is

$$\tau_{meas.group} = -\frac{1}{2\pi}\frac{d\phi}{df}, \tag{124}$$

where ϕ is the phase of Z_1. To determine the correct root, the calculated group delays are found from eq. (123) for various values of n in the logarithm term of eq. (120), where $\ln Z_1 = \ln|Z_1| + j(\theta + 2\pi n)$, $n = 0, \pm 1, \pm 2, \cdots$. The calculated and measured group delays are compared to yield the correct value of n. For dispersionless materials the group delay is constant with frequency.

Many researchers think of the NRW solution as completely explicit. However, due to the phase ambiguity and causality constraints, it is not in the strict sense. For low-loss specimens, the NRW solution is divergent at integral multiples of one-half wavelength in the specimen. This occurs because the phase of S_{11} cannot be accurately measured for small $|S_{11}|$. Also in this limit both of the scattering equations reduce to the relation $Z_1^2 \to 1$, which is a relation for only the phase velocity and therefore solutions for ϵ_r^* and μ_r^* are not separable. This singular behavior can be minimized in cases where permeability is known *a priori*, as shown in previous work performed by Baker-Jarvis [54].

For magnetic materials there are other methods for solution of the S-parameter equations. In the next section we will describe various solution procedures. A comparison of the Nicolson-Ross results for the permittivity of Teflon compared to the iterative permittivity from eq. (97) is given in Figure 26.

7.5.2   Modified Nicolson-Ross: Reference-Plane Invariant Algorithm

In measurements, keeping the sample faces at the reference planes is difficult. Therefore an algorithm that is independent of the reference planes would be very useful.
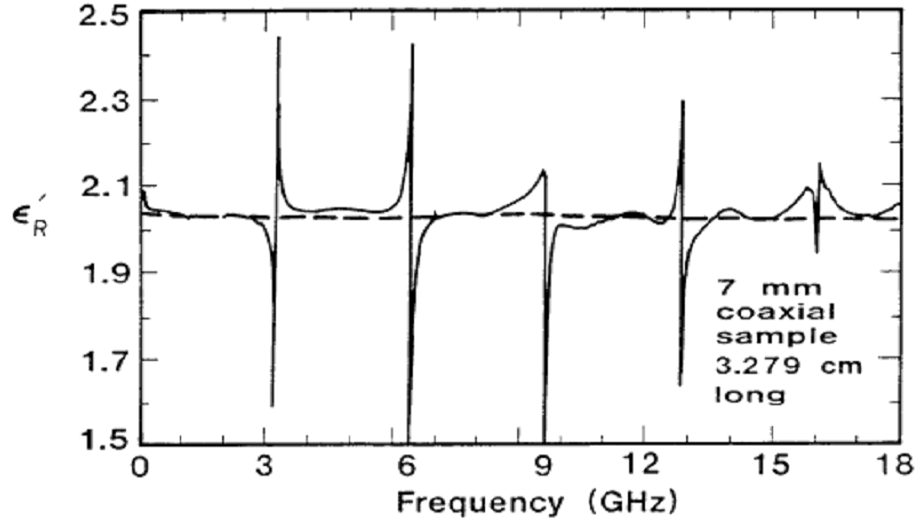
Figure 26. The results of permittivity as a function of frequency using the Nicolson-Ross algorithm versus eq. (97).

In order to obtain both the permittivity and the permeability from the S-parameter relations, we can have at least two independent measurements. Most commonly we use a two-port measurement of S_{11} and S_{21} on one specimen , or a one-port SCL measurement of a specimen at two different positions in the line. Alternatively, we can use independent measurements of two specimens of different lengths. In the full S-parameter solution developed, we solve equations that are invariant to reference planes for ϵ and μ. This is an enhancement over the Nicolson-Ross equations. A set of equations for single-specimen magnetic measurements is eqs. (97) and (98). The LHS of eq. (98) is the determinant of the scattering matrix.

7.5.3 Iterative Solution

Equations (97) and (98) can be solved either iteratively, or by a technique similar to the NRW technique. In an iterative approach, Newton's numerical method for root determination works quite well. To solve the system we can separate the system into four real equations. The iterative solution works well if good initial guesses are available.

69

7.5.4　Explicit Solution

We can also possible to obtain an explicit solution to eqs. (97) and (98). Let $x = (S_{21}S_{12} - S_{11}S_{22})\exp\{2\gamma_0(L_{air} - L)\}$ and $y = \{(S_{21} + S_{12})/2\}\exp\{\gamma_0(L_{air} - L)\}$: then we can show that the roots for the transmission coefficient are $Z = \pm 1$ and

$$Z = \frac{x+1}{2y} \pm \sqrt{\left(\frac{x+1}{2y}\right)^2 - 1}. \tag{125}$$

The correct roots are selected such that eqs. (95) and (96) are satisfied. The reflection coefficient is

$$\Gamma_2 = \pm\sqrt{\frac{x - Z^2}{xZ^2 - 1}} \equiv \frac{z - z_0}{z + z_0} \equiv \frac{\frac{\mu}{\gamma} - \frac{\mu_0}{\gamma_0}}{\frac{\mu}{\gamma} + \frac{\mu_0}{\gamma_0}}. \tag{126}$$

For TM modes replace μ/γ by γ/ϵ in eq. (126).

The ambiguity in the plus-or-minus sign in eq. (126) can be resolved as for Z. The permeability and permittivity are then

$$\mu_r^* = -\frac{1 + \Gamma_2}{1 - \Gamma_2}\frac{1}{\gamma_0 L}(\ln Z + j2\pi n), \tag{127}$$

$$\epsilon_r^* = \frac{c^2}{\omega^2}[(\frac{2\pi}{\lambda_c})^2 - \frac{1}{L^2}(\ln Z + j2\pi n)^2]/\mu_r^*. \tag{128}$$

The correct value of n is selected using the group delay comparison, as described in the Nicolson-Ross-Weir technique. Usually we fit the measured group delay around a specific point by a least-squares polynomial. At low frequencies and low permittivity the correct roots are more easily identified since they are more widely spaced. However, high-permittivity materials have many possible roots and discerning the correct n in the logarithm is sometimes difficult.

7.5.5　NIM Parameter Extraction

For NIM, the correct sign on the index of refraction is required. In these measurements we can use eq. (125) to obtain the index of refraction. As previously, the correct roots must be selected by requiring that the real part of $j\omega\mu/\gamma \geq 0$ and $Re(\gamma) \geq 0$. Also, the correct branch of the logarithm function must be determined through the group delay, as discussed previously for other methods.

7.5.6 Measurement Results

The measurement consists of inserting a well-machined specimen into a coaxial line or waveguide and measuring the scattering parameters. For waveguide measurements we need to have a section of waveguide of length about two free-space wavelengths between the coax-to-waveguide adapter and the specimen holder. This acts as a mode filter for damping evanescent modes. There are many roots to the equations for the permeability and permittivity, and caution must be exercised when selecting the correct root. At lower frequencies (less than 1 GHz), the roots are usually more widely spaced and therefore root selection is simplified. Another approach to root selection is to measure two specimens of differing lengths, where the results are compared to determine the correct root. In Figure (27), we show data on 7 mm coaxial line-measurements on several polymer materials. For comparison purposes, the corresponding measurements of permittivity and loss tangent on the same materials at 10 GHz using a highly-accurate dielectric resonator are Teflon: $(2.05 \pm 0.02, 2 \times 10^{-4} \pm 8 \times 10^{-5})$, Rexolite: $(2.54 \pm 0.01, 4 \times 10^{-4} \pm 8 \times 10^{-5})$, Nylon: $(3.04 \pm 0.02, 7 \times 10^{-3} \pm 8 \times 10^{-5})$, PMMA: $(2.61 \pm 0.02, 5 \times 10^{-3} \pm 8 \times 10^{-5})$, polyvinylchloride(PVC): $(2.70 \pm 0.02, 5 \times 10^{-3} \pm 8 \times 10^{-5})$.
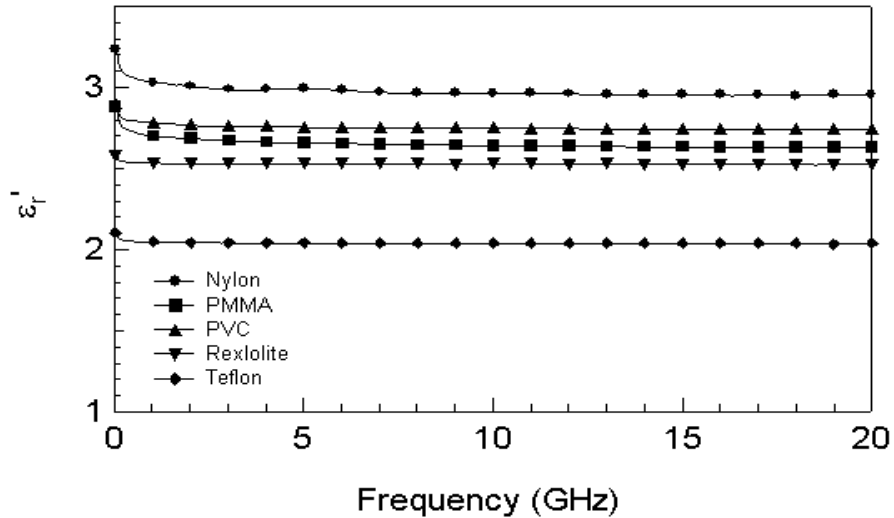

Figure 27. Measurements of ϵ_r' on polymers.
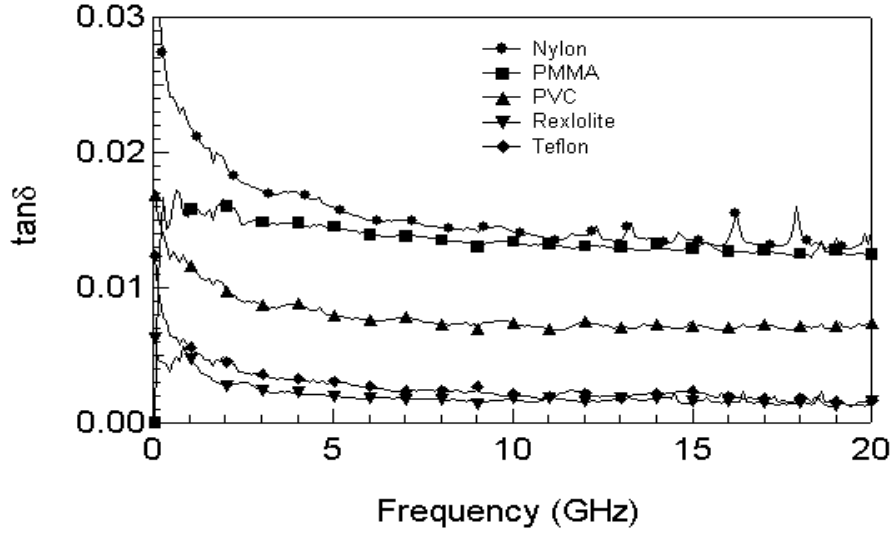
Figure 28. Measurements of $\tan\delta$ on polymers.

7.5.7 Measurements of Magnetic Materials

Waveguide measurement data on magnetically loaded polymers are given in Figures 29 through 32 using the full iterative and explicit S-parameter techniques. The measurements reported in this section have not been corrected for gaps around the specimen. The effect of the air gaps is a bias in measured values of the material parameters that are below the actual values. In the next section we will discuss ways of mitigating the effects of air gaps on measurements.

7.5.8 Effects of Air Gaps Between the Specimen and the Waveguide for Magnetic Materials

Systematic uncertainties due to air gaps between the specimen holder and the specimen may be either corrected with the formulas given in the Appendix C or mitigated using a conducting paste can be applied to the external surfaces of the specimen that are in contact with the specimen holder.

Figure 29. ϵ_r' of a loaded polymer in an X-band waveguide with the full S-parameter iterative technique.
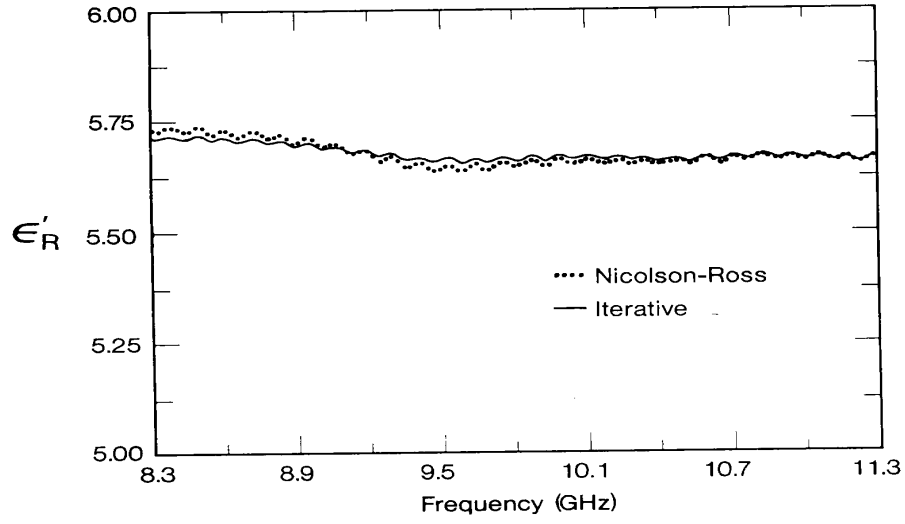

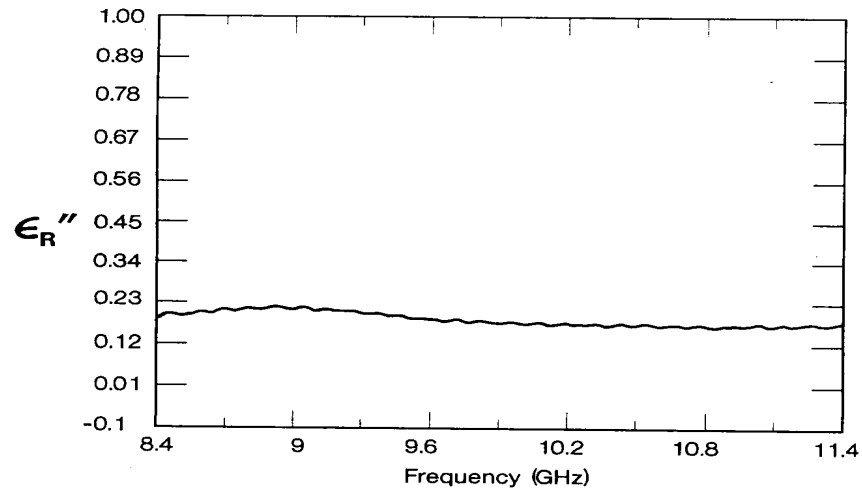Figure 30. ϵ_r'' of a loaded polymer in an X- band waveguide with the full S-parameter iterative technique.
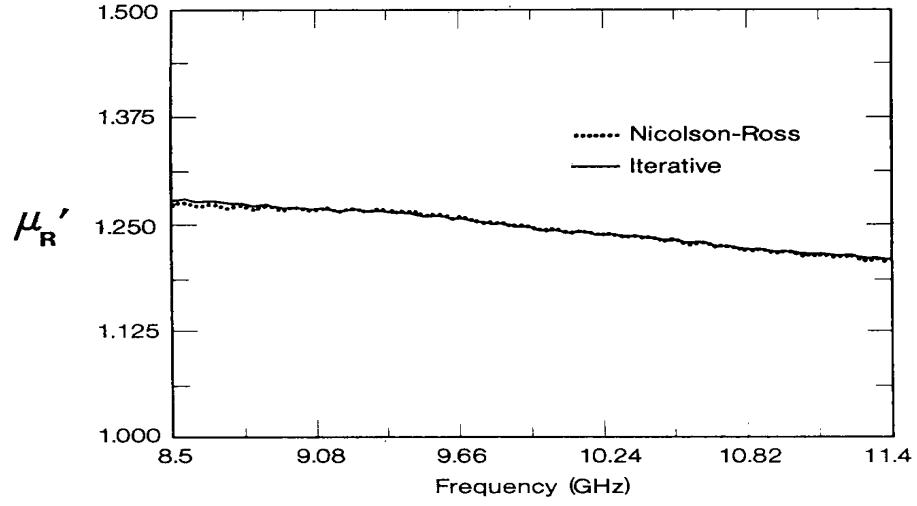
Figure 31. μ_r' of a ferrite loaded polymer in an X-band waveguide with the full S-parameter iterative technique.
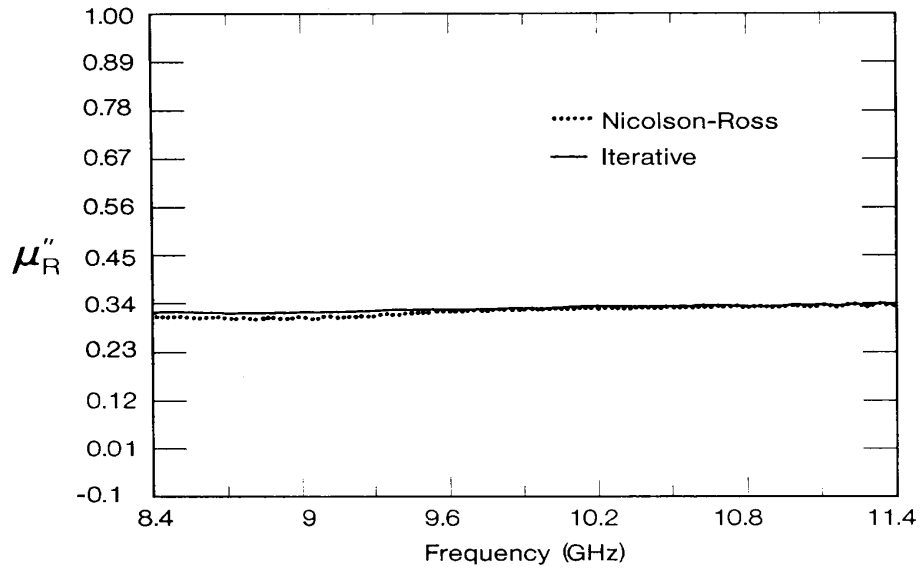

Figure 32. μ_r'' of a ferrite loaded polymer in an X-band waveguide with the full S-parameter iterative technique.

7.6 Uncertainty Determination of Combined Permittivity and Permeability Measurements in Waveguide

7.6.1 Independent Sources of Uncertainty for Magnetic Measurements

In this section an uncertainty analysis is presented. The complete derivations of the uncertainty equations are given in [4]. The sources of error in the permeability and permittivity TR measurement include

- Uncertainties in measuring the magnitude and phase of the scattering parameters

- Gaps between the specimen and specimen holder

- Specimen holder dimensional variations

- Uncertainty in specimen length

- Line losses and connector mismatch

Techniques for correcting for uncertainties arising from gaps around the specimen are given in Appendix B [95–100]. We assume that all measurements of permittivity have been corrected for air gaps around the specimen before the uncertainty analysis is applied. In coaxial line, the permeability is less affected by air gaps than the permittivity since the magnetic field is tangential to the air gap and therefore there is less stored magnetic energy in the air-gap region when compared to a magnetic field normal to the air gap. In order to evaluate the uncertainty introduced by the measured scattering parameters and specimen dimensions, a differential uncertainty analysis is assumed applicable with the uncertainty due to S_{11} and S_{21} evaluated separately. We assume that the S-parameters are functions of $S_{ij}(|S_{11}|, |S_{21}|, \theta_{11}, \theta_{21}, L, d)$. The root-sum-of-squares (RSS) uncertainties for the physically measured parameters are

$$\frac{\Delta\epsilon_r'}{\epsilon_r'} = \frac{1}{\epsilon_r'}\sqrt{\sum_\alpha \left[\left(\frac{\partial\epsilon_r'}{\partial|S_\alpha|}\Delta|S_\alpha|\right)^2 + \left(\frac{\partial\epsilon_r'}{\partial\theta_\alpha}\Delta\theta_\alpha\right)^2\right] + \left(\frac{\partial\epsilon_r'}{\partial L}\Delta L\right)^2 + \left(\frac{\partial\epsilon_r'}{\partial d}\Delta d\right)^2}, \quad (129)$$

$$\frac{\Delta\epsilon_r''}{\epsilon_r''} = \frac{1}{\epsilon_r''}\sqrt{\sum_\alpha \left[\left(\frac{\partial\epsilon_r''}{\partial|S_\alpha|}\Delta|S_\alpha|\right)^2 + \left(\frac{\partial\epsilon_r''}{\partial\theta_\alpha}\Delta\theta_\alpha\right)^2\right] + \left(\frac{\partial\epsilon_r''}{\partial L}\Delta L\right)^2 + \left(\frac{\partial\epsilon_r''}{\partial d}\Delta d\right)^2}, \quad (130)$$

where $\alpha = 11$ or 21, $\Delta\theta$ is the uncertainty in the phase of the scattering parameter, $\Delta|S_\alpha|$ is the uncertainty in the magnitude of the scattering parameter, Δd is the uncertainty in the air gap around the specimen, and ΔL is the uncertainty in the specimen length. The Δ indicates one standard deviation in the independent variable. The derivatives with respect to air gap, $\partial\epsilon'_r/\partial d$, have been presented previously [54]. The uncertainties used for the S-parameters depend on the specific ANA used for the measurements. This type of uncertainty analysis assumes that changes in independent variables are sufficiently small that a Taylor series expansion is valid. Of course there are many other uncertainty sources of lesser magnitude such as repeatability of connections and torquing of flange bolts. Estimates for these uncertainties could be added to the uncertainty budget.

7.6.2 Measurement Uncertainty for a Specimen in a Transmission Line

The measurement bounds for S-parameter data are obtained from specifications for a network analyzer. The dominant uncertainty is in the phase of S_{11} as $\mid S_{11} \mid \rightarrow 0$. The uncertainty in $|S_{21}|$ is relatively constant until $|S_{21}| \leq -50$ dB, when it increases abruptly.

In Figures 33 and 34, the total uncertainty in ϵ_r^* and μ_r^*, computed from S_{21} and S_{11} is plotted as a function of normalized specimen length.

In Figures 33 and 34, the uncertainty due to the gap correction is not included, nor are there uncertainties included for connector repeatability or flange bolt torquing. The maximum uncertainty for low-loss materials occurs at multiples of one-half wavelength. Generally, we see a decrease in uncertainty as a function of increasing specimen length. Also, the uncertainties in the S-parameters have some frequency dependence, with higher frequencies having larger uncertainties in phase.

7.7 Uncertainty in the Gap Correction

The correction for an air gap between the wall of the specimen holder and specimen is very important for measurements of high-permittivity materials. In addition, the uncertainty in the gap correction is very important for high permittivity materials and may actually dominate the uncertainties of the measurement. In this section the uncertainty in the gap

76

Figure 33. The relative uncertainty in $\epsilon'_r(\omega)$ for a low-loss material as a function of normalized length, with $\mu^*_r = (2, 0.05)$, $\epsilon^*_r = (10, 0.05)$ and $(5, 0.05)$.

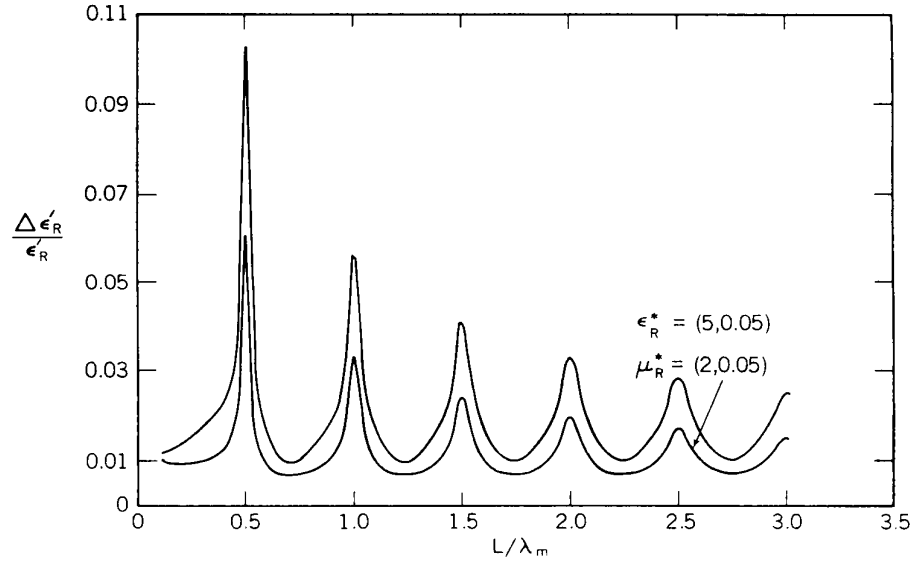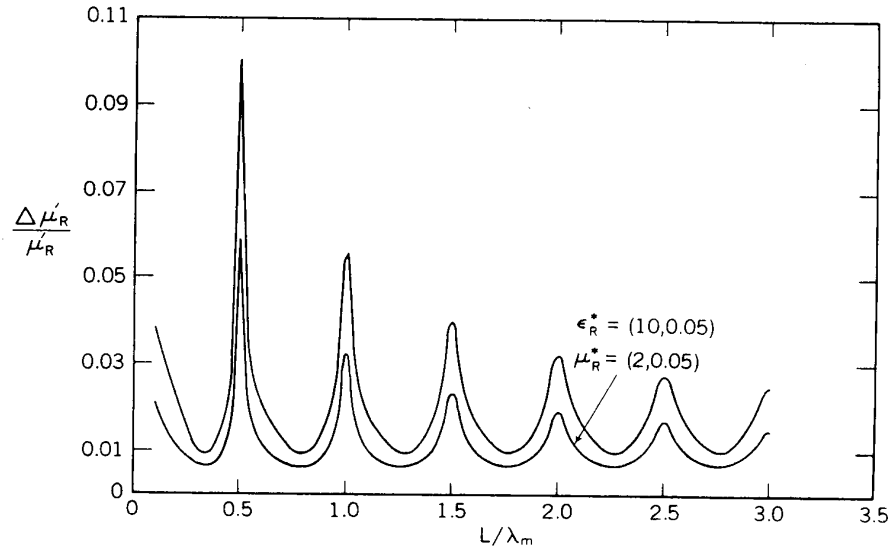Figure 34. The relative uncertainty in $\mu'_r(\omega)$ for a low-loss material as a function of normalized length, with $\mu^*_r = (2, 0.05)$, $\epsilon^*_r = (10, 0.05)$ and $(5, 0.05)$.

correction will be worked.

7.7.1 Waveguide Air-Gap Uncertainty for Dielectrics

The uncertainty due to an air gap between specimen and holder can be calculated from the partial derivatives of ϵ_r^* with respect to gap thicknesses, d. The relevant derivatives for waveguide are given by

$$\frac{\partial \epsilon'_{cR}}{\partial d} = \epsilon'_{mR}\left[\frac{1}{b - (b-d)\epsilon'_{mR}}\right] - \epsilon'^2_{mR}\frac{d}{[b - (b-d)\epsilon'_{mR}]^2}, \tag{131}$$

$$\frac{\partial \epsilon''_{cR}}{\partial d} = -\epsilon''_{mR}\epsilon'_r \frac{b}{[b - (b-d)\epsilon'_{mR}]^2}. \tag{132}$$

7.7.2 Coaxial Air-Gap Correction for Dielectrics

For coaxial line the relevant derivatives are given by

$$\frac{\partial \epsilon'_{cR}}{\partial R_2} = -\epsilon'_{mR}\frac{1}{R_2(L_3 - \epsilon'_{mR}L_1)} + \epsilon'^2_{mR}\frac{L_2}{R_2(L_3 - \epsilon'_{mR}L_1)^2}, \tag{133}$$

$$\frac{\partial \epsilon'_{cR}}{\partial R_3} = \epsilon'_{mR}\frac{1}{R_3(L_3 - \epsilon'_{mR}L_1)} + \epsilon'^2_{mR}\frac{L_2}{R_3(L_3 - \epsilon'_{mR}L_1)^2}, \tag{134}$$

$$\frac{\partial \epsilon''_{cR}}{\partial R_2} = \epsilon''_{mR}\epsilon'_{mR}\left[\frac{1}{L_2 R_2} + \frac{L_1}{L_2^2 R_2}\right], \tag{135}$$

$$\frac{\partial \epsilon''_{cR}}{\partial R_3} = -\epsilon''_{mR}\epsilon'_{mR}\left[\frac{1}{L_2 R_3} + \frac{L_1}{L_2^2 R_3}\right]. \tag{136}$$

where

$$L_1 = \ln\frac{R_2}{R_1} + \ln\frac{R_4}{R_3}, \tag{137}$$

$$L_2 = \ln\frac{R_3}{R_2}, \tag{138}$$

$$L_3 = \ln\frac{R_4}{R_1}. \tag{139}$$

8. Short-Circuited Line Methods

8.1 Theory

In this section we review the mathematical formalism for short-circuit measurements and develop a measurement algorithm. We consider a measurement of the reflection coefficient
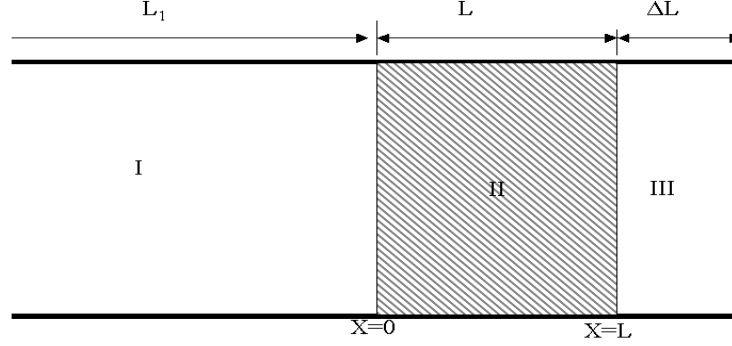
Figure 35. A transmission line with a short-circuit termination.

(S_{11} for a shorted two-port) as a function of frequency. We begin with a mathematical analysis of the electromagnetic fields in the specimen (see Figure 35). The details of the field model have been presented previously [54] and only the most essential details will be presented here. In terms of hyperbolic functions, the reflection coefficient is

$$\Gamma = \frac{\tanh\gamma L + \beta\tanh\gamma_0\Delta L - \beta(1 + \beta\tanh\gamma L\tanh\gamma_0\Delta L)}{\tanh\gamma L + \beta\tanh\gamma_0\Delta L + \beta(1 + \beta\tanh\gamma L\tanh\gamma_0\Delta L)}. \tag{140}$$

Although in the derivation of eq. (140), we assumed that the specimen plane coincides with the measurement calibration plane, this is not in general the case; however, we can transform the reference plane position by a simple procedure. To accomplish this, we write the most general expression for the reflection coefficient as

$$\Gamma_{11(trans)} = R_1^2\Gamma, \tag{141}$$

where $\Gamma_{11trans}$ is the reflection coefficient at the calibration reference plane position,

$$R_1 = \exp(-\gamma_o L_1), \tag{142}$$

and L_1 is the distance from the calibration plane to the specimen front face. Equation (141) transforms the reflection coefficient from the calibration plane to the plane of the specimen's front face. For many applications we wish to eliminate the distance L_1 from eq. (141). This can be accomplished by measuring Γ_{empty} of the empty specimen holder,

$$\Gamma_{empty} = -\exp(-2\gamma_o[L_1 + \Delta L + L]) = -\exp(-2\gamma_0 L_{air}), \tag{143}$$

79

and consequently the ratio of the filled to empty holder reflection coefficient is

$$\frac{\gamma_{11(trans)}}{\Gamma_{empty}} = -\exp(2\gamma_0[\Delta L + L])\Gamma. \tag{144}$$

If both the permeability and the permittivity are required, measurement data for two different short-circuit positions are needed. Note that standing waves can be formed in the region between the specimen and short-circuit and between the calibration plane and specimen's front face. Therefore, certain frequencies, depending on specimen length and the other lengths, will give better results for permittivity, whereas other frequencies will yield better results for permeability.

The position of the short circuit for a coaxial line is in a low electric field and high magnetic field region, and a position $\lambda/4$ from the short- circuit is a high electric field and low magnetic field region. Therefore, as frequency permits, for permittivity measurements the specimen should be moved away from the short-circuit termination. Permeability in isolation can be obtained with the specimen at the short-circuit position. This depends on the sample thickness and the wavelength. Of course when an ANA is used measurements will be taken at many combinations of field strengths and therefore the uncertainty will vary with frequency. A limitation of the SCL method is that the electric field will be very small over the entire waveguide section at low frequencies. Therefore dielectric materials are difficult to measure at low frequencies in a SCL system.

8.2   Measurements

In the SCL technique the scattering parameter S_{11} is measured broadband, with the specimen at a given position in the specimen holder. The distance from the specimen to the short-circuit termination must be known to a high degree of accuracy. If both permeability and the permittivity are required then the specimen must be moved in the line and the S-parameters again measured.

Depending on the position of the short circuit, the specimen may be immersed in either a region of high electric field or high magnetic field. A strong electric field is advantageous for determination of permittivity, whereas a strong magnetic field is advantageous for permeability determination. Generally, the specimen end will be in a region of high magnetic

80
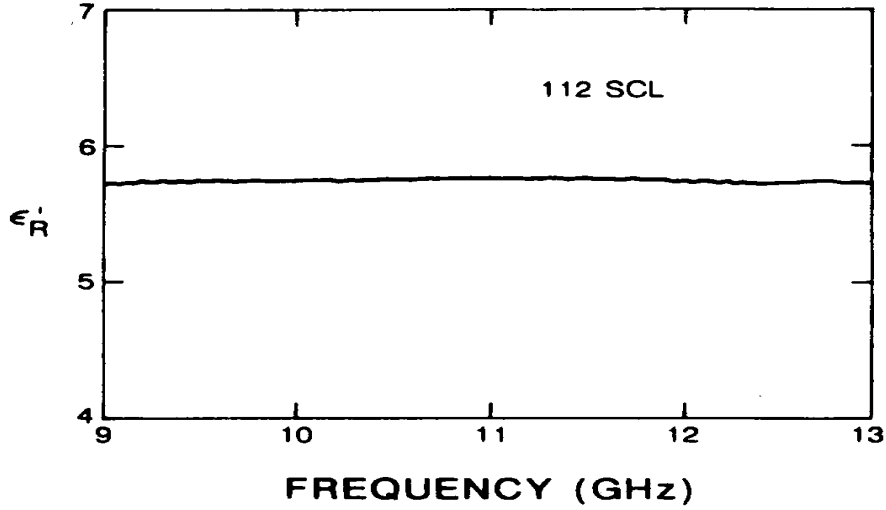
Figure 36. ϵ'_r without gap correction using SCL for a loaded polymer mixture.

field when the specimen is in closest physical contact with the short. We can take advantage of the fluctuating electric and magnetic field distributions when measuring permittivity and permeability. When taking broadband measurements on an ANA we can predict when the specimen is immersed in the various field strengths. Then one can select the measurements to be used for permittivity and permeability calculations [93].

Measurements were made on an ANA for various specimens. Using eq. (140) we obtained the permittivity and permeability data shown in Figures 36 and 37.

9.   Permeameters for Ferrites and Metals

9.1   Overview of Permeameters

In the past, permeameters have been used for low-frequency measurements on medium-high permeability materials. For ferrites, the skin depth is large and is easier to model than in metals where it is only a fraction of a millimeter. Therefore we use different approaches for metals versus ferrites or other resistive materials. Rasmussen et al. [101], Hoer and Rasmussen [102], Powell and Rasmussen [103], and Goldfarb and Bussey [58] have all described various ferrite permeameter designs. The conductivity of metals can be measured

81
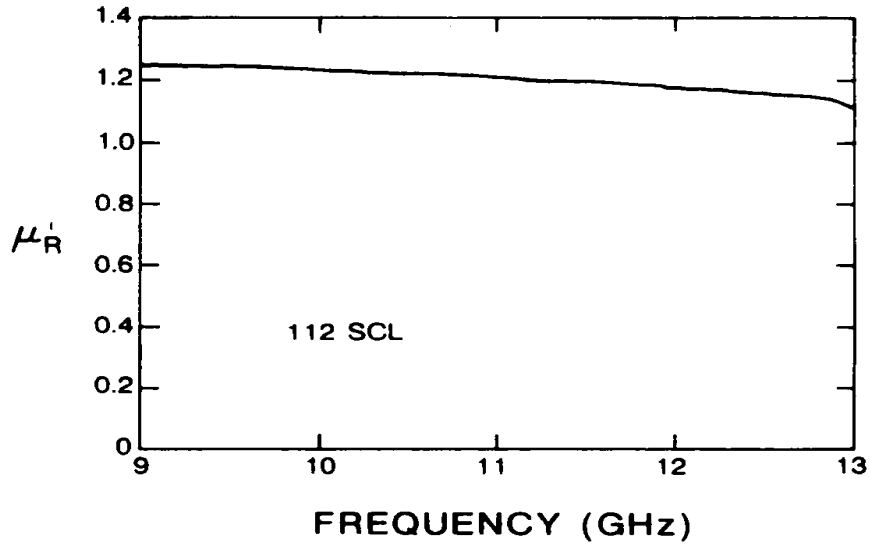
Figure 37. μ'_r without gap correction using SCL for a loaded polymer mixture.

with a four-probe system using voltmeters. An overview of this technique is given in [104]. Alexander et al. [105] have studied permeameters for ferromagnetic and ferrite thin films.

9.2   Permeability of Metals

For metals, the characterization of the electrical properties includes the surface resistance, conductivity, and permeability. The high-frequency surface resistance can be determined by end-plate substitution methods [106]. For metals, an accurate way to measure permeability is to wind a toroidal specimen with wire and measure changes in inductance as shown in Figure 38. These types of measurements are summarized in [104]. The main difficulty with these measurements is that the skin depth is short and needs to be included in the model. If a toroidal specimen is inserted into a region containing an azimuthal magnetic field, the inductance is changed. If the inductance of the empty specimen holder is compared to the inductance of the filled holder then we can extract the complex permeability of the material. At very low frequencies, if the skin depth is much larger than the sample size, it need not be modeled.

82
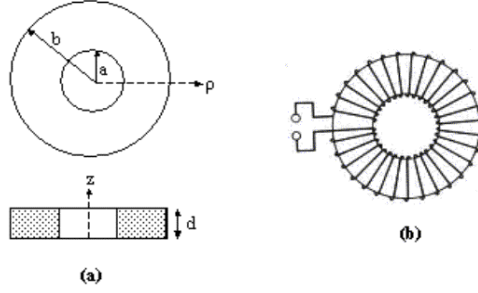
Figure 38. Toroid wiring over metal or ferrite core.

9.3   Ferrites and Resistive Materials

For magnetic materials such as ferrites at low frequencies, the skin depth usually is not important in the measurement. We consider a magnetic toroid in a short-circuited coaxial line. For long wavelengths near the short circuit we have a strong, relatively uniform, magnetic field. In such cases the following simple model can be used to determine the permeability. Consider a toroid of inner diameter a and outer diameter b and height h at low frequencies (depending on properties, for frequencies < 100 MHz). The material contributes an inductance of [58]

$$\mathcal{L}_m = \frac{\mu' h \ln(b/a)}{2\pi} \tag{145}$$

and the inductance of the air space taken up by the toroid is

$$\mathcal{L}_a = \frac{\mu_0 h \ln(b/a)}{2\pi}. \tag{146}$$

The net change in the specimen inductance when the specimen is inserted into the holder is

$$\Delta \mathcal{L} = \mathcal{L}_m - \mathcal{L}_a \tag{147}$$

and therefore

$$\mu'_r = 1 + \frac{2\pi \Delta \mathcal{L}}{\mu_0 h \ln(b/a)}. \tag{148}$$

83
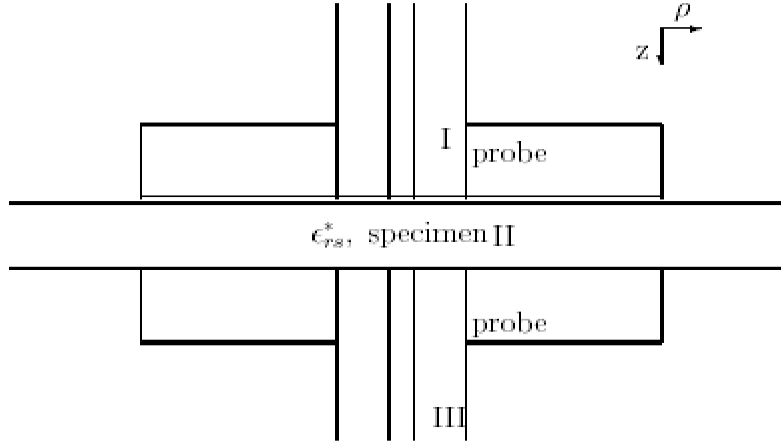
Figure 39. Two open-ended coaxial probes with specimen inserted.

The magnetic loss may be obtained from consideration of the core loss ΔR or resistance

$$\mu_r'' = \frac{\Delta R}{\mu_0 f h \ln(b/a)}.$$ (149)

10.   Other Transmission-Line Methods

10.1   Two-Port for Thin Materials and Thin Films

10.1.1   Overview

We can use two coupled coaxial probes to monitor the dielectric properties of thin materials. The two-port measurement fixture is depicted in Figure 39. In this case there may be transmission as well as reflection. An analytical solution for this problem has been derived previously [107].

The scattering parameters can be obtained by matching tangential field components at interfaces. The analytical solution follows the same line of reasoning used in the full-field single coaxial probe problem. Experimental results indicate that this method is useful for broadband material measurements on thin materials.

10.1.2 Scattering Parameters

The scattering parameters may be constructed if we match at the material-conductor interfaces, the Hankel transforms of Helmholtz equation for the electric and magnetic fields, solve for coefficients, and then take inverse transforms. In particular, two independent vector relations can be obtained

$$\mathbf{Q}_1 \vec{S}_{11} + \mathbf{Q}_2 \vec{S}_{21} = \vec{P}_1 \tag{150}$$

and

$$\mathbf{Q}_2 \vec{S}_{11} + \mathbf{Q}_1 \vec{S}_{21} = \vec{P}_2. \tag{151}$$

Here $\vec{S}_{11}$ and $\vec{S}_{21}$ are the reflection and transmission vectors. The components of the matrices are

$$Q_{1mn} = \delta_{mn} + \frac{\epsilon_2^* \gamma_{n(c)}}{\epsilon_c^*} \int_0^\infty \frac{\zeta D_n D_m (\exp(2\gamma_2 d) + 1)}{\gamma_s (\exp(2\gamma_2 d) - 1)} d\zeta, \tag{152}$$

$$Q_{2mn} = -2 \frac{\epsilon_2^* \gamma_{n(c)}}{\epsilon_c^*} \int_0^\infty \frac{\zeta D_n D_m \exp(\gamma_2 d)}{\gamma_2 (\exp(2\gamma_2 d) - 1)} d\zeta, \tag{153}$$

$$P_{1n} = \delta_{n0} - \frac{\epsilon_2^* \gamma_{n(c)}}{\epsilon_c^*} \int_0^\infty \frac{\zeta D_n D_0 (\exp(2\gamma_2 d) + 1)}{\gamma_2 (\exp(2\gamma_2 d) - 1)} d\zeta. \tag{154}$$

The propagation constants are $\gamma_{n(c)} = \sqrt{k_{n(c)}^2 - (\omega/c)^2 \epsilon_{rc}^* \mu_{rc}^*}$, where $k_{n(c)}$ are cutoff wavenumbers and subscript (c) denotes a coaxial line. Note that all of the TM_{0n} modes are evanescent. Also $\gamma_2 = j\sqrt{k_2^2 - \zeta^2}$, if $\Re(k_2) > \zeta$, and $\gamma_2 = \sqrt{\zeta^2 - k_2^2}$ if $\Re(k_2) < \zeta$. Also R_m are radial eigenfunctions given by eq. (184). Further,

$$P_{2n} = \frac{\epsilon_2^* \gamma_{n(c)}}{\epsilon_c^*} \int_0^\infty \frac{2 D_0 D_n \zeta \exp(\gamma_2 d)}{\gamma_2 (\exp(2\gamma_2 d) - 1)} d\zeta \tag{155}$$

for $m, n = 1, 2, ..., N$. The coefficients are calculated from the eigenfunctions R_n (see eq. (161)) in the coaxial line of outer dimension b and inner dimension a

$$D_n(\zeta) = \int_a^b \rho J_1(\zeta\rho) R_n(\rho) d\rho \tag{156}$$

can be found analytically. For $n = 0$,

$$D_0(\zeta) = \frac{1}{\sqrt{\ln b/a}} \int_a^b J_1(\zeta\rho) d\rho = \frac{1}{\sqrt{\ln b/a}} \frac{1}{\zeta} [J_0(\zeta a) - J_0(\zeta b)] \tag{157}$$

85

and otherwise

$$D_n(\zeta) = \int_a^b \rho R_n(\rho) J_1(\zeta\rho) d\rho$$
$$= \frac{2}{\pi} \frac{C_n}{k_{n(c)}} \frac{1}{J_0(k_{n(c)}b)} \frac{\zeta}{k_{n(c)}^2 - \zeta^2} [J_0(\zeta b) J_0(k_{n(c)}a) - J_0(\zeta a) J_0(k_{n(c)}b)]. \tag{158}$$

Straightforward matrix manipulation of eqs.(150) and (151), assuming that no singular matrices or inverses are encountered, yields the following solution for the forward problem:

$$\vec{S}_{21} = [\mathbf{Q}_1 - \mathbf{Q}_2\mathbf{Q}_1^{-1}\mathbf{Q}_2]^{-1}(\vec{P}_2 - \mathbf{Q}_2\mathbf{Q}_1^{-1}\vec{P}_1), \tag{159}$$

and

$$\vec{S}_{11} = \mathbf{Q}_1^{-1}(\vec{P}_1 - \mathbf{Q}_2\vec{S}_{21}). \tag{160}$$

The first components in $\vec{S}_{11}$ and $\vec{S}_{21}$ are the measured TEM mode reflection coefficients obtained by a network analyzer.

The fixture's electromagnetic behavior depends on whether the two flanges are connected by conducting or nonconducting clamps or pins. If the two halves are electrically insulated, then a radial waveguide TEM mode (E_z, H_ϕ) is present. If, on the other hand, the halves are shorted, then this mode should be suppressed.

10.2 Short-Circuited Open-ended Probes

10.2.1 Overview of Short-Circuited Probes

Another method that has been used over the years is a variation of the coaxial probe, where the sample is positioned at the end of the inner conductor as shown in Figure 40(a) [97, 108, 109]. A full-mode model of configuration in Figure 40(b) has been published [110]. Since the sample rests on a metal surface, the method has limited loss resolution. The method has the advantage that the sample has a strong electric field in the z direction at the end of the inner conductor. The sample at the conductor end is in a small radial waveguide with a TEM mode that has E_z and H_ϕ components. At the end of the coax the TEM mode can propagate between the sample and short for $[0 \leq \rho \leq a]$ and can resonant for high frequencies ($f \approx c/2a\sqrt{\epsilon_r'}$). Whereas for $[a \leq \rho \leq b]$ there are only cutoff TM$_{0m}$ modes.
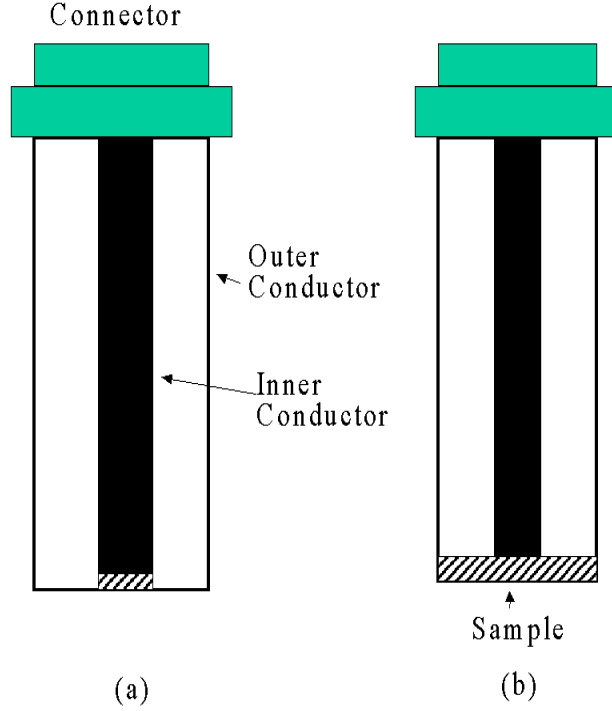
Figure 40. Open-ended sample method. (a) depicts the sample only under the inner post alone, and (b) the sample extends across the entire diameter of the coaxial line.

10.2.2 Mode-Match Derivation for the Reflection Coefficient for the Short-Circuited Probe

The full mode-match solution for the reflection coefficient for case (b), where the sample fills the coaxial line at the short position, can be derived by matching the tangential electric and magnetic fields at the coaxial-line-sample interface, and by requiring the tangential electric field goes to zero on the short-circuit termination. The radial eigenfunctions in coaxial line of inner radius a and outer radius b are

$$
\begin{aligned}
R_{1n}(\rho) = \quad & \underbrace{c_0/\rho}_{\text{for } n=0 \ (\text{TEM mode})} \\
= \quad & \underbrace{c_n[J_1(k_{1n}\rho)N_0(k_{1n}a) - N_1(k_{1n}\rho)J_0(k_{1n}a)]}_{n>0 \ (TM_{0n}\text{modes})}
\end{aligned}
\tag{161}
$$

where J_0, J_1, N_0, N_1 are the Bessel functions of the second kind. Also,

$$c_n = \frac{\pi k_{1n}}{\sqrt{2}} \frac{1}{\sqrt{\frac{J_0^2(k_{1n}a)}{J_0^2(k_{1n}b)} - 1}}, \tag{162}$$

where the eigenvalues in the coaxial line are found from the condition that the z-electric field component vanishes on the side wall. This condition requires for $n = 0$, $k_{10} = 0$. For $n \neq 0$ we have TM_{0m} modes with eigenvalues determined from

$$J_0(k_{1n}b)N_0(k_{1n}a) - N_0(k_{1n}b)J_0(k_{1n}a) = 0. \tag{163}$$

The propagation coefficients are

$$\gamma_{1n} = j\sqrt{\epsilon_{r1}^*\mu_{r1}^*\frac{\omega^2}{c_{lab}^2} - k_{1n}^2}. \tag{164}$$

The reflection coefficient of all modes, TEM plus evanescent, is

$$\vec{\Gamma} = [\overleftrightarrow{I} - \overleftrightarrow{L_4}\overleftrightarrow{L_3}]^{-1} \cdot [\overleftrightarrow{L_4}\,\vec{Q} + \vec{P}]. \tag{165}$$

The measured TEM reflection coefficient is Γ_0. Given Γ_0, the first component in eq. (165) is solved by a nonlinear root finding algorithm for the permittivity. The unknown permittivity is ϵ_2 and has thickness L and radius b. The inner conductor of the coaxial line has radius a. The coefficients are given by

$$\overleftrightarrow{L_{4mn}} = -\frac{\gamma_{1m}}{j\omega\epsilon_1}\cosh k_{2n}L\int_a^b rJ_1(\lambda_{2n}r)R_{1m}(\rho)dr \tag{166}$$

and

$$\vec{P} = \delta_{mn}. \tag{167}$$

The matrix elements are given by:

$$\int_a^b rR_{10}J_1(\lambda_{2n}r)dr = \frac{1}{\sqrt{\ln(b/a)}}\int_a^b J_1(\lambda_{2n}r)dr = \frac{1}{\sqrt{\ln(b/a)}}\frac{J_0(\lambda_{2n}a)}{\lambda_{2n}}, \tag{168}$$

$$\int_a^b rR_{1m}J_1(\lambda_{2n}r)dr = \frac{2}{\pi}\frac{c_m}{k_{1m}}\frac{1}{J_0(k_{1m}b)}\frac{\lambda_{2n}}{k_{1m}^2 - \lambda_{2n}^2}[J_0(\lambda_{2n}b)J_0(k_{1m}a) - J_0(\lambda_{2n}a)J_0(k_{1m}b)], \tag{169}$$

88

$$\overset{\leftrightarrow}{L}_{3nm} = \frac{j\omega\epsilon_2 \int_a^b r R_{1m} J_1(\lambda_{2n}r)dr}{k_{2n}\sinh(k_{2n}L)N_n^2}, \tag{170}$$

$$\mathbf{Q}_n = \frac{j\omega\epsilon_2 \int_a^b r R_{10} J_1(\lambda_{2n}r)dr}{k_{2n}\sinh(k_{2n}L)N_n^2}, \tag{171}$$

$$N_n^2 = \int_0^b r J_1^2(\lambda_{2n}r)dr = \frac{b^2 J_1^2(\lambda_{2n}b)}{2}, \tag{172}$$

where $k_{2n} = \sqrt{k_2^2 - \lambda_{2n}^2}$. $k_2 = \omega\sqrt{\epsilon_2\mu_2}$. The eigenvalues λ_{2n} are roots of

$$J_0(\lambda_{2n}b) = 0. \tag{173}$$

11. Measurement Methods for Liquids

There are both resonant and nonresonant methods for liquids. Resonant methods use either cavities or dielectric resonators. Transmission-line methods include open-circuited or matched-load waveguides. A good database for liquid dielectric measurements is given in Reference [111].

11.1 Liquid Measurements Using Resonant Methods

A resonance can be supported in a low-loss dielectric cylinder within a metallic shield. It will also resonant if a hole is drilled into the center and liquid is inserted as shown in Figure 41 [112, 113]. The dielectric loss of the specimen influences the resonant frequency and Q. The electric field is proportional to the Bessel function $J_1(\lambda r)$, which goes to 0 as $r \to 0$. Hence, by placing the liquid at the center of the dielectric resonator, the loss of the specimen will not damp out the Q, and a resonant mode can propagate.

11.2 Open-Circuited Holders

11.2.1 Overview

The shielded open-circuited coaxial line specimen holder has been used for years for dielectric measurements of liquids and powders in the microwave band [4, 114–117]. The fixture is composed of an outer conductor that extends beyond the end of the inner conductor, as shown in Figure 42. The specimen holder algorithm is based on an accurate model of a
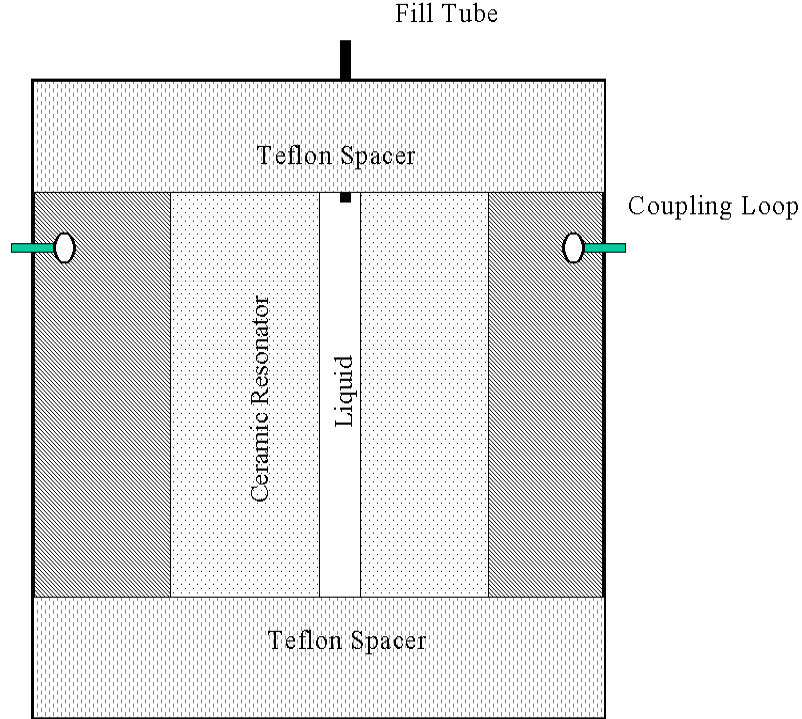
Figure 41. A dielectric resonator for liquids.

coaxial line terminated in a shielded open circuit. The advantage of an open-circuited holder is the ease of specimen installation, the broad frequency capability, and the strong electric field in the specimen region. The specimen holder has been found useful in both ambient and high-temperature measurements. Von Hippel [118] used an open-circuited specimen holder for liquid measurements. Bussey [114] extended the open-circuited holder technique to higher frequencies using an admittance model. Scott and Smith [119] studied the instabilities encountered in solving the relevant nonlinear open-circuit equations. Hill [120] studied in situ measurements of soils using open-circuited transmission lines. Jesch [121] used the shielded open-circuited holder for measurements on shale oil. Biological tissues have been measured using the shielded open-circuited line, for example, see Stuchly and Stuchly [97]. The model we use is based on a full-wave solution. The full-mode model is more accurate than the commonly used capacitance expansion [114, 122]. Here, we will develop the theory behind the shielded open-circuited holder, and present measurement results and uncertainties.

There are various limitations of the measurement method. For low-permittivity materials
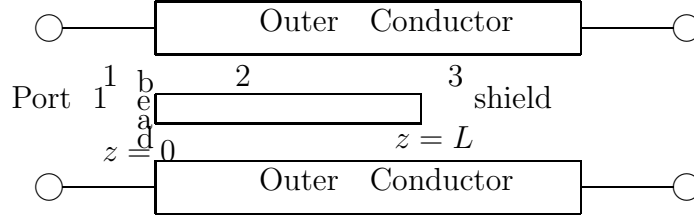
Figure 42. A shielded open circuit termination. The inner and outer radii of conductors are a and b.
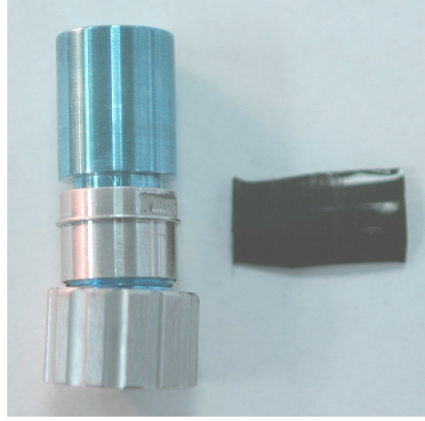
Figure 43. Open-circuited holder for liquids.

$(\epsilon'_r < 10)$ 14 mm coaxial line can be used up to approximately 1 GHz; 7 mm coaxial line can be used up to approximately 10 GHz. For a given coaxial line there are cutoff conditions where the high-order TM_{0m} modes start to propagate. In addition, due to the bead properties, the TE_{11} mode propagate. Any deviation of the inner conductor from the vertical will cause an asymmetry that may couple in to other higher modes. In theory, if the shield is infinitely long and filled with specimen, the higher-order mode models can be used at frequencies above cutoff of the shield section. However, the method, in practice, is limited to frequencies where the higher modes are cut off in the specimen. Sufficiently lossy samples attenuate the fields so that the measurement sees only a semi-infinite line. Less lossy samples will have

multiple reflections in the line. We can modify the algorithms so that the liquid is only in the coaxial region. This enhances the measurement frequency range.

11.2.2 Model 1: TEM Model with Correction to Inner Conductor Length

Bussey derived a simple and useful model for the shielded open-circuited holder with a frequency-dependent correction to the length of the inner conductor [114, 116]. For the special case of a compensated bead where the connector air section length is L_1, bead section length is L_2, and the inner conductor length is L_3, we have

$$\Gamma = \exp\left(-2(\gamma_1 L_1 + \gamma_2 L_2)\right)\frac{\beta_2 - \tanh(\gamma_3 L_3)}{\beta_2 + \tanh(\gamma_3 L_3)}, \tag{174}$$

where

$$\beta_2 = \sqrt{\frac{\mu_{r(3)}^*}{\epsilon_{r(3)}^*}}. \tag{175}$$

The propagation constants of the line sections and bead sections are

$$\gamma_i = j\frac{\omega}{c_{vac}}\sqrt{\epsilon_{r(i)}^*\mu_{r(i)}^*}. \tag{176}$$

Due to the open-circuit termination the inner conductor has an effective length longer than the measured L_3. In this TEM model, the higher modes at the discontinuity are modeled as a correction in length L_3 due to the fringing capacitance at the end of the inner conductor. Somlo [122] derived an approximate expression for a correction to the inner conductor length ΔL, that accounts for the fringing capacitance:

$$\Delta L = (b - a)(0.6034 + 0.9464x^2 + 18.19x^{5.127}), \tag{177}$$

where $x = b\sqrt{\epsilon_{r(3)}'}/\lambda$, λ is the free-space wavelength, and b and a are the radii of the outer and inner conductors. ΔL is an increasing function of frequency. Equation (177) is valid for $x < 0.3$. We assume that the frequency of operation is chosen such that the TM_{01} mode is below cut-off in the cylindrical waveguide section. This requires $x < 0.383$ or $f_{(GHz)} < 0.115/b\sqrt{\epsilon_{r(3)}'}$ [114]. The total length of the holder is $L = L_1 + L_2 + L_3 + \Delta L$. The effective bead thickness L_2 near the connector needs to be determined to minimize uncertainty.

11.2.3 Model 2: Full-Mode Model Theoretical Formulation

Consider a sample in the transmission line shown in Figure 43. The shielded open-circuited holder consists of three sections. Region 1 contains the bead in the airline, which is at 50 Ω, Region 2 contains the sample, and Region 3 represents the shield region. The problem is to accurately characterize the shielded open circuit. We will develop a compact expression for the reflection coefficient in terms of the air line and the sample parameters.

We assume a time dependence of $\exp(j\omega t)$ in the coaxial line. Due to azimuthal symmetry, we need to consider only TEM and TM_{0mn} modes. We also assume that an incident TEM wave travels from the input port towards the sample. At the sample discontinuity the TM_{0mn} modes are reflected, and a TEM wave travels into the material. The problem is to obtain an expression for the TEM reflection coefficient as a function of the specimen's complex permittivity.

The radial component of the electric fields in Regions 1 through 3 are

$$E_{\rho(1)} = R_0(\rho)\exp\left(-\gamma_{10}z\right) + \sum_{n=0}^{\infty}\Gamma_n R_n(\rho)\exp(\gamma_{1n}z), \tag{178}$$

$$E_{\rho(2)} = \sum_{n=0}^{\infty} A_n R_n(\rho)\exp\left(-\gamma_{2n}z\right) + \sum_{n=0}^{\infty} B_n R_n(\rho)\exp(\gamma_{2n}z), \tag{179}$$

$$E_{\rho(3)} = \sum_{n=1}^{\infty} Q_n G_n(\rho)\exp\left(-\gamma_{3n}z\right), \tag{180}$$

where for $n = 0$,

$$\gamma_{i0} = j\frac{\omega\sqrt{\epsilon_{ri}}}{c_{vac}}, \tag{181}$$

and for $i = 1, 2$, if $n > 0$,

$$\gamma_{in} = j\sqrt{\epsilon_{ri}\mu_{ri}\frac{\omega^2}{c_{lab}^2} - k_{in}^2}, \tag{182}$$

for $i = 1, 2$ and for all of the modes in Region 3. If the argument is negative, then the wave is evanescent and

$$\gamma_{in} = \sqrt{k_{in}^2 - \epsilon_{ri}\mu_{ri}\frac{\omega^2}{c_{lab}^2}}. \tag{183}$$

The radial eigenfunctions in Regions 1 and 2 for the TEM mode and evanescent TM_{0m} modes are, for $m = 1, 2, \cdots$.

$$R_{m(i)} = C_{m(1)}[J_1(k_{m(1)}\rho)Y_0(k_{m(1)}a) - Y_1(k_{m(1)}\rho)J_0(k_{m(1)}a)], \tag{184}$$

and $R_{0(1)} = C_{0(1)}/\rho$. In eq. (184), $R_{m(1)}$ are radial eigenfunctions, c_{vac} is the speed of light in vacuum and

$$C_0 = \frac{1}{\sqrt{\ln(b/a)}}, \tag{185}$$

and

$$C_n = \sqrt{\frac{1}{\int_a^b \rho R_n^2(\rho)d\rho}} = \frac{\pi k_{1n}}{\sqrt{2}} \frac{1}{\sqrt{\frac{J_0^2(k_{1n}a)}{J_0^2(k_{1n}b)} - 1}}. \tag{186}$$

The eigenvalues are determined from

$$J_0(k_{m(1)}a)Y_0(k_{m(1)}b) - Y_0(k_{m(1)}a)J_0(k_{m(1)}b) = 0. \tag{187}$$

G_n are normalized eigenfunctions in the cylindrical waveguide and R_n are the normalized eigenfunctions in the coaxial line defined by

$$G_n(\rho) = S_n J_1(k_{3n}\rho), \tag{188}$$

where S_m are normalization constants are given by

$$S_{n(3)} = \frac{1}{\sqrt{\int_0^{b_3} \rho J_1^2(\lambda_{3(n)}\rho)d\rho}} = \frac{\sqrt{2}}{b_3 J_1(\lambda_{3(n)}b_3)}. \tag{189}$$

The eigenvalues are found when the tangential electric field on the side wall vanishes

$$J_0(k_{3n}b) = 0. \tag{190}$$

Therefore $k_{3n} = p_n/b$, where p_n is the nth root of $J_0(x) = 0$, for $n = 0, 1, 2...$.

The azimuthal magnetic fields in Regions 1 through 3 are

$$H_{\phi(1)} = \frac{j\omega\epsilon_1}{\gamma_{10}}R_0(\rho)\exp(-\gamma_{10}z) - \sum_{n=0}^{\infty}\Gamma_n\frac{j\omega\epsilon_1}{\gamma_{1n}}R_n(\rho)\exp(\gamma_{1n}z), \tag{191}$$

$$H_{\phi(2)} = \sum_{n=0}^{\infty}\frac{j\omega\epsilon_2}{\gamma_{2n}}A_n R_n(\rho)\exp(-\gamma_{2n}z) - \sum_{n=0}^{\infty}\frac{j\omega\epsilon_2}{\gamma_{2n}}B_n R_n(\rho)\exp(\gamma_{2n}z), \tag{192}$$

$$H_{\phi(3)} = \sum_{n=0}^{\infty}\frac{j\omega\epsilon_3}{\gamma_{3n}}Q_n G_n(\rho)\exp(-\gamma_{3n}z). \tag{193}$$

The tangential components of E_ρ and H_ϕ must be continuous across the interfaces. If we match the tangential components of the electric field from eqs. (178) and (179) at $z = 0$ we obtain the following equations:

$$A_m + B_m = \delta_{m0} + \Gamma_m, \tag{194}$$

where $m = 0, 1, 2 \cdots$. If we match the magnetic field in eqs. (179) and (180) and the tangential electric fields at $z = L$, we obtain

$$Q_m = \exp\left(\gamma_{3m}L\right) \sum_{n=0}^{\infty} [A_n \exp\left(-\gamma_{2n}L\right) + B_n \exp\left(\gamma_{2n}L\right)] < G_m R_n >, \tag{195}$$

or

$$\vec{Q} = \mathbf{M_1}\vec{A} + \mathbf{M_2}\vec{B}, \tag{196}$$

where

$$M_{(1)mn} = \exp\left(\gamma_{3m}L\right) \exp\left(-\gamma_{2n}L\right) < G_m R_n >, \tag{197}$$

$$M_{(2)mn} = \exp\left(\gamma_{3m}L\right) \exp\left(\gamma_{2n}L\right) < G_m R_n > . \tag{198}$$

If we match eqs. (191) and (192) at $z = 0$ we obtain

$$A_m - B_m = \frac{\epsilon_1 \gamma_{2m}}{\epsilon_2 \gamma_{1m}} \left[\delta_{m0} - \Gamma_m\right], \tag{199}$$

where $m = 0, 1, 2$. If we match eqs. (192) and (193) at $z = L$ we find

$$\frac{\gamma_{2n}}{\epsilon_2} \sum_{m=0}^{\infty} \exp\left(-\gamma_{3m}L\right) \frac{\epsilon_3}{\gamma_{3m}} Q_m < G_m R_n >= A_n \exp\left(-\gamma_{2n}L\right) - B_n \exp\left(\gamma_{2n}L\right), \tag{200}$$

or

$$\mathbf{M_3}\vec{Q} = \mathbf{M_4}\vec{A} - \mathbf{M_5}\vec{B}, \tag{201}$$

where

$$M_{(3)mn} = \exp\left(-\gamma_{3m}L\right) < G_m R_n > \frac{\gamma_{2n}\epsilon_{r3}}{\gamma_{3m}\epsilon_{r2}}. \tag{202}$$

We can solve for the coefficients in eqs. (194) and (199) using

$$A_n = \frac{1}{2}\left[\delta_{n0}(1 + \frac{\epsilon_{r1}\gamma_{2n}}{\epsilon_{r2}\gamma_{1n}}) + \Gamma_n(1 - \frac{\epsilon_{r1}\gamma_{2n}}{\epsilon_{r2}\gamma_{1n}})\right] \tag{203}$$

95

and

$$B_n = \frac{1}{2}\left[\delta_{n0}(1 - \frac{\epsilon_{r1}\gamma_{2n}}{\epsilon_{r2}\gamma_{1n}}) + \Gamma_n(1 + \frac{\epsilon_{r1}\gamma_{2n}}{\epsilon_{r2}\gamma_{1n}})\right].\tag{204}$$

Let

$$\vec{A} = \vec{C} + \mathbf{M_6}\vec{\Gamma}\tag{205}$$

and

$$\vec{B} = \vec{D} + \mathbf{M_7}\vec{\Gamma},\tag{206}$$

where

$$\mathbf{M}_{(6)mn} = \frac{1}{2}\left(1 - \frac{\epsilon_{r1}\gamma_{2n}}{\epsilon_{r2}\gamma_{1n}}\right)\delta_{mn},\tag{207}$$

$$\mathbf{M}_{(7)mn} = \frac{1}{2}\left(1 + \frac{\epsilon_{r1}\gamma_{2n}}{\epsilon_{r2}\gamma_{1n}}\right)\delta_{mn},\tag{208}$$

$$C_n = \frac{1}{2}\left[\delta_{n0}(1 + \frac{\epsilon_{r1}\gamma_{2n}}{\epsilon_{r2}\gamma_{1n}})\right],\tag{209}$$

$$D_n = \frac{1}{2}\left[\delta_{n0}(1 - \frac{\epsilon_{r1}\gamma_{2n}}{\epsilon_{r2}\gamma_{1n}})\right].\tag{210}$$

We obtain the following equation for $\vec{\Gamma}$:

$$[\mathbf{M_8}\mathbf{M_6} + \mathbf{M_9}\mathbf{M_7}]\vec{\Gamma} + \mathbf{M_8}\vec{C} + \mathbf{M_9}\vec{D} = 0,\tag{211}$$

where

$$\mathbf{M_8} = \mathbf{M_3}\mathbf{M_1} - \mathbf{M_4},\tag{212}$$

$$\mathbf{M_9} = \mathbf{M_3}\mathbf{M_2} + \mathbf{M_5}.\tag{213}$$

Therefore,

$$\mathbf{P} \cdot \vec{\Gamma} = \vec{T}.\tag{214}$$

Applying measured results for the reflection coefficient of the TEM mode Γ_0, we use Cramer's rule in eq. (214) to get a nonlinear equation for ϵ_{2r}^* of the form $\Gamma_0 = f(\epsilon_{2r}^*)$.

In the measurements, the reference plane must be transformed through the bead and air sections. The transformed reflection coefficient to be used for the TEM mode in eq. (214) is

$$\Gamma_{\text{trans}} = \Gamma_0 \exp\left(-2(\gamma_a L_1 + \gamma_b L_2)\right),\tag{215}$$
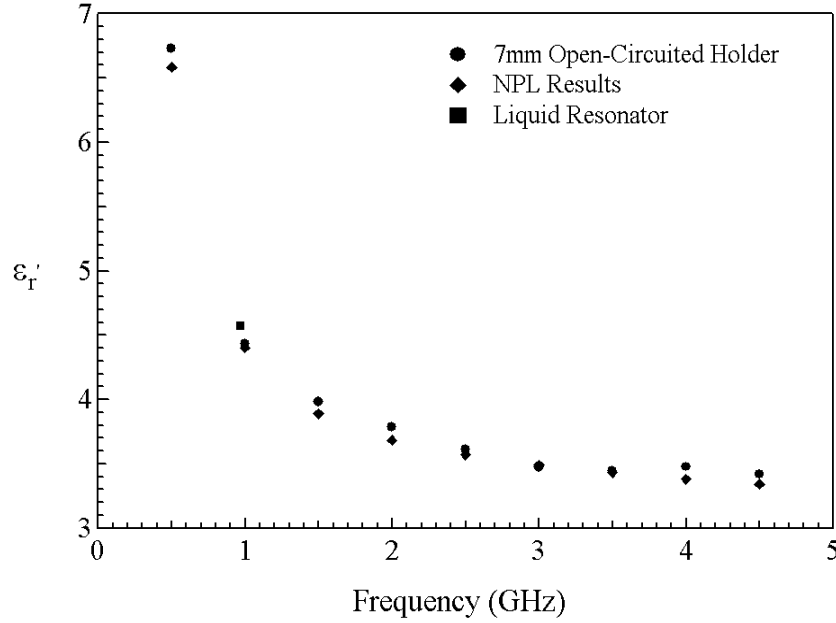
Figure 44. The real part of the permittivity for 1-butanol.

where L_1 and L_2 are the effective axial lengths of the air and bead sections of the connector. The bead is usually nonuniform, so an effective length needs to be determined from a standard measurement. A way to eliminate the bead rotation problem is to measure the sample holder in air and divide that result into the result for the measurement with the sample in the holder.

The TEM mode admittance and reflection coefficient are related by

$$\Gamma_0 = \frac{Y_0 - Y}{Y_0 + Y},\tag{216}$$

where Y_0 is the admittance of the air-filled line and Y is the admittance with the sample in the line.

In Figures 44 and 45, permittivity and loss tangent data for butanol are plotted for measurements with an open-circuited holder and the TE_{01} resonator.

11.2.4 Uncertainty Analysis for Shielded Open-Circuited Holder

Uncertainties include the reflection coefficient, conductor and bead dimensions. Since this specimen holder is usually used for measurements of liquids, gaps between conductors and specimens are neglected. These independent uncertainty sources are tabulated in Table 11.

97

Figure 45. The loss tangent for 1-butanol.

Table 11. Uncertainties for shielded open-circuited holder

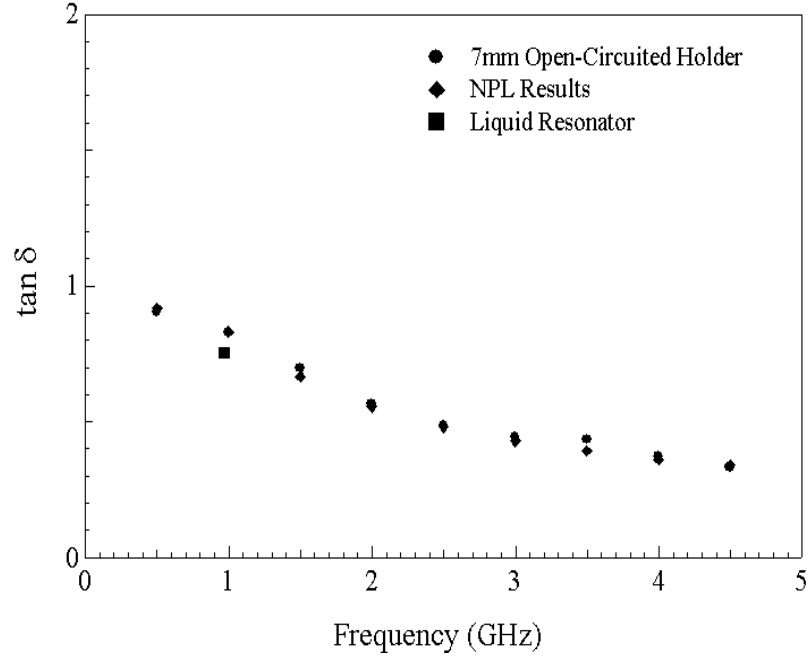| Error Source	Magnitude
Inner conductor length	± 0.0002 m
Outer conductor diameter	± 0.0002 m
Inner conductor diameter	± 0.0002 m
Bead thickness	± 0.0004 m
Max($|\Gamma|$)	± 0.01
Max($|\theta|$)	$\pm 0.1^o$

In order to evaluate the uncertainty introduced by the measured scattering and length parameters, we assume that a differential uncertainty analysis can be used. We assume that the total RSS relative uncertainty with no cross-correlation can be written as

$$\frac{\Delta\epsilon'_{r2}}{\epsilon'_{r2}} = \frac{1}{\epsilon'_{r2}}\sqrt{\left(\frac{\partial\epsilon'_{r2}}{\partial|\Gamma|}\Delta|\Gamma|\right)^2 + \left(\frac{\partial\epsilon'_{r2}}{\partial\theta_{11}}\Delta\theta_{11}\right)^2 + \left(\frac{\partial\epsilon'_{r2}}{\partial L}\Delta L\right)^2 + \left(\frac{\partial\epsilon'_{r2}}{\partial L_3}\Delta L_3\right)^2}, \qquad (217)$$

$$\frac{\Delta\epsilon''_{r2}}{\epsilon''_{r2}} = \frac{1}{\epsilon''_{r2}}\sqrt{\left(\frac{\partial\epsilon''_{R2}}{\partial|\Gamma|}\Delta|\Gamma|\right)^2 + \left(\frac{\partial\epsilon''_{r2}}{\partial\theta_{11}}\Delta\theta_{11}\right)^2 + \left(\frac{\partial\epsilon''_{r2}}{\partial L}\Delta L\right)^2 + \left(\frac{\partial\epsilon''_{r2}}{\partial L_3}\Delta L_3\right)^2}, \qquad (218)$$

where $\Delta\theta_{11}$ is the uncertainty in the phase of the reflection coefficient, $\Delta|\Gamma|$ is the uncertainty in the magnitude of the reflection coefficient, and ΔL, ΔL_3 are the uncertainties the in lengths of the inner conductor and bead. The bead holds the center conductor in place and is usually made of polytetrafluoroethylene.

The independent variables are the dimension of the conductors, the thickness of bead, and the phase and magnitude of scattering parameters. The uncertainties used for the scattering parameters depend on the specific ANA used for the measurements. If σ_s is the standard deviation in N measurements of the independent variable r, then the standard error is $\Delta r = \sigma_s/\sqrt{N}$. The partial derivatives in eqs. (217) and (218) and complete uncertainty analysis is given in Baker-Jarvis et al. [116].

11.3 Open-ended Coaxial Probe

11.3.1 Theory of the Open-ended Probe

Over the years, the open-ended coaxial probe has been studied extensively from both theoretical and experimental aspects. Open-ended coaxial probes are commonly used as nondestructive testing tools and for liquid measurements over a frequency band of 200 MHz to 20 GHz. The method, although nondestructive, does have limitations. For example, the fields at the probe end contain both E_z and E_ρ components. If there is an air gap between the specimen and the probe, the discontinuity in the normal electric field causes a large
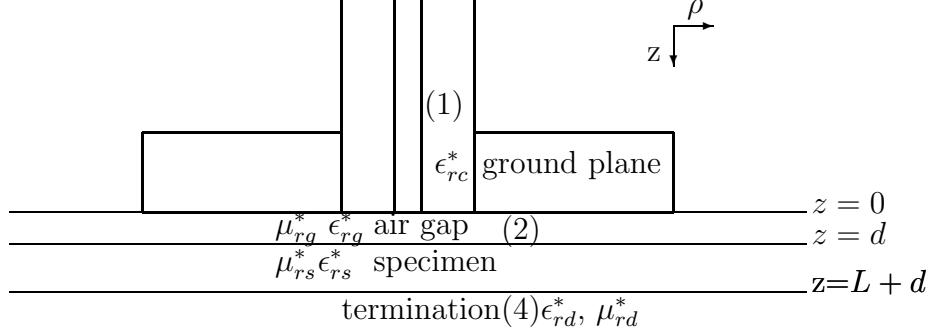
Figure 46. The open-ended coaxial probe over a specimen with an air gap between specimen and probe. In liquid measurements there is usually no gap.

error in the predicted permittivity. For this reason, the probe has been used primarily for liquid and semisolid measurements, where good contact can be obtained. Equations for the reflection coefficient can be obtained from solutions to the Helmholtz equation [98–100]. In liquid measurements, the coaxial probe is submersed in the specimen and the reflection coefficient is measured. The permittivity is then obtained using a Newton-Raphson root finding technique. The size of the probe is related to the frequency band of interest. A typical probe with liftoff capability is shown in Figure 47. The higher the frequency, the smaller the coaxial probe size. We use a full-mode model of the coaxial probe. In matrix form we can write the reflection coefficient vector as

$$\mathbf{Q} \cdot \vec{\Gamma} = \vec{P}, \tag{219}$$

or

$$\sum_{n=0}^{\infty} Q_{mn} \Gamma_n = P_m, \tag{220}$$

where

$$Q_{mn} = \int_0^\infty \zeta D_m \frac{\epsilon^*_{rg} D_n (e^{2\gamma_2 d}((1 + \frac{\epsilon^*_{rg}\gamma_3}{\epsilon^*_{rs}\gamma_2}) + \Theta(1 - \frac{\epsilon^*_{rg}\gamma_3}{\epsilon^*_{rs}\gamma_2})) + ((1 - \frac{\epsilon^*_{rg}\gamma_3}{\epsilon^*_{rs}\gamma_2}) + \Theta(1 + \frac{\epsilon^*_{rg}\gamma_3}{\epsilon^*_{rs}\gamma_2})))}{\epsilon^*_{rc}\gamma_2 (e^{2\gamma_2 d}((1 + \frac{\epsilon^*_{rg}\gamma_3}{\epsilon^*_{rs}\gamma_2}) + \Theta(1 - \frac{\epsilon^*_{rg}\gamma_3}{\epsilon^*_{rs}\gamma_2})) + ((\frac{\epsilon^*_{rg}\gamma_3}{\epsilon^*_{rs}\gamma_2} - 1) - \Theta(1 + \frac{\epsilon^*_{rg}\gamma_3}{\epsilon^*_{rs}\gamma_2})))} d\zeta$$

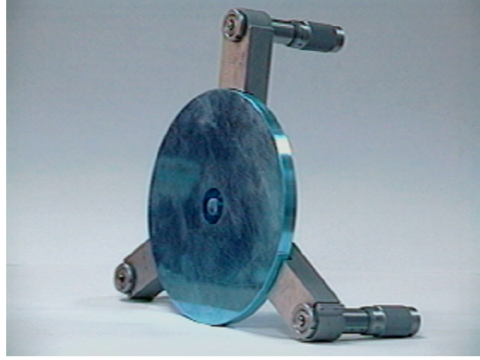$$+ \frac{1}{\gamma_{n(c)}} \delta_{mn}, \tag{221}$$

100

Figure 47. Dielectric coaxial probe for liquids.

$$P_m = -\int_0^\infty \zeta D_m \frac{\epsilon^*_{rg} D_0 (e^{2\gamma_2 d}((1 + \frac{\epsilon^*_{rg}\gamma_3}{\epsilon^*_{rs}\gamma_2}) + \Theta(1 - \frac{\epsilon^*_{rg}\gamma_3}{\epsilon^*_{rs}\gamma_2})) + ((1 - \frac{\epsilon^*_{rg}\gamma_3}{\epsilon^*_{rs}\gamma_2}) + \Theta(1 + \frac{\epsilon^*_{rg}\gamma_3}{\epsilon^*_{rs}\gamma_2})))}{\epsilon^*_{rc}\gamma_2 (e^{2\gamma_2 d}((1 + \frac{\epsilon^*_{rg}\gamma_3}{\epsilon^*_{rs}\gamma_2}) + \Theta(1 - \frac{\epsilon^*_{rg}\gamma_3}{\epsilon^*_{rs}\gamma_2})) + ((\frac{\epsilon^*_{rg}\gamma_3}{\epsilon^*_{rs}\gamma_2} - 1) - \Theta(1 + \frac{\epsilon^*_{rg}\gamma_3}{\epsilon^*_{rs}\gamma_2})))} d\zeta$$
$$+ \frac{1}{\gamma_1}\delta_{m0}, \ (222)$$

for $m, n = 0, 1, 2, ...N$, where N is number of modes. We define propagation coefficients $\gamma_i = j\sqrt{k_i^2 - \zeta^2}$, for $\Re(k_i) > \zeta$, $i = 2, 3, 4$, and $\gamma_i = \sqrt{\zeta^2 - k_i^2}$ if $\Re(k_i) < \zeta$. For a shorted termination at $z = d + L$, $\Theta = \exp(-2\gamma_3 L)$. For a material termination at this position we define $\Theta = \exp(-2\gamma_3 L)(1 - \Theta_2)/(1 + \Theta_2)$, where $\Theta_2 = (\epsilon^*_{rs}\gamma_4)/(\epsilon^*_{rd}\gamma_3)$. In the limit of semi-infinite material, $L \to \infty$, and since $\epsilon''_{rs} > 0$ we obtain $\Theta \to 0$. The reflection coefficient of the TEM mode is of primary interest since the other modes are evanescent in the coaxial line. The permittivity is calculated using a Newton-Raphson procedure on Γ_0. An uncertainty analysis is given in reference [1].

11.3.2 Uncertainty Analysis for Coaxial Open-ended Probe

Uncertainties in open-ended coaxial measurements include calibration and measurement uncertainties [99]. We consider that the uncertainty in a measurement due to phase, magnitude and lift-off. These independent sources of error are tabulated in Table 12. We consider that calculated permittivity is a function of the following independent variables: $\epsilon^*_{rs}(|\Gamma_0|, \theta_0, d)$. The estimated magnitude and phase uncertainties introduced by the measurement standards are combined with the network analyzer uncertainties. A worst-case differential uncertainty

Table 12. Sources of error for the open-ended coaxial holder

Error Source	Magnitude
Outer conductor diameter	± 0.0002 m
Inner conductor diameter	± 0.0002 m
Permittivity of bead	± 0.02
Max($|\Gamma|$)	± 0.01
Max($|\theta|$)	$\pm 0.1^o$

analysis assuming no cross-correlations is

$$\Delta\epsilon'_{rs} = \sqrt{\left(\frac{\partial\epsilon'_{rs}}{\partial|\Gamma_0|}\Delta|\Gamma_0|\right)^2 + \left(\frac{\partial\epsilon'_{rs}}{\partial\theta_0}\Delta\theta_0\right)^2 + \left(\frac{\partial\epsilon'_{rs}}{\partial d}\Delta d\right)^2}. \tag{223}$$

A similar equation can be written for ϵ''_{rs}. Implicit differentiation can be used to find the necessary derivatives. The details are given in Reference [99].

12. Dielectric Measurements on Biological Materials

12.1 Methods for Biological Measurements

The dielectric properties of human tissues have been studied extensively over the years. Therefore the range of conductivities that occur in the human body are well known. In the past, phantoms have been used for: (a) studies on the electromagnetic interaction with human tissue, (b) health effects of microwaves, and (c) interaction of wireless transmitters with human tissue [123]. The effects of electromagnetic waves on biological tissues is related to the conductivity and dielectric properties of tissues. The application of electric fields produces an overall increase in the molecular kinetic energy that is manifested in small amounts of heating, bond breaking, and production of free-radical, unpaired electron spins. Interactions of magnetic fields are less strong and are related primarily to paramagnetic effects and magnetic elements in the tissue.

The body consists of muscle, fat, bone, organs, and cavities. Since the dielectric properties of human tissues are heterogeneous, materials can be made that simulate the electrical response of a particular area of the human body. Most of the previously developed phantoms attempted to mimic both the conductivity and the permittivity of the human body.

Gabriel [124] has compiled extensive data on various human tissues and also developed a database. This database reports measurements on various human organs such as head, brain, muscle, fat, and bone.

12.2   Conductivity of High-Loss Materials Used as Phantoms

In this section we summarize the measurements on high-loss liquids that simulates the properties of biological tissues. For comparison purposes, typical ac conductivities and permittivities of the human body are shown in Figures 48 and 49. For the measurements on liquid conductivity, we used a dc conductivity probe. In Figure 50, the conductivity of KCl in 500 ml deionized water is plotted versus concentration for minor variations in temperature. The uncertainties in the liquid measurement are due to uncertainties in the measurement device and uncertainties in temperature variations. Our lab has a temperature stability on $\pm 1^o$C. We found for the conductivities: at $\sigma = 0.5$ the Type B expanded relative uncertainty $U = ku_c = 0.02$ (k-2).   The dependence of the conductivity on the KCl concentration is

Table 13. Previous work on human phantom materials.

Frequency	Materials	Citation and Date
1 Hz to 1 GHz	TEATFB	Broadhurst et al. 1987 [125]
900 MHz	graphite and resin	Kobayashi et al. 1993 [126]
10 to 100 MHz	glycine, NaCl	Hagmann et al. 1992 [127]
500 MHz to 3 GHz	silicone rubber, carbon black	Nikawa et al. 1996 [128]
200 MHz to 2.45 GHz	gel, aluminum powder, NaCl	Chou et al. 1984 [129]
750 MHz to 5 GHz	polyacrylamide, NaCl	Andreuccetti et al. 1988 [130]
5 to 40 MHz	agar, sodium azide, PVC powder	Kato et al. 1987 [131]
10 to 50 MHz	gelatine and NaCl	Marchal et al. 1989 [132]
300 MHz to 1 GHz	liquid	CENELEC Standard

nearly linear (see Figure 50).   Conductivities close to that of the human body components can be reproduced by either carbon-black composites, glycine composites, or various salty solutions. The liquids can be mixed easily to obtain the desired response. These liquids also show good time stability in the conductivity and a predictable temperature response. The
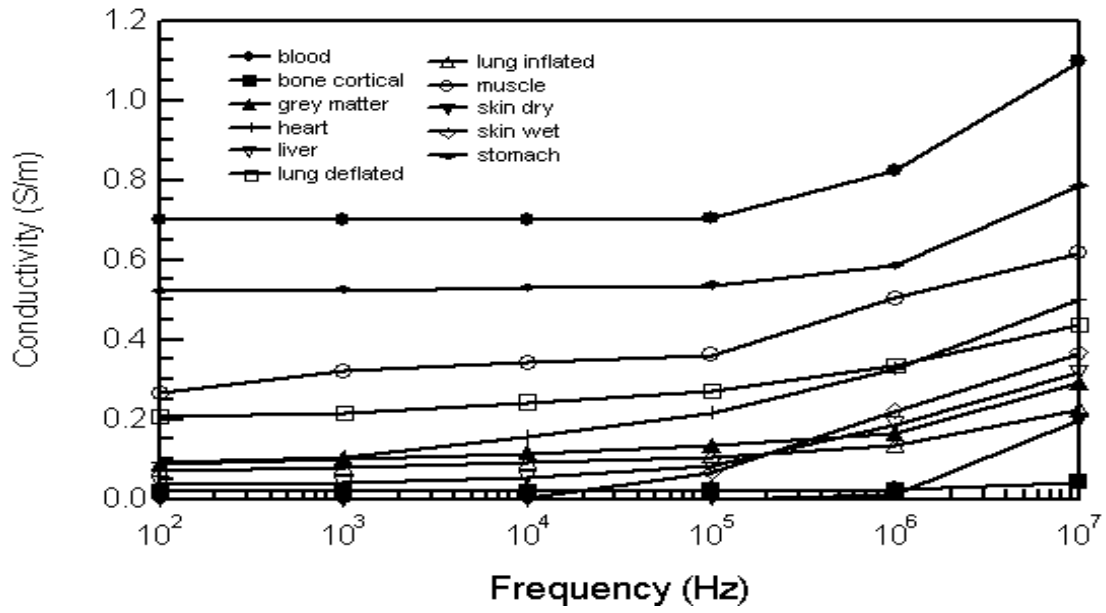
Figure 48. Conductivity measurements (S/m) on various body components [124] (no uncertainties assigned).
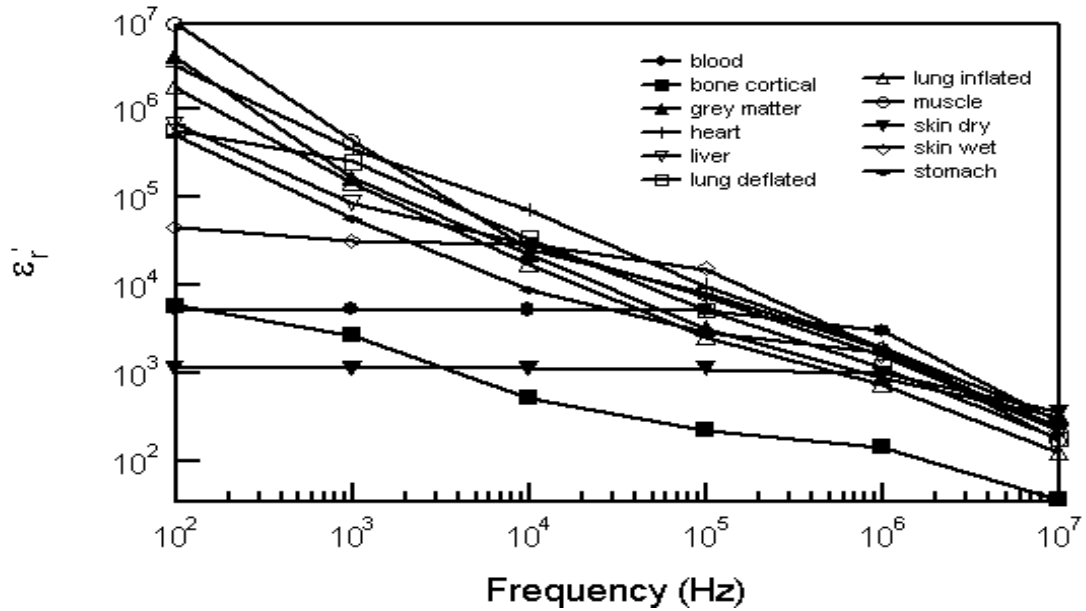

Figure 49. Permittivity measurements on various body components [124] (no uncertainties assigned).

104
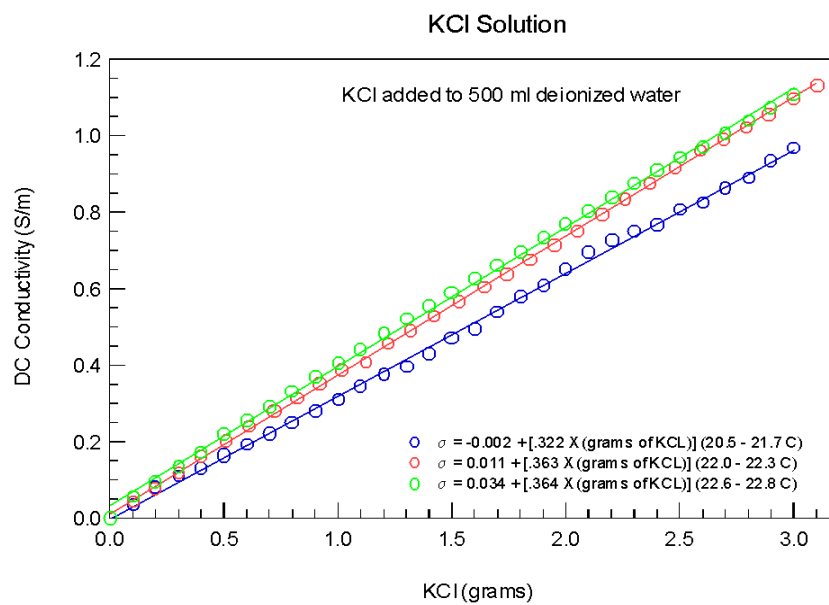
Figure 50. Conductivity of potassium chloride solution. Also shown are regression fits, in the straight lines, for the conductivity as a function of concentration.
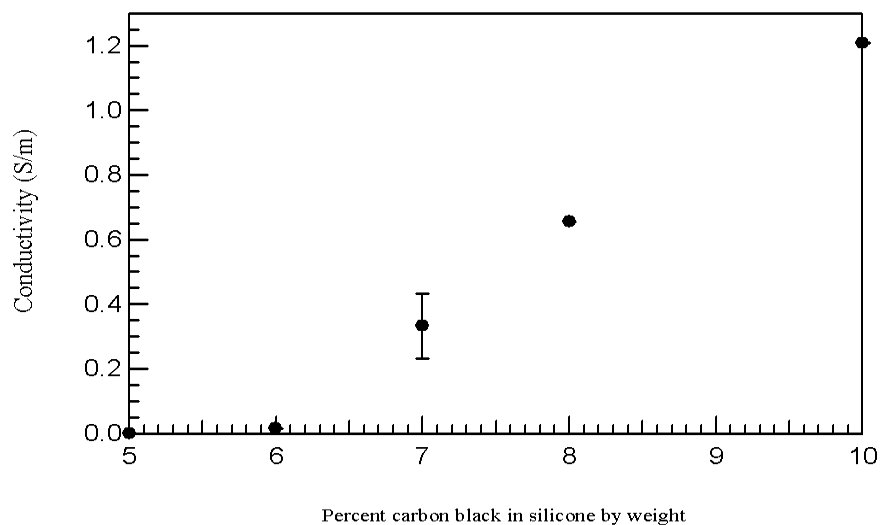
Figure 51. Conductivity as a function of carbon-black concentration for Cabot Black Pearls.
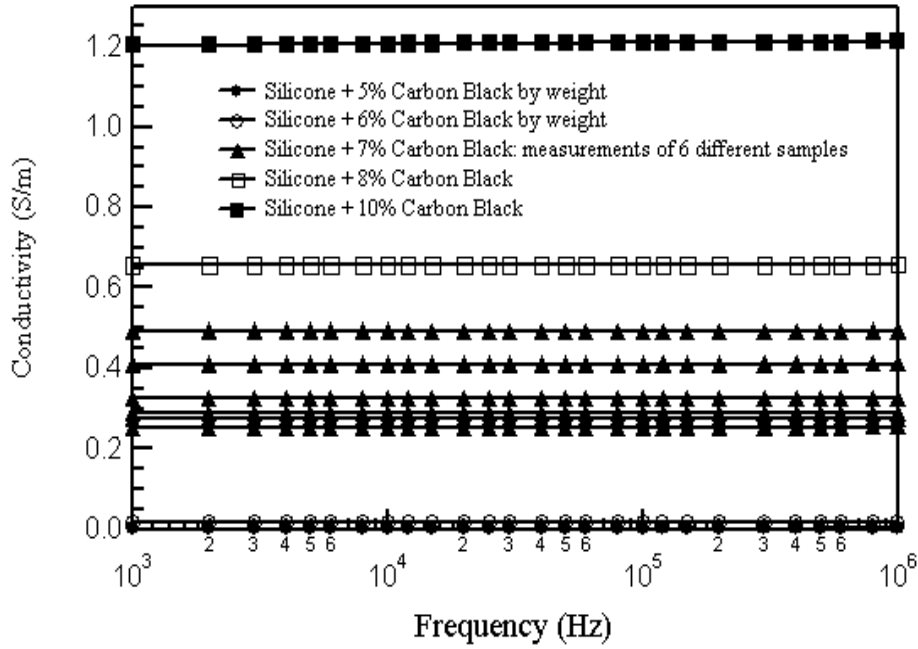
Figure 52. Conductivity as a function of carbon-black concentration for Cabot Black Pearls.

carbon-black conductivity exhibits a percolation threshold where the conductivity increases abruptly, as shown in Figures 51 and 52. There is a need to develop new phantom materials that are stable over time and exhibit the required electrical behavior over frequency bands of interest.

13.   Capacitive Techniques

13.1   Overview of Capacitive Techniques

Capacitance techniques (see Figures 53 and 54) are useful at frequencies extending from fractions of a hertz to megahertz frequencies. If the structures are deposited on chip so that they have very small conductors, specimens can be measured up to gigahertz frequencies [133,134]. Capacitance models work well if the wavelength is much longer than the conductor separation. Of course, most transmission lines such as coplanar waveguide, microstrip, stripline, and coaxial line can be used to make capacitive measurements.

A difficulty with capacitor measurements is the effects of the fringing-fields and, at low frequencies, electrode polarization. The fringe field is usually partially eliminated by using guards or making another measurement using a reference material or air. The fringing field

is minimized if the potentials of the guards and center electrode are at the same potential and only the feed potential is at an elevated potential.

The capacitance for a parallel plate with no fringing fields near the edges is given by

$$C = \frac{\epsilon' A}{d}. \tag{224}$$

The conductance at low frequency is given by

$$G = \omega \frac{\epsilon'' A}{d}. \tag{225}$$

This model assume no fringing fields. A more accurate model would include the effects of fringing fields. Use of guard electrodes as shown in Figure 53 minimizes the effects of the fringe field.

Capacitor Measurement
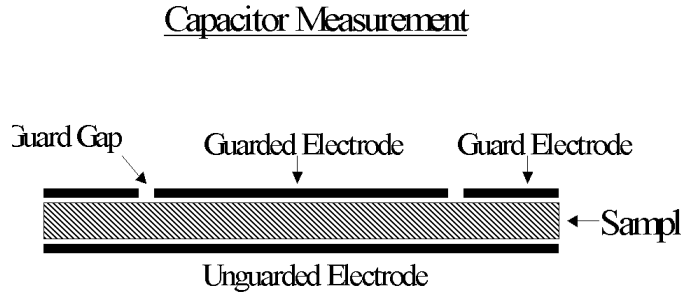
Figure 53. A specimen in a capacitor with electrode guards.

The permittivity can be obtained from measurements of C and G and is given by

$$\epsilon_r = \frac{C - jG/\omega}{C_{air} - jG_{air}/\omega}. \tag{226}$$

13.2   Capacitance Uncertainty

In a capacitor measurement, the components of the permittivity are given by

$$\epsilon_r' = C/C_{air}, \tag{227}$$

and

$$\epsilon_r'' = \frac{G}{\omega C_{air}}. \tag{228}$$

107

Table 14. Uncertainties for capacitive fixture

Error Source	Magnitude Uncertainty
Plate separation	± 0.0002 m
Area of plate	± 0.0002 m
Max (C/C_{air})	± 0.01
Max (G/C_{air})	± 0.01

The independent sources of uncertainty are tabulated in table 3. These include uncertainties in C/C_{air}, G/C_{air} and fringing field effects, parameterized by a variable F. The total relative uncertainty in the real part of permittivity is

$$\Delta \epsilon_r' = \sqrt{(\Delta C/C_{air})^2 + \left(\frac{\partial \epsilon_r'}{\partial (C/C_{air})} \frac{\partial (C/C_{air})}{\partial F} \Delta F\right)^2}, \tag{229}$$

and

$$\Delta \epsilon_r'' = \sqrt{(\Delta G/(\omega C_{air}))^2 + \left(\frac{\partial \epsilon_r''}{\partial (G/C_{air})} \frac{\partial (G/C_{air})}{\partial F} \Delta F\right)^2}. \tag{230}$$

13.3 Electrode Polarization and Permittivity Measurements

13.3.1 Overview

Measurements on conducting liquids are complicated by ionic conductivity and by the effects of electrode polarization [135]. Electrode polarization is caused by the build up and blockage of conducting ions on the capacitor plates, producing a capacitive double-layer electric field. The double layers on the electrodes produce a very large capacitance in series with the specimen under test. Since the electrode capacitance is not a property of the material under test, it must be removed from the measurement. The presence of electrode polarization results in the measured real part of the permittivity being many orders of magnitude greater than the correct value.

The effects of electrode polarization can be modeled by the following relations [136]

$$C = C_s + \frac{1}{\omega^2 R^2 C_p}, \tag{231}$$

$$R = R_s + R_p + R_s \omega^2 R^2 C^2, \tag{232}$$
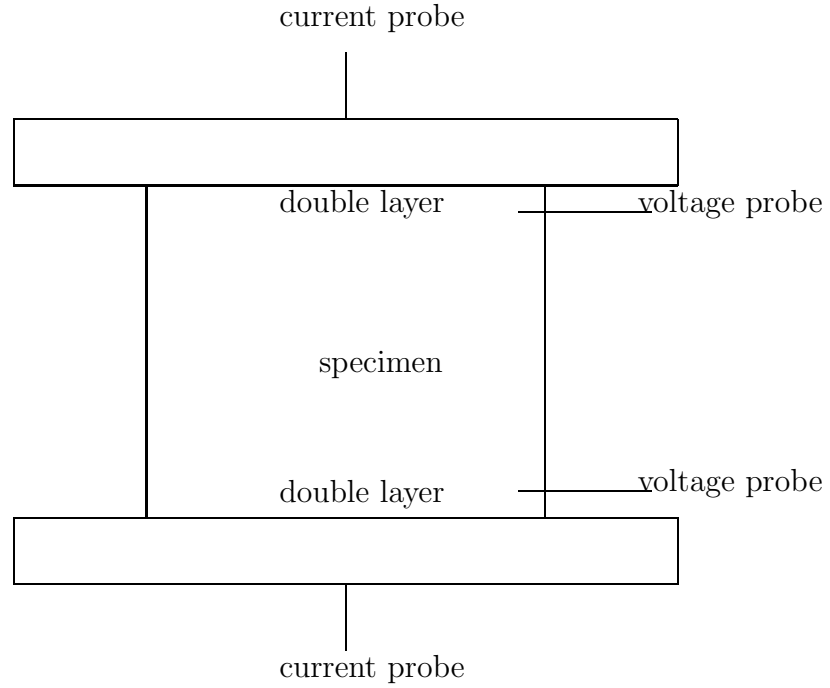
Figure 54. Capacitor with specimen for minimizing electrode polarization.

where C, R are the measured capacitance and resistance, C_p, R_p are the electrode double-layer capacitance and resistance, and C_s, R_s are the specimen capacitance and resistance. A way to partially eliminate electrode polarization is by measuring the capacitance at two separations d_1, d_2, capacitances C_1 and C_2, and resistances R_1 and R_2. Since C_p is the same for each measurement and C_s can be scaled as $C_{s2} = (d_1/d_2)C_{s1}$, we can obtain the specimen capacitance using

$$C_{1s} = \frac{C_2 - C_1 \frac{R_1^2}{R_2^2}}{\frac{d_1}{d_2} - \frac{R_1^2}{R_2^2}}. \tag{233}$$

Another way of minimizing the effects of electrode polarization is to coat the capacitor plates with platinum black [137]. This lessens the influence of electrode polarization by decreasing the second term on the right hand side of eq. (231). Probably the best approach is to bypass the electrode polarization problem altogether and use a four-probe capacitor system.

13.3.2 Four-Probe Technique

The four-probe capacitance technique (see Figure 54) overcomes electrode problems [138] by measuring the voltage drop away from the plates and thereby avoiding the double layer. The permittivity for a substance such as DNA contained in a solution, is calculated by

$$\Delta Z' = -\frac{1}{C_0}(\frac{\epsilon_0}{\sigma})^2 \Delta(\omega\epsilon''), \tag{234}$$

$$\Delta Z'' = -\frac{1}{C_0}(\frac{\epsilon_0}{\sigma})^2(\omega\epsilon'), \tag{235}$$

where $\Delta\epsilon''$ is the difference in loss between fluid with material versus fluid alone and $\Delta Z'$ and $\Delta Z''$ are the differences in real and imaginary parts of the impedance.

14.   Discussion

In this technical note we have attempted to review all of the relevant elements of metrology for measuring lossy materials. Some methods have been neglected, for example, many of the nondestructive measurement methods. We have seen that only specific types of resonant methods work for lossy materials, and as a result some variations of transmission-line methods must be used.

15.   Acknowledgments

We acknowledge discussions with Ed Kuester and Dave Hill, and Jerzy Krupka for designing and writing software for the resonant liquid fixtures. We acknowledge the support of the Departments of Justice, Homeland Security, and Dr. George Lieberman of the Office of Law Enforcement Standards of NIST.

16. References

[1] Baker-Jarvis, J.; Geyer, R. G. Nondestructive testing with a coaxial probe. URSI Digest. URSI, Boulder, CO; 1992 January. Presented at URSI.

[2] Chang, C. S.; Agrawal, A. P. Fine line thin dielectric circuit board characterization. Proc. 44th Electronic Components and Technology Conf.; pp. 564–569. IEEE Comp. Hybrids Mfg. Technol.; 1994.

[3] Westphal, W. P. Techniques of measuring the permittivity and permeability of liquids and solids in the frequency range 3 c/s to 50 kMc/s. M.I.T., Air Force Materials Lab. XXXVI; 1950.

[4] Baker-Jarvis, J.; Geyer, R. G.; Domich, P. D. A non-linear least-squares solution with causality constraints applied to transmission line permittivty and permeability determination. IEEE Trans. Instrum. Measur. 41: 646–652; 1992.

[5] Ramo, S.; Whinnery, J. R.; Duzer, T. V. Fields and Waves in Communication Electronics. New York: John Wiley and Sons; 1984.

[6] Evans, R. Effects of losses on signals in PWB's. IEEE Trans. Comp., Pkg. Mfg. Technol.: Part B 17: 217–222; 1994 May.

[7] Marks, R. B.; Williams, D. F. Characteristic impedance determination using propagation constant measurement. IEEE Microwave Guided Wave Lett. 1: 141–143; 1991 June.

[8] Marks, R. B.; Williams, D. F. A general waveguide circuit theory. J. Res. Natl. Inst. Stands. Technol. 97: 533–562; 1992 October.

[9] Baker-Jarvis, J.; Janezic, M. D.; Riddle, B.; Holloway, C. L.; Paulter, N. G.; Blendell, J. E. Dielectric and conductor-loss characterization and measurements on electronic packaging materials. Natl. Inst. Stand. Technol. Tech. Note 1520; 2001 July.

[10] Bahl, I.; Ely, K. Modern microwave substrate materials. Microwave J. 33: 131–146; 1990.

[11] Master, R. N.; Herron, L. W.; Tummala, R. R. Cofiring process for glass/copper multilayer ceramic substrate. Electronic Components and Technology Conf. pp. 5–9; 1991.

[12] Jackson, J. D. Classical Electrodynamics, 3rd Ed.. New York: John Wiley and Sons; 1999.

[13] Vanzura, E. J.; Weil, C. M.; Williams, D. F. Complex permittivity measurements of gallium arsenide using a high-performance resonant cavity. In Digest; Conf. on Precision Electromagnetic Measurements; pp. 103–104; 1992.

[14] Dyre, J. C.; Schroder, T. B. Universality of ac conductivity in disordered solids. Rev. Mod. Phys. 72: 873; 2000.

[15] Rozanski, S. A.; Kremer, F. J. Macromol. Chem. Phys. 196: 877; 1995.

[16] Baker-Jarvis, J.; Kabos, P. Nonequilibrium electromagnetics: Local and macroscopic fields using statistical mechanics. Phys. Rev. E 70: 036615–1–13; 2004.

[17] de Fornel, F. Evanescent waves from Newtonian optics to atomic optics. Berlin: Springer; 2000.

[18] Boetcher, C. J. F.; Bordewijk, P. Theory of Electric Polarization, volumes I and II. New York: Elsevier; 1978.

[19] Crenshaw, M. E.; Bowden, C. M. Lorentz local-field effects on spontaneous emission in dielectric media. Phys. Rev. A 63: 13801–1:13801–5; 2000.

[20] van Duijnen, P. T.; Vries, A. H.de; Swart, M.; Grozema, F. Polarizabilities in the condensed phase and the local fields problem: A direct field formulation. J. Chem. Phys. 117: 8442–8453; 2002.

[21] Wortmann, R.; Bishop, D. M. Effective polarizabilities and local field corrections for nonlinear optical experiments in condensed media. J. Chem. Phys. 108: 1001; 1998.

[22] Mandel, M.; Mazur, P. On the molecular theory of dielectric relaxation. Physica 24: 116–128; 1958.

[23] Gubernatis, J. E. Scattering theory and effective medium approximations to heterogeneous materials. Physica 24; pp. 84–96; 1978.

[24] Keller, O. Local fields in the electrodynamics of mesoscopic media. Phys. Reports 268: 85–262; 1996.

[25] Cole, R. H. Correlation function theory of dielectric relaxation. J. Chem. Phys. 42: 637–643; 1964.

[26] Holloway, C. L.; Kuester, E. F.; Baker-Jarvis, J.; Kabos, P. A double negative (DNG) composite material composed of magnetodielectric spherical particles in a dielectric. IEEE Trans. Antennas Propag. 51: 2596–2603; 2003.

[27] Yoo, Y. K.; Xiang, X. D. Combinatorial material preparation. J. Phys. Cond. Matter 21: R49–R78; 2002.

[28] Mazur, P.; Nijboer, B. R. A. On the statistical mechanics of matter in an electromagnetic field: I. Physica 19: 971–986; 1953.

[29] Robinson, F. N. H. Macroscopic Electromagnetism. Oxford: Pergamon Press; 1973.

[30] de Groot, S. R.; Suttorp, L. G. Foundations of Electrodynamics. New York: American Elsevier; 1972.

[31] Raab, R. E.; Cloete, J. H. An eigenvalue theory of circular birefringence and dichroism in a non-magnetic chiral medium. J. Electromagn. Waves Applicat. 8: 1073–1089; 1994.

[32] Bloch, F.; Siegert, A. Magnetic resonance for nonrotating fields. Phys. Rev. 57: 522; 1940.

[33] Kittel, C. On the theory of ferromagnetic absorption. Phys. Rev. 73: 155–163; 1947.

[34] Callen, H. B. A ferromagnetic dynamical equation. J. Phys. Chem. Solids 4: 256–270; 1958.

[35] Bloembergen, N. On the ferromagnetic resonance in nickel and Supermalloy. Phys. Rev. 78: 572–580; 1950.

[36] Vleck, J. H.van. Concerning the theory of ferromagnetic absorption. Phys. Rev. 78: 26–274; 1950.

[37] Nelson, D. F. Electric, Optic, and Acoustic Interactions in Dielectrics. New York: John Wiley and Sons; 1979.

[38] Loudon, R.; Allen, L.; Nelson, D. F. Propagation of electromagnetic energy and momentum in absorbing dielectrics. Phys. Rev. A 52: 1071–1085; 1997.

[39] Graham, E. B.; Pierrus, J.; Raab, R. E. Multipole moments and Maxwell's equations. J. Phys. B: At. Opt. Phys. 25: 4673–4684; 1992.

[40] Kittel, C. Introduction to Solid State Physics, 6th Ed. New York: John Wiley; 1986.

[41] Lewin, L. Advanced Theory of Waveguides. London, England: Iliffe; 1951.

[42] Pendry, J. B.; Holden, A. J.; Robbins, D. J.; Stewart, W. J. Magnetism from conductors and enhanced nonlinear phenomena. IEEE Trans. Phys. Microwave Theory Tech. 47: 2075–2084; 1999.

[43] Pendry, J. B.; Holden, A. J.; Stewart, W. J.; Youngs, I. Extremely low frequency plasmons in metallic mesostructures. Phys. Rev. Lett. 76: 4773–4776; 1996.

[44] Pendry, J. B.; Holden, A. J.; Robbins, D. J.; Stewart, W. J. Low frequency plasmons in thin-wire structures. J. Phys.: Condens. Matter 10: 4785–4809; 1998.

[45] Ziolkowski, R. W.; Heyman, E. Wave propagation in media having negative permittivity and permeability. Phys. Rev. E 64: 056625–1:15; 2001.

[46] Bailey, A. E. Microwave Measurement. London: Peter Peregrinus; 1985.

[47] Marks, R. B. A multiline calibration for network analyzers. IEEE Trans. Microwave Theory and Techniques 39: 1205–1215; 1991.

[48] Wong, K. H. Using precision coaxial air dielectric transmission lines as calibration and verification standards. Microwave J. pp. 83–90; 1988 December.

[49] International Organization for Standardization. Guide to the Expression of Uncertainty in Measurement; 1st Ed.; 1993.

[50] Bussey, H. E.; Steinert, L. A. Exact solution for a gyromagnetic sample and measurements on a ferrite. IRE Trans. Microwave Theory Tech. MTT-6: 72–76; 1958 January.

[51] ASTM-D3380-90 standard test method for relative permittivity and dissipation factor for polymer-based microwave circuit substrates. 1990 Annual Book of American Society for Testing of Materials (ASTM) 10.01; 1990.

[52] Papoulis, A. The Fourier Integral and Its Applications. New York: McGraw-Hill; 1987.

[53] Lynch, A. C. Relationship between permittivity and loss tangent. Proc. IEE 118: 244–246; 1971.

[54] Baker-Jarvis, J. Transmission/reflection and short-circuit line permittivity measurements. Natl. Inst. Stand. Technol. Tech. Note 1341; 1990 July.

[55] Holloway, C. L.; Kuester, E. F. Power loss associated with conducting and rough surfaces. IEEE Trans. Microwave Theory Tech. 48: 1601–1610; 2000 October.

[56] Weir, W. B. Automatic measurement of complex dielectric constant and permeability at microwave frequencies. Proc. IEEE 62(1): 33–36; 1974 January.

[57] Roberts, S.; von Hippel, A. A new method for measuring dielectric constant and loss in the range of centimeter waves. J. Appl. Phys. 7: 610–616; 1946 July.

[58] Goldfarb, R. B.; Bussey, H. E. Method for measuring complex permeability at radio frequencies. Rev. Sci. Instrum. 58(4): 624–627; 1987.

[59] Mattar, K. E.; Watters, D. G.; Brodwin, M. E. Influence of wall contacts on measured complex permittivity spectra at coaxial line frequencies. IEEE Trans. Microwave Theory Tech. MTT-39(3): 532; 1991.

[60] Baker-Jarvis, J.; Geyer, R. G.; Domich, P. D. A nonlinear optimization technique for permittivity and permeability determination. IEEE Trans. Instrum. Meas. 41(5): 646–652; 1992.

[61] Weil, C. M.; Riddle, B.; Novotney, D. R.; Johnk, R. T. Modal cutoff in coaxial transmission lines of conical and cylindrical geometries. Proc. 2001 Intl. Microwave Symposium., pp. 1229–1232; 2001.

[62] York, R. A.; Compton, R. C. An automated method for dielectric constant measurements of microwave substrates. Microwave J. 33: 115–121; 1990 March.

[63] Janezic, M. D.; Kuester, E. F.; Baker-Jarvis, J. Broadband permittivity and loss tangent measurements using a split-cylinder resonator. 2003 Ceramic Interconnect Technology Conf. pp. 101–106; 2003.

[64] Getsinger, W. J. Microstrip dispersion model. IEEE Trans. Microwave Theory Tech. IM-21: 34–39; 1973 January.

[65] Wheeler, H. A. Transmission-line properties of parallel-wide strips separated by a dielectric sheet. IEEE Trans. Microwave Theory Tech. MTT-13: 172–185; 1965 March.

[66] Bahl, I. J.; Stuchly, S. S. Analysis of a microstrip covered with a lossy dielectric. IEEE Trans. Microwave Theory Tech. MTT-28(2): 104–109; 1980 February.

[67] Tanaka, H.; Okada, F. Precise measurements of dissipation factor in microwave printed circuit boards. IEEE Trans. Instrum. Meas. IM-38(2): 509–514; 1989 April.

[68] Olyphant, M.; Ball, J. H. Stripline methods for dielectric measurements at microwave frequencies. IEEE Trans. Electron. Insul. EI-5(1): 26–32; 1970 March.

[69] Holloway, C. L.; Kuester, E. F. Edge shape effects and quasi-closed form expressions for the conductor loss of microstrip lines. Radio Sci. 29: 539–559; 1994 May-June.

[70] Holloway, C. L. Expressions for the conductor loss of strip-line and coplanar-strip (CPS) structures. Microwave Opt. Technol. Lett. 25: 162–168; 2000 May.

[71] Holloway, C. L.; Hufford, G. A. Internal inductance and conductor loss associated with the ground plane of a microstrip line. IEEE Trans. Electromagn. Compat. 39: 73–78; 1997 May.

[72] Leontovich, M. A. Approximate boundary conditions for electromagnetic fields at the surface of a highly conducting body. Issledovaniya po Rasprostraneniyu Radiovoln, part 2 5-12: 351–355; 1985.

[73] Booth, J. C.; Holloway, C. L. Conductor loss in superconducting planar structures: Calculations and measurements. IEEE Trans. Microwave Theory Tech. 47: 769–773; 1999 June.

[74] Kuester, E. Accurate approximations for a function appearing in the analysis of microstrip. IEEE Trans. Microwave Theory Tech. 32: 131–133; 1984.

[75] Laverghetta, T. S. Microwave Materials and Fabrication Techniques. New York: Artech House; 1990.

[76] Holloway, C. L.; Kuester, E. F. A quasi-closed form expression for the conductor loss of CPW lines, with an investigation of edge shape effects. IEEE Trans. Microwave Theory Tech. 12: 2695–2701; 1995 December.

[77] Carin, L.; Sichina, J.; Harvey, J. F. Microwave underground propagation and detection. IEEE Trans. Phys. Microwave Theory Tech. 50: 945–952; 2002.

[78] Zoubir, A. M.; Chant, I.; Brown, C. L.; Barkat, B.; Abeynayake, C. Signal processing techniques for landmine detection using impulse ground penetrating radar. IEEE Sensors Journal 2: 41–51; 2002.

[79] Zhang, J.; Nakhkash, M.; Huang, Y. In-situ characterisation of building materials. 11th International Conf. on Antennas Propag. 1: 269–274; 2001.

[80] van Morrow, I. L.; Gendren, P. Effective imaging of buried dielectric objects. IEEE Trans. Geosc. Remote Sens. 40: 943–949; 2002.

[81] Oguz, U.; Gurel, L. Frequency responses of ground-penetrating radars operating over highly lossy grounds. IEEE Trans. IEEE Trans. Geosc. Remote Sens. 40: 1385–1394; 2002.

[82] Chignell, R. J. Buried object detection using ground penetrating radar. Proceedings Intelligent Sensors, DERA/IEE Workshop, Orlando, FL; 2000.

[83] Pirri, M.; Lombardo, P.; Bucciarelli, T. Performance assessment of wide-band pulsed GPR for archaeological applications. Proceedings IEEE Trans. Geosc. Remote Sens. Symp., IGARSS. Orlando, FL; 2000.

[84] Grosvenor, C. A.; Johnk, R.; Novotny, D.; Canales, S.; Baker-Jarvis, J.; Janezic, M. D. Electrical material property measurements using a free-field, ultra-wideband system. Proc. 2004 CEIDP, pp. 174–177; 2004.

[85] Wells, T. Measurements of permittivity and/or permeability at elevated temperatures centimeter/millimeter wave. Proc. AMTA Workshop; pp. 50–62; Chicago, Il; 1992 July.

[86] Ghodgaonkar, D. K.; Varadan, V. V.; Varadan, V. K. Free-space measurement of complex permittivity and complex permeability of magnetic materials at microwave frequencies. IEEE Trans. Instrum. Measur. 39: 387–394; 1990.

[87] Muscil, J.; Zacek, F. Microwave Measurements of Complex Permittivity by Free-Space Methods and Their Applications. New York: Elsevier; 1986.

[88] Chen, X. D.; Grzesarczyk, T. M.; Wu, B. I.; Pacheco, J.; Kong, J. A. Robust method to retrieve the constitutive effective parameters of metamaterials'. Phys. Rev. E 70: 16608; 2004.

[89] Pendry, J.; Negative refraction makes a perfect lens. Phys. Rev. Lett. 85: 3966; 2000.

[90] Maslovski, S.; Trekyakov, S.; Alitalo, P. Near-field enhancement and imaging in double negative planar polariton-resonant structures. J. Appl. Phys. 96: 1293; 2004.

[91] Boughriet, A.-H.; Legrand, C.; Chapoton, A. Noniterative stable transmission/reflection method for low-loss material complex permittivity determination. IEEE Trans. Microwave Theory and Techniques 45: 52–57; 1997.

[92] Bussey, H. E. Measurement of rf properties of materials: A survey. Proc., IEEE 55(6): 1046–1053; 1967 June.

[93] Bussey, H. E.; Gray, J. E. Measurement and standardization of dielectric samples. IRE Trans. Instrum. I-11(3): 162–165; 1962.

[94] Nicolson, A. M.; Ross, G. F. Measurement of the intrinsic properties of materials by time domain techniques. IEEE Trans. Instrum. Meas. IM-19: 377–382; 1968 November.

[95] Levine, H.; Papas, C. H. Theory of the circular diffraction antenna. J. Appl. Phys. 22(1): 29–43; 1951 January.

[96] Mosig, J. R.; Besson, J.-C. E.; GE-Fabry, M.; Gardiol, F. E. Reflection of an open-ended coaxial line and application to non-destructive measurement of materials. IEEE Trans. Instrum. Meas. 30(1): 46–51; 1981.

[97] Stuchly, M. A.; Stuchly, S. S. Coaxial line reflection methods for measuring dielectric properties of biological substances at radio and microwave frequencies-A review. IEEE Trans. Instrum. Meas. IM-29: 176–183; 1980.

[98] Li, L. L.; Ismail, N. H.; Taylor, L. S.; Davis, C. C. Flanged coaxial microwave probes for measuring thin moisture layers. IEEE Trans. Biomed. Eng. 39(1): 49–57; 1992 January.

[99] Baker-Jarvis, J.; Janezic, M. D.; Domich, P. D.; Geyer, R. G. Analysis of an open-ended coaxial probe with lift-off for nondestructive testing. IEEE Trans. Instrum. Meas. 43(5): 711–718; 1994 October.

[100] Jenkins, S.; Hodgetts, T. E.; Symm, G. T.; Warhamm, A. G. P.; Clarke, R. N. Comparison of three numerical treatments for the open-ended coaxial line sensor. Electron. Lett. 26: 234–235; 1990.

[101] Rasmussen, A. L.; Enfield, A. W.; Hess, A. Advances in the design and application of the radiofrequency permeameter. J. Res. Nat. Bur. Stand. (U.S.); 56(5): 261–267; 1960.

[102] Hoer, C. A.; Rasmussen, A. L. Equations for the radiofrequency magnetic permeameter. J. Res. Nat. Bur. Stand. 67C: 69– 76; 1963 March.

[103] Powell, R. C.; Rasmussen, A. L. A radio-frequency permittimeter. IRE Transactions on Instrumentation I-9(2): 179–184; 1960.

[104] Janezic, M. D.; Baker-Jarvis, J. Permeability of metals. Natl. Inst. Stand. Technol. Tech. Note 1532; 2004 August.

[105] Alexander, C.; Rantchler, J.; Silva, T. J.; Kabos, P. Frequency and time-resolved measurements of FeTaN films with longitudinal bias fields. J. Appl. Phys. 87: 6623–6635; 2000.

[106] Krupka, J.; Klinger, M.; Kuhn, M.; Baranyak, A.; Stiller, M.; Hinken, J. Surface resistance measurements of HTS films by means of sapphire dielectric resonators. IEEE Trans. Appl. Supercond. 3: 3043–3048; 1993.

[107] Baker-Jarvis, J.; Janezic, M. D. The two-port coaxial probe for thin materials. IEEE Trans. Electromagn. Compat. 38: 67–70; 1996.

[108] Marcuvitz, N. Waveguide Handbook. New York: Dover Publications; 1951.

[109] Nozaki, R.; Bose, T. Complex permittivity measurements by time-domain spectroscopy. IEEE Trans. Instrum. Meas. 39: 945–951; 1990.

[110] Belhadj-Tahar, N.-E.; Fourier-Lamer, A.; Chanterac, H. Broadband simultaneous measurement of complex permittivity and permeability using a coaxial discontinuity. IEEE Trans. Microwave Theory Tech. 38(1): 1–7; 1990 January.

[111] Gregory, A. P.; Clarke, R. N. Tables of complex permittivity of dielectric reference liquids at frequencies up to 5 GHz. National Physical Laboratory; NPL Report CETM 33; 2001.

[112] Baker-Jarvis, J.; Janezic, M. D. Broadband dielectric measurement of liquids. Proceedings of 2004 CEIDP pp. 17–20; 2004.

[113] Krupka, J.; Derzakowski, K.; Janezic, M. D.; Baker-Jarvis, J. $Te_{01\delta}$ dielectric resonator technique for the precise measurement of the complex permittivity of lossy liquids below 1 GHz. CPEM Digest; 2004.

[114] Bussey, H. E. Dielectric measurements in a shielded open circuit coaxial line. IEEE Trans. Instrum. Meas. IM-29: 120–124; 1980 June.

[115] Baker-Jarvis, J.; Janezic, M. D.; Jones, C. A. Shielded open-circuited sample holder for dielectric measurements of solids and liquids. IEEE Trans. Instrum. Measur. 47: 338–344; 1998.

[116] Baker-Jarvis, J.; Janezic, M. D.; Stafford, R. Analysis of an open-circuited sample holder for dielectric and magnetic measurements of liquids and powders. Natl. Inst. Stand. Technol. NISTIR 5001; 1992.

[117] Jenkins, S.; Hodgetts, T. E.; Clarke, R. N.; Preece, A. W. Dielectric measurements on reference liquids using automatic network analyzers and calculable geometries. Meas. Sci. Tech. 1: 691–702; 1990.

[118] von Hippel, A. Dielectric Materials and Applications. Cambridge, MA: M.I.T. Press; 1954.

[119] Scott, W. R.; Smith, G. S. Error analysis for dielectric spectroscopy using shielded open-circuited coaxial lines of general length. IEEE Trans. Instrum. Meas. IM-35: 130–137; 1986 June.

[120] Hill, P. N.; Green, H. E. In situ measurement of soil permittivity and permeability. J. Elect. Elect. Eng., Australia 2(4): 205–209; 1982 December.

[121] Jesch, R. L. Dielectric measurements of oil shales as functions of temperature and frequency. IEEE Trans. Geosci. Remote Sensing GE-22(2): 99–105; 1984 March.

[122] Somlo, P. I. The discontinuity capacitance and the effective position of a shielded open circuit in a coaxial line. Proc. Inst. Radio Elec. Eng. Australia 28(1): 7–9; 1967 January.

[123] Stricklett, K. L.; Baker-Jarvis, J. Electrical properties of biological materials: A bibliographic survey. Natl. Inst. Stand. Technol. NISTIR 6564; 2001.

[124] Gabriel, C.; Grant, E. H.; Tata, R.; Brown, P. R.; Gestblom, B.; Noreland, E. Microwave absorption in aqueous solutions of DNA. Nature 328: 145–146; 1987.

[125] Broadhurst, M. G.; Chiang, C. K.; Davis, G. T. Dielectric phantoms for electromagnetic radiation. J. Mole. Solids 36: 47–64; 1987.

[126] Kobayashi, T.; Nojima, T.; Yamada, K.; Uebayashi, S. Dry phantom composed of ceramics and its application to SAR estimation. IEEE Trans. Microwave Theory Tech. 41: 136–140; 1993.

[127] Hagmann, M. J.; Calloway, R.; Osborn, A.; Foster, K. Muscle equivalent phantom materials for 10-100 MHz. IEEE Trans. Microwave Theory Tech. 40: 760–762; 1992.

[128] Nikawa, Y.; Chino, M.; Kikuchi, K. Soft and dry phantom modeling material using silicone rubber with carbon fiber. IEEE Trans. Microwave Theory Tech. 44: 1949–1953; 1996.

[129] Chou, C.; Chen, G.; Guy, A.; Luk, K. Formulas for preparing phantom muscle tissue for various radiofrequencies. Bioelectromagn. 5: 435–441; 1984.

[130] Andreuccetti, D.; Bini, M.; Ignesti, A. Use of polyacrylamide as a tissue-equivalent material in the microwave range. IEEE Trans. Biomed. Eng. 35: 275–277; 1988.

[131] Kato, H.; Ishida, T. Development of an agar phantom adaptable for simulation of various tissues in the range 5-40 MHz. Phys. Med. Bio. 32: 221–226; 1987.

[132] Marchal, C.; Nadi, M.; Tosser, A. J.; Roussey, C.; Gaulard, M. L. Dielectric properties of gelatine phantoms used for simulations of biological tissues between 10 and 50 MHz. Int. I. Hyperthermia 5(6): 725–732; 1989.

[133] Broadhurst, M. G.; Bur, A. J. Two-terminal dielectric measurements up to 6×10^8 Hz. J. Res. Nat. Bur. Stand. (U.S.) 69C(3): 165–172; 1965.

[134] Clarke, R. A guide to the dielectric characterisation of materials at RF and microwave frequencies. National Physical Laboratory; NPL; 2003.

[135] Schwan, H. P. Linear and nonlinear electrode polarization and biological materials. Ann. Biomed. Eng. 20: 269–288; 1992.

[136] Takashima, S. Dielectric dispersion of deoxyribonucleic acid. J. Phys. Chem. 70(5): 1372–1379; 1966.

[137] Schwan, H. P. Electrical properties of tissue and cell suspensions. Advances in Biological and Medical Physics; Laurence, J.; Tobias, C. A., Editors pp. 147–209. Academic Press; 1957.

[138] Bernengo, J. C.; Hanss, M. Four-electrode, very-low-frequency impedance comparator for ionic solutions. Rev. Sci. Instrum. 47: 505–508; 1976.

[139] Microelectronics packaging materials database. Center for Information and Numerical Data Synthesis and Analysis (CINDAS); 2002.

[140] Jones, C. A.; Grosvenor, J. H.; Weil, C. M. RF material characterization using a large-diameter (76.8 mm) coaxial air line. Natl. Inst. Stand. Technol. Tech. Note 1517; 2000 February

[141] Al-Qadi, I. L.; Hazim, A.; Su, W.; Riad, S. M. Dielectric properties of Portland cement concrete at low radio frequencies. Journal of materials in Civil Engineering 7: 192–198; 1995.

[142] Mubarak, K.; Bois, K. J.; Zoughi, R. A simple, robust, and on-site microwave technique for determining water-to-cement ratio (w/c) of fresh Portland cement-based materials. IEEE Trans. Instrum. Measur. 50: 1255–1263; 2001.

[143] Olmi, R.; Bini, M.; Ignesti, A.; Riminesi, C. Nondestructive permittivity measurement of solid materials. Meas. Sci. Technol. 11: 1623–1629; 2000.

[144] Beek, A. Dielectric properties of young concrete. PhD thesis; Delft University Press, Delft, Netherlands,2000.

[145] Chew, W. C.; Olp, K. J.; Otto, G. P. Design and calibration of a large broadband dielectric measurement cell. IEEE Trans. IEEE Trans. Geosc. Remote Sens. 29: 42–47; 1998.

[146] Maierhofer, C.; Wostmann, J. Investigation of dielectric properties of brick materials as a function of moisture and salt content using a microwave impulse technique at very high frequencies. NDT and E International 31: 259–263; 1998.

[147] Sarabandi, K.; Li, E. S.; Nashashibi, A. Modeling and measurements of scattering from road surfaces at millimeter-wave frequencies. IEEE Trans. Antennas Propag. 45: 1679–1688; 1997.

[148] Taherian, M. R.; Yeun, D. J.; Habashy, T. M.; Kong, J. A. A coaxial-circular waveguide for dielectric measurement. IEEE Trans. Geosci Remote Sens. 29: 321–330; 1991.

[149] Nyfors, E.; Vainikainen, P. Industrial Microwave Sensors; Artech House Inc. 1989.

[150] Richalot, E.; Bonilla, M.; Wong, M.-F.; Fouad-Hanna, V.; Baudrand, H.; Wiart, J. Electromagnetic propagation into reinforced-concrete walls. IEEE Trans. Microwave Theory Techn. 48: 357–366; 2000.

[151] Bouchilloux, P.; Lhermet, N.; Claeyssen, F. Electromagnetic stress sensor for bridge cables and prestressed concrete structures. J. Intell. Mater. Sys. Structures 10: 397–401; 1999.

[152] Cuinas, I.; Pugliese, J.-P.; Hammoudeh, A. Frequency dependence of dielectric constant of construction materials in microwave and millimeter-wave bands. Microwave Opt. Technol. Lett. 30: 123–124; 2001.

[153] Pena, D.; Feick, R.; Hristov, H. D.; Grote, W. Measurment and modeling of propagation losses in brick and concrete walls for the 900-MHz band. IEEE Trans. Antennas Propag. 51: 31–39; 2003.

[154] Kharkovsky, S. N.; Akay, M. F.; Hasar, U. C.; Atis, C. D. Measurement and monitoring of microwave reflection and transmission properties of cement-based specimens. Proc. 18th IEEE Instrum. Measur. Technology Conf., 1: 513–518; 2001.

[155] Kharkovsky, S. N.; Akay, M. F.; Hasar, U. C.; Atis, C. D. Measurement and monitoring of microwave reflection and transmission properties of cement-based specimens. IEEE Trans. Instrum. Measur. 51: 1210–1218; 2002.

[156] Peer, S.; Case, J. T.; Gallaher, E.; Kurtis, K. E.; Zoughi, R. Microwave reflection and dielectric properties of mortar subjected to compression force and cyclically exposed to water and sodium chloride solution. IEEE Trans. on Instrum. Measur.Instrum. Measur, 52: 111–118; 2003.

[157] Tarng, J. H.; Perng, D. W. Modeling and measurements of UHF radio propagating through floors in a multifloored building. Proc. IEE Microwaves, Antennas Propag., 144: 359–263; 1997.

[158] Honcharenko, W.; Bertoni, H. L. Transmission and reflection characteristics at concrete block walls in the UHF bands proposed for future PCS. IEEE Trans. Antennas Propag. 42: 232–239; 1994.

[159] Hasted, J. B.; Shah, M. A. Microwave absorption by water in building materials. Brit. J. Appl. Phys. 15: 825–836; 1964.

[160] Shah, M. A.; Hasted, J. B.; Moore, L. Microwave aborption by water in building materials: Aerated concrete. Brit. J. Appl. Phys. 16: 1747–1754; 1965.

[161] Baker-Jarvis, J.; Geyer, R. G.; Grosvenor, J. H.; Janezic, M. D.; Jones, C. A.; Riddle, B.; Weil, C. M.; Krupka, J. Dielectric characterization of low-loss materials: A comparison of techniques. IEEE Trans. Dielect. Elect.Insul. 5; 1998 August.

[162] Krupka, J.; Derzakowski, K.; Riddle, B.; Baker-Jarvis, J. A dielectric resonator for measurements of complex permittivity of low loss dielectric materials as a function of temperature. Meas. Sci. Technol. 9: 1751–1756; 1998.

[163] Krupka, J.; Derzakowski, K.; Tobar, M.; Hartnett, J.; Geyer, R. Complex permittivity of some ultralow loss dielectric crystals at cryogenic temperatures. Meas. Sci. Technol. 10: 387–392; 1999.

[164] Bur, A. J. Dielectric properties of polymers at microwave frequencies: a review. Polymer 26; 1985 July.

[165] Ehrlich, P. Dielectric properties of Teflon from room temperature to 314° C and from frequencies of 10^2 to 10^5 c/s. J. Res. Nat. Bur. Stand. (U.S.) 51; 1953.

[166] Mazur, K. More data about dielectric and electret properties of poly(methyl methacrylate). J. Phys. D: Appl. Phys. 30; 1997.

[167] McCammon, R. D.; Saba, R. G.; Work, R. N. Dielectric properties of polystyrene and some polychlorostyrenes from 4 K to room temperature. J. Polymer Sci: Part A-2 7; 1969.

126

[168] Pillai, P. K. C.; Rashmi. Dielectric properties of polystyrene and some related polymers. Intern. J. Polymeric Mater. 8; 1980.

[169] Aras, L.; Baysal, B. M. Dielectric relaxation studies of some linear crosslinked and branched polymers. J. Polymer Sci: Polymer Phys. Ed. 22; 1984.

[170] Bergman, R.; Alvarez, F.; Alegria, A.; Colmenero, J. Dielectric relaxation in PMMA revisted. J. Non-Crystalline Solids pp. 580–583; 1998.

[171] Chaki, T. K.; Khastgir, D. K. Effect of frequency and temperature on dielectric properties of polypropylene at X-Band microwave region. J. Elastomers Plastics 22; 1990.

[172] Touloukian, Y. S.; Kirby, R. K.; Taylor, R. E.; Lee, T. Y. R. Thermal Expansion Nonmetallic Solids, volume 13. Thermophysical Properties of Matter: IFI/Plenum. 1977.

[173] James, W. L.; Yen, Y.-H.; King, R. J. A microwave method for measuring moisture content, density, and grain angle of wood. United States Department of Agriculture Research Note FPL-0250; 1985.

[174] Torgovnikov, G. I. Dielectric properties of wood and wood-based materials. New York: Springer-Verlag; 1993.

[175] Suzuki, H.; Mohan, A. S. Measurement and prediction of high spatial resolution indoor radio channel characteristics map. IEEE Trans. Vehicular Technol. 49: 1321–1333; 2000.

[176] Lahteenmaki, J.; Karttaavi, T. Measurement of dielectric parameters of wall materials at 60 GHz band. Electron. Lett. 32: 1442–1444; 1996.

[177] Jones, R. N.; Bussey, H. E.; Little, W. E.; Metzker, R. F. Electrical characteristics of corn, wheat, and soya in the 1- 200 MHz range. nat. Bur. Stds.(U.S.) NBSIR 78-897; 1978.

[178] Blackham, D. Use of open-ended coaxial probe to determine permittivity. In Microwave Power Symposium; pp. 44–45. International Microwave Power Institute; 1990 August.

[179] King, R. J.; King, K. V.; Woo, K. Moisture measurements of grains. IEEE Trans. Instrum. Meas. 41: 111–115; 1992.

[180] Regier, M. Dielectric properties of mashed potatoes. Int. J. Food Prop. 4: 431–439; 2001.

[181] Narayanan, R. M. Free-space microwave measurements of low moisture content in powdered foods. Trans. ASAE 43: 1733–1736; 2000.

[182] Ryynanen, S. Electromagnetic properties of food materials: A review of the basic principles. J. Food Eng. 26: 409–429; 1995.

[183] Calay, R. K. Prediction equations for the dielectric properties of foods. Int. J. Food Techn. 29: 699–713; 1994.

[184] Tong, C. H. Dielectric properties of bentonite pastes as a function of temperature. J. Food Process Pres. 17: 139–145; 1993.

[185] Bodakian, B.; Hart, F. X. The dielectric properties of meat. IEEE Trans. Dielect. Insul. 1: 181–187; 1994 April.

[186] Evans, S.; Michelson, S. C. Intercomparison of dielectric reference materials available for the calibration of an open-ended probe at different temperatures. Meas. Sci. Technol. 6: 1721–1732; 1995.

[187] Hartshorn, L.; Parry, J. V. L.; Essen, L. The measurement of the dielectric constant of standard liquids. Proc. Physical Society, B LXVIII: 422–446; 1955.

[188] Gregory, A. P.; Clarke, R. N.; Hodgetts, T. E.; Symm, G. T. Rf and microwave dielectric measurements upon layered materials using a reflectometric coaxial sensor. National Physical Laboratory NPL Report DES 125; 1993 March.

[189] Price, A. H. Dielectric measurements on liquids in the frequency range 250 MHz to 140 GHz. In High frequency dielectric measurements; Chamberlain, J.; Chantry, G. W., Ed., pp. 28–33. IPC Science and Technology Press; 1973.

[190] Cachet, H.; Lestrade, J. C.; Badiali, J. P. A measurement technique suited to the dielectric study of electrolyte solutions. High frequency dielectric measurements. In Chamberlain, J.; Chantry, G. W., Ed., pp. 38–41. IPC Science and Technology Press; 1973.

[191] Clarke, R. N. A re-entrant cavity method for the measurement of non-linear polarization in organic liquids. High frequency dielectric measurements. In Chamberlain, J.; Chantry, G. W., editors, pp. 56–59. IPC Science and Technology Press; 1973.

[192] Baker-Jarvis, J.; Janezic, M. D.; Jones, C. A. Shielded open-circuited sample holder for dielectric measurements of solids and liquids. IEEE Trans. Instrum. Meas. 47: 338–344; 1998 April.

[193] Hodgetts, T. E. The open-ended coaxial line: A rigorous variational treatment. Royal Signals and Radar Establishment 4331; 1989.

[194] Kunz, W. Structure of Water and Ionic Hydration. Birkhauser Verlag; Basel, Switzerland; 1995.

[195] Hasted, J. B. Aqueous Dielectrics. New York: John Wiley and Sons; 1973.

[196] Marsland, M. A.; Evans, S. Dielectric measurements with an open-ended coaxial probe. IEE Proc. 134: 341–349; 1987.

[197] Dikarev, B. N. Conduction currents and dielectric properties of engine oils. Proceedings on the 5th Intl. Conf. on Properties and Applications of Dielectric Materials; pp. 124–127. IEEE; 1997.

[198] Olhoeft, G. R. Applications and frustrations in using ground penetrating radar. IEEE AESS Systems Magazine; pp. 12–20; 2002.

[199] Stuchly, S. S.; Bassey, C. E. Coplanar microwave sensor for industrial applications. Proc. 12th Intl. Conf. Microwaves and Radar, MIKON'98; 3, pp. 755–759; 1998.

[200] Fouracre, R. A. Dielectric measurements of radiation induced effects in polyethersulphone. Proc. IEEE 5th Intl. Conf. Conduction and Breakdown in Solid Dielectics; pp. 43–47; 1995.

[201] He, Y. D.; Shen, L. C. Measurement of complex permittivity of materials using a monopole antenna. IEEE Trans. Geosci. Remote Sensing 30: 624–627; 1992.

[202] Bernard, P. A.; Gautray, J. M. Measurement of dielectric constant using a microstrip ring resonator. IEEE Trans. Microwave Theory Tech. 39: 592–595; 1991.

[203] J. Boiskarl; Benally, A. D.; Zoughi, R. Multimode solution for the reflection properties of an open-ended rectangular waveguide radiating into a dielectric half-space: The forward and inverse problems. IEEE Trans. Instrum. Meas. 48: 1131–1140; 1999.

[204] J. Boiskarl; F. Handjojolarry; Benally, A. D.; Mubarak, K.; Zoughi, R. Dielectric plug-loaded two port transmission line measurement technique for dielectric property characterization of granular and liquid materials. IEEE Trans. Instrum. Meas. 48: 1141–1148; 1999.

[205] Stone, W. C. Electromagnetic signal attenuation in construction materials. Natl. Inst. Stand. Technol. NISTIR 6055; 1997.

[206] Stone, W. C. Surveying through solid walls; Automation Robotics Construction, Proc. 14th Internation Symposium, Pittsburgh, PA pp. 22–40. 1997.

[207] Baker-Jarvis, J.; Jones, C. A.; Riddle, B.; Janezic, M. D.; Geyer, R. G.; Grosvenor, J. H.; Weil, C. M. Dielectric and magnetic measurements: A survey of nondestructive, quasi-nondestructive, and process-control techniques. Res. Nondestruct. Eval. 7: 117–136; 1996.

[208] Liebe, H. J.; Hufford, G.; Manabe, T. A model for the complex permittivity of water at frequencies below 1 THz. Int. J. Infrared Millimeter Waves 12: 659–673; 1991.

130

[209] Fernandez, D. J.; Mulev, Y.; Goodwin, A. R. H.; Sengers, J. M. H. A database for the static dielectric constant of water and steam. J. Phys. Chem. Ref. Data 24: 33–65; 1995.

[210] Nandi, N.; Bhattacharyya, K.; Bagchi, B. Dielectric relaxation and solvation dynamics of water in complex chemical and biological systems. Chem. Rev. 100: 2013–2045; 2000.

[211] Vogelhut, P. The dielectric properties of water and their role in enzyme-substrate interactions. Electronics Research Laboratory Series 60, (476); 1962.

[212] Buckley, F.; Maryott, A. A. Tables of dielectric dispersion data for pure liquids and dilute solutions. Nat. Bur. Stds. (U.S.) Circular 589; 1958.

[213] Hippel, A.von. The dielectric relaxation spectra of water, ice, and aqueous solutions and their interpretation. Laboratory of Insulation Research Technical Reports 1 and 2; 1967.

[214] Gerhardt, R. A.; Cao, W. Distinguishing bulk water from adsorbed water via dielectric measurements. Proc. Electrical Insulation and Dielectric Phenomena Conf.; vol. 1; 102–105. IEEE; 1996.

[215] Hong, S. J.; Kim, K. J.; Lee, J. R. Moisture effects on the penetration loss through exterior building walls. Vehicular Technology Conf., 1998. VTC 98. 48th IEEE 2: 860–864; 1998.

[216] Saxton, J. A.; Lane, J. A. Electrical properties of sea water. Wireless Eng. 29: 269–275; 1952.

[217] Ho, W.; Hall, W. F. Measurements of the dielectric properties of seawater and NaCl solutions at 2.65 GHz. J. Geophys. Res. 78: 6301–6315; 1973.

[218] Hasted, J. B.; Ritson, D. M.; Collie, C. H. Dielectric properties of aquatic ionic solutions: Parts I and II. J. Chem. Phys. 16: 1–21; 1948.

[219] Haggis, G. H.; Hasted, J. B.; Buchanan, T. J. The dielectric properties of water in solutions. J. Chem. Phys. 29: 1452–1465; 1952.

[220] Hufford, G. A model for the complex permittivity of ice at frequencies below 1 THz. Int. J. Infrared and Millimeter Waves 12: 677–682; 1991.

[221] Hallikainen, M. T.; Ulaby, F.; Abdelrazik, M. Dielectric properties of snow in the 3 to 37 GHz range. IEEE Trans. Antennas Propag. 34: 1329–1340; 1986 November.

[222] Curtis, J. O. A durable laboratory apparatus for the measurement of soil dielectric properties. IEEE Trans. Instrum. Meas. 50: 1364–1369; 2001.

[223] Dobson, M. C.; Ulaby, F. T.; Hallikainen, M. T.; El-Rayes, M. A. Microwave dielectric behavior in wet soils:Part II: Empirical models and experimental observations. IEEE Trans. IEEE Trans. Geosc. Remote Sens., 23: 35–45; 1985.

[224] Hallikainen, M. T.; Ulaby, F. T.; Dobson, M. C.; El-Rayes, M. A.; Wu, L.-K. Microwave dielectric behavior in wet soils:Part I: Empirical models and experimental observations. IEEE Trans. IEEE Trans. Geosc. Remote Sens., 23: 25–34; 1985.

[225] Anis, M. K.; Jonscher, A. K. Frequency and time-domain measurements on humid sand soil. J. Mater. Sci. 28: 3626–3634; 1993.

[226] Roth, C. H.; Malicki, M. A.; Plagge, R. Empirical evaluation of the relationship between soil dielectric constant and volumetric water content as the basis for calibrating soil moisture measurements by TDR. J. Soil Sci. 43: 1–14; 1992.

[227] Klein, K.; Carlos, J. Frequency and time-domain measurements on humid sand soil. Geotechn. Testing J. 20: 168–179; 1997.

[228] Jesch, R. L. Dielectric measurements of four different soil texture types as a function of frequency and moisture content. Nat. Bur. Stand. (U.S.) NBSIR 78-896; 1978.

[229] Geyer, R. G. Dielectric mixing rules for background test soils. Natl. Inst. Stand. Technol. NISTIR 1517; 1988.

[230] Holdem, J. R.; Keam, R. B.; Schoonees, J. A. Estimation of the number of frequencies and bandwidth for the surface measurement of soil moisture as a function of depth. IEEE Trans. Instrum. Meas. 49: 964–970; 2000.

[231] Skulski J.; Galwas, B. A. Planar resonator sensor for moisture measurements. Proc. 12th Int. Conf. on Microwaves and Radar MIKON'98, vol. 3; pp. 692–695; 1998.

[232] Curtis, J. O. Effect of soil composition on complex dielectric properties. U.S. Army Corps of Engineers EL-95-34; 1995.

[233] Challa, S.; Little, W. E.; Cha, C. Y. Measurements on the dielectric properties of char at 2.45 GHz. J. Microwave Power Electromagn. Energy 29: 131–137; 1994.

[234] Baker-Jarvis, J.; Inguva, R. Dielectric heating of oilshales by monopole and coaxial applicators. J. Microwave Power 23: 160–170; 1988.

[235] Baker-Jarvis, J.; Inguva, R. Electromagnetic heating of oilshales. Fuel 67: 916–926; 1988.

[236] Inguva, R.; Baker-Jarvis, J. Oil shale retorting using electromagnetic methods. DE-AC21-85LC11060 DOE; 1988.

[237] Baker-Jarvis, J.; Inguva, R. Dielectric heating of oilshales by monopole and coaxial applicators. J. Microwave Power 23: 160–170; 1988.

[238] Baker-Jarvis, J.; Inguva, R. Electromagnetic heating of oilshales. Fuel 67: 916–926; 1988.

[239] Balanis, C. A.; Rice, W. S.; Smith, N. S. Microwave measurements of coal. Radio Sci. 11: 413–418; 1976.

[240] Hartsgrove, G.; Kraszewski, A.; Surowiec, A. Simulated biological materials for electromagnetic radiation absorption studies. Bioelectromagn., 8: 29–36. 1987.

[241] Foster, K. R.; Schwan, H. P. Dielectric properties of tissues and biological materials: A critical review; volume 17; pp. 25–104. CRC Press; 1989.

[242] Broadhurst, M. G.; Chiang, C. K.; Wahlstrand, K. J.; Hill, R. M.; Dissado, L. A.; Pugh, J. The dielectric properties of biological tissue fro 10^{-2} to 10^9 hz. J. Molecular Liquids 36: 65–73; 1987.

[243] Toler, J.; Seals, J. RF dielectric properties measurement system: Human and animal. U. S. Department Health, Education, and Welfare, No. 77-176; 1977.

[244] Laverghetta, T. S. Microwave Materials and Fabrication Techniques. Boston: Artech House; 2000.

[245] Gershon, D.; Calame, J. P.; Birnbolm, A. Complex permittivity measurements and mixing laws of alumina composites. J. Appl. Phys. 89: 8110–8116; 2001.

[246] Sihvola, A. Electromagnetic Mixing Formulas and Applications. London: Institution of Electrical Engineers; 1999.

[247] Sthraus, V. D.; Mikel'son, M. Y. Effect of low cycle loading on the mechanical and low-frequency dielectric characteristics of a number of polymer and composite materials. Mechanics of Composite Materials; pp. 253–258. Soviet Press; 1983.

[248] Nakamura, S.; Saitokazuhiko; Sawa, G. Electrical field dependence of conductivity and critical exponent of it for carbon black-resin composites. Proc. Seventh Int. Conf. Dielectric Materials Measurements and Applications; pp. 96–99. IEE; 1996.

[249] Nakamura, S.; Tomimura, T.; Sawa, G. Electrical conduction mechanism of polymer carbon black composites below and above the percolation threshold. Proc.Electrical Insulation and Dielectric Phenomena; 1; pp. 265–268. IEEE; 1998.

[250] Nakamura, S.; Tomimura, T.; Sawa, G. Dielectric properties of carbon black-polyethylene composites below the percolation threhold. Proc.Electrical Insulation and Dielectric Phenomena; 1; pp. 293–296. IEEE; 1999.

[251] Mantese, J. V.; Michell, A.; Dungan, D.; Geyer, R. G.; Baker-Jarvis, J.; Grosvenor, J. H. Applicability of effective medium theory to ferroelectric/ferrimagnetic composites

with composition and frequency-dependent complex permittivities and permeabilities. J. Appl. Phys. 79: 1655–1660; 1996.

[252] Ganchev, S.; Bakhtiari, S.; Zoughi, R. Calibration and measurement of dielectric properties of finite thickness composite sheets with open-ended coaxial sensors. IEEE Trans. Instrum. Meas. 44; 1023 - 1029, 1995.

[253] Tittle, C. W. Boundary value problems in composite media: Quasi- orthogonal functions. J. Appl. Phys. 36(4): 1486–1488; 1965 April.

[254] Traut, G. R. Clad laminates of PTFE composites for microwave antennas. Microwave J. 23: 47–53; 1980 November.

[255] Geyer, R.; Baker-Jarvis, J.; Vanderah, T.; Mantese, J. Complex permittivity and permeability estimation of composite electroceramics. J. Am. Ceram. Soc. 88: 115–120; 1998.

[256] McLachlan, D. S. Analytical functions for the dc and ac conductivity of conductor-insulation composites. J. Electroceramics 52: 93–110; 2000.

[257] Kraszewski, A. Prediction of the dielectric properties of two-phase mixtures. J. Microwave Power 12: 215–222; 1977.

[258] Sato, K.; Kozima, H.; Masuzawa, H.; Manabe, T.; Ihara, T.; Kasashima, Y.; Yamaki, K. Measurements of reflection characteristics and refractive indices of interior construction materials in millimeter-wave bands. Vehicular Technology Conf., 1995 IEEE 45th 1: 449–453; 1995.

[259] Sato, K.; Manabe, T.; Ihara, T.; Saito, H.; Ito, S.; Tanaka, T.; Sugai, K.; Ohmi, N.; Murakami, Y.; Shibayama, M.; Konishi, Y.; Kimura, T. Measurements of reflection and transmission characteristics of interior structures of office building in the 60-GHz band. IEEE Trans. Antennas Propag. 45: 1783–1792; 1997.

[260] Sagnard, F.; Vignat, C.; Montcourtois, V.; Rolland, E. Microwave measurements of the complex permittivity of construction materials using Fresnel reflection coefficients

and reflection ellipsometry. 2001 IEEE International Symposium Antennas Propag. Society, 1: 626–629; 2001.

[261] Cuinas, I.; Sanchez, M. G.; Rodriguez, F. G. Normal-incidence transmission of radio waves through building materials in the 5.8 GHz frequency band. Microwave Opt. Techn. Lett. 23: 7–12; 1999.

[262] Taylor, C. D.; Gutierrez, S. J.; Langdon, S. L.; Murphy, K. L. On the propagation of RF into a building constructed of cinder block over the frequency range 200 MHz to 3 GHz. IEEE Trans. Electromagn. Compat. 41: 46–49; 1999.

[263] Cuinas, I.; Sanchez, M. G. Permittivity and conductivity measurements of building materials at 5.8 GHz and 41.5 GHz. Wireless Per. Commun., 20: 93–100; 2002.

[264] Gibson, T. B.; Jenn, D. C. Prediction and measurement of wall insertion loss. IEEE Trans. Antennas Propag. 47: 55–57; 1999.

[265] Poon, L.-S.; Wang, H.-S. Propagation characteristic measurement and frequency reuse planning in an office building. Proc.IEEE 44th Vehicular Technology Conf., 3: 1807–1810; 1994.

[266] Vogel, W. J.; Torrence, G. W. Propagation measurements for satellite radio reception inside of buildings. IEEE Trans. Antennas Propag. 41: 954–961; 1993.

[267] Lee, D. J. Y.; Lee, W. C. Y. Propagation prediction in and through buildings. IEEE Trans. Vehicular Technol. 49: 1529–1533; 2000.

[268] Frazier, L. M. Radar surveillance through solid materials. Proc. SPIE, The International Society for Optical Engineering 2938: 139–146; 1996.

[269] Ju, K. M.; Chiang, C. C.; Liaw, H. S.; Her, S. L. Radio propagation in office buildings at 1.8 GHz. PIMRC'96., Seventh Proc. IEEE Int. Symp. Personal, Indoor and Mobile Radio Communications, 1996. 3: 766–770; 1996.

[270] Correia, L. M.; Frances, P. O. Transmission and isolation of signals in buildings at 60 GHz. , Sixth IEEE Int. Symp. Personal, Indoor and Mobile Radio Communications, 1995. PIMRC'95. 'Wireless: Merging onto the Information Superhighway'.3: 1031–1034; 1995.

[271] Robert, A. Dielectric permittivity of concrete between 50 MHz and 1 GHz and GPR measurements for building materials. J. Appl. Geophys. 40: 89–94; 1998.

[272] Jean, J.Ho. Design of low dielectric glass+ceramics for multilayer ceramic substrates. IEEE Trans. Comp. Pkg. Mfg. Technol.: Part B 17: 228–233; 1994.

[273] Neelakanta, P. Electromagnetic Materials. London: CRC Press; 1995.

A. Review of the Literature on Dielectric Measurements of Lossy Materials

In this section we briefly overview the existing literature on dielectric and magnetic material measurements of a wide variety of lossy materials. General references include the databases at the Center for Information and Numerical Data Synthesis Analysis (CINDAS) and Microelectronics Packaging Materials Database [139]. Both of these databases compile dielectric measurement results on a large number of materials.

For the interested reader we cite various references to material measurements below. We have included the most robust studies for which we have the most familiarity and concentrated on sources that include uncertainties.

- Measurements on concrete, rock, and asphalt are given in References [79, 140–160]. Figures 55 to 58 include measurements we performed on concrete and mortar with a shielded-open-circuited holder.

- Measurements on plastics are given in References [9, 161–172].

- Measurements of organic materials such as wood depend strongly on the water content. Measurements on various types of wood are given in References [173, 174]. Dielectric
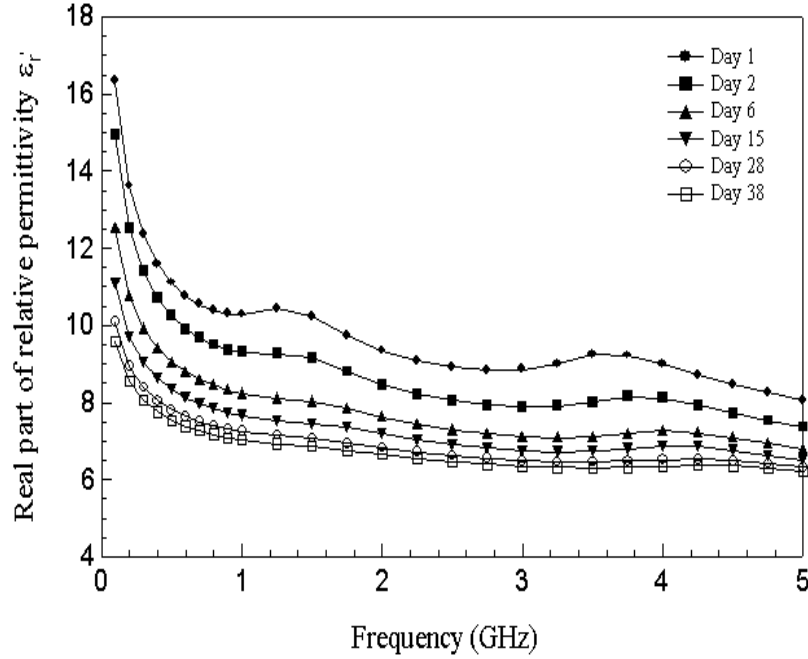
136

Figure 55. The real part of the permittivity for (5000 PSI) concrete as a function of cure time.

properties of wood, as a function of moisture content, are given below.

- Many measurements on building material and in-door reflection data are given in References [79, 175, 176, 259].

- Dielectric properties of grains and food products are given in [177–179]. Dielectric properties of some foods are summarized in References [180–184].

- Dielectric properties of meat are given in References [185].

- The dielectric properties of various liquids are given in References [3, 100, 117, 118, 137, 186–197].

- Ground-penetrating radar methods and measurements are summarized in References [77–83, 142, 198].

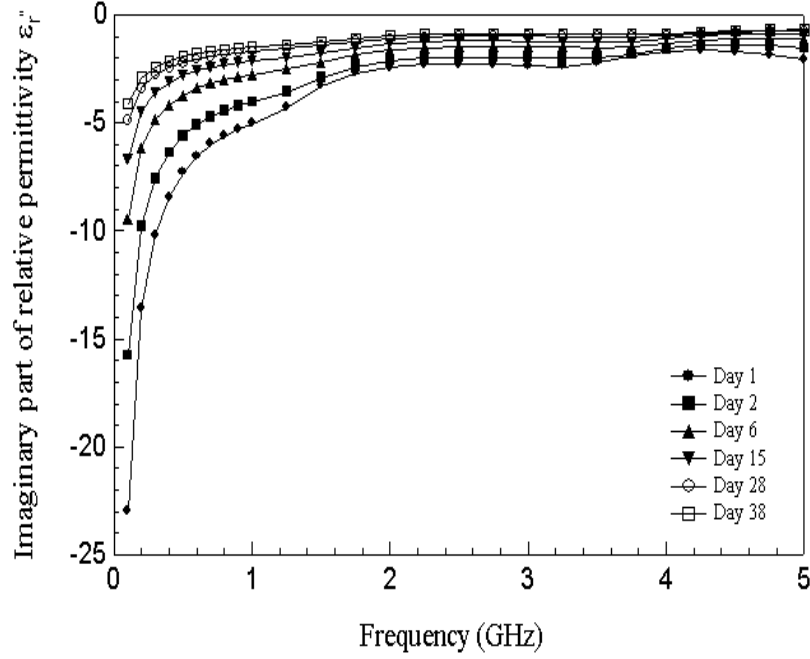- Nondestructive techniques are summarized in References [199–207].

Figure 56. The imaginary part of the permittivity for (5000 PSI) concrete as a function of cure time.

- Dielectric measurements on deionized water are given in References [208–215]. Water is commonly modeled by a Debye curve. For frequencies below 100 GHz we can use [208]:

$$\epsilon_r^* = \epsilon_\infty + \frac{\epsilon_s - \epsilon_\infty}{1 - i\frac{f}{\gamma_D}}, \tag{236}$$

where f is in GHz, $\gamma_D = 20.27 + 146.5\theta + 314\theta^2$, $\theta = 1 - 300/(273.15 + T)$, $\epsilon_s = 77.66 - 103.3\theta$, $\epsilon_\infty = 0.066\epsilon_s$.

- Measurements on salt water are given in References [216–219].

- Measurements on ice are given in Reference [220]. The real part of the permittivity is approximately $\epsilon_r' = 3.15$. The loss factor is shown to be

$$\epsilon_r'' = 6.14 \times 10^{-5} F(1.118(\theta + 1)) f_G, \tag{237}$$

where f_G is the frequency in gigahertz and $F = xe^x/(e^x - 1)^2$, $\theta = 300/(273.15 + T_c) - 1$, where T_c is the Celsius temperature.
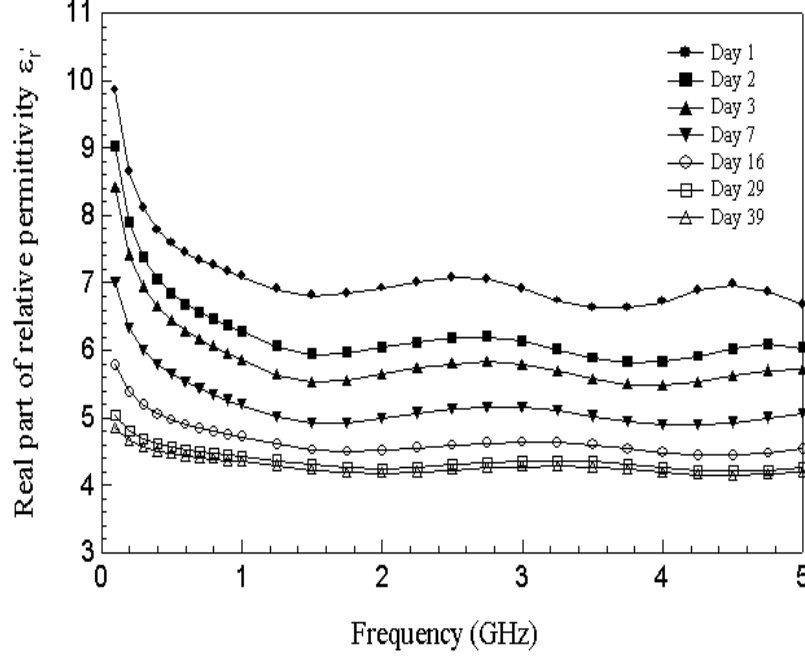
138

Figure 57. The real part of the permittivity for mortar cement as a function of cure time.

- Dielectric measurements of snow are summarized in Reference [221]. The permittivity of snow depends on the density. From the data of Hallikainen at al. Reference [221] we can fit the permittivity of snow at 10 GHz as a function of density:

$$\epsilon_r' = 1 + 1.2(\rho_s/1000) + 1.2(\rho/1000)_s^2, \tag{238}$$

where the density is in kg/m^3. The loss factor at 18 GHz is modeled as

$$\epsilon_r'' = 15.5 m_w, \tag{239}$$

where m_w is the percent liquid water content; in these formulas m_w ranges from 0 to 16.

- Soils have been measured by many researchers as functions of organic, sand, clay and water content [222–232]. Although soils vary by the amount of moisture, loom, sand, and clay the variation of a *typical soil* as a function of the percent of volumetric moisture content (P_m) has been fit by Reference [232] at 78 MHz and at 20 ^{0}C as

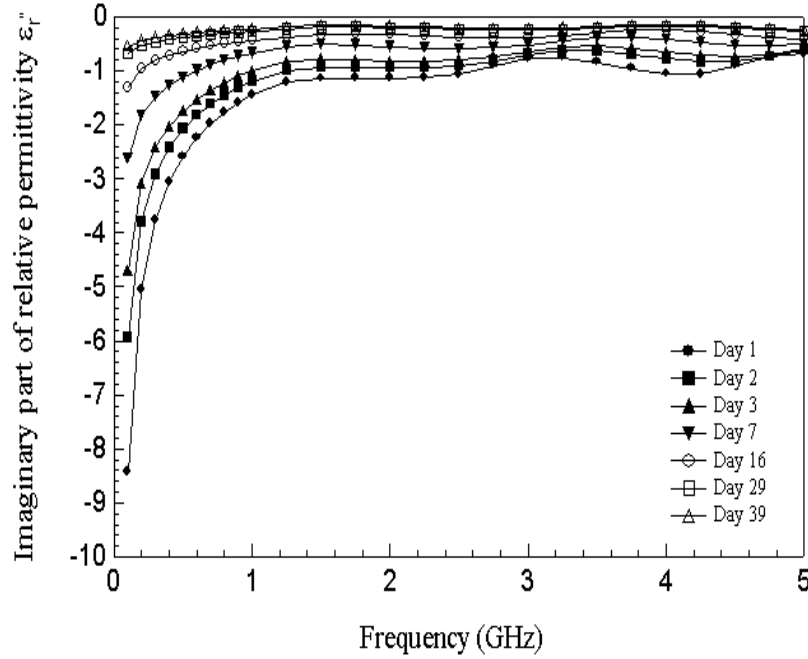$$\epsilon_r' = 0.00189 P_m^2 + 0.690 P_m + 0.3. \tag{240}$$

Figure 58. The imaginary part of the permittivity for concrete as a function of cure time.

- Dielectric properties of oil shale and char have been characterized by a number of authors in References [233–238]. Dielectric measurements of coal are given in [239].

- Measurements on biological phantoms are summarized in References [124–132, 240].

- Measurements of biological tissues, DNA, proteins, and reference liquids are summarized in References

  [115, 123, 241–243].

- Dielectric properties of composites and building materials are summarized in References [176, 244–258, 260–270].

The dielectric properties of various building materials were measured by our group and reported in Table 15

Kind of wood	dry wood		moist wood		
	$\varepsilon_{r'}$	tanδ	content of water	ε_r	tanδ
Beech	1.888	2.6E-02	9.5%	2.536	1.5E-01
Ash	2.045	3.2E-02	10.2%	2.901	1.5E-01
Walnut	1.854	3.0E-02	10.1%	2.486	1.4E-01
Mahogany	1.830	2.9E-02	10.9%	2.520	1.8E-01
Sycamore	1.885	3.0E-02	10.3%	2.547	1.8E-01
Birch	2.072	3.5E-02	10.3%	2.860	1.8E-01
Pine	1.721	2.9E-02	10.5%	2.211	1.3E-01
Alder	1.900	3.3E-02	11.6%	2.510	1.5E-01
Oak	1.962	3.5E-02	10.8%	2.584	1.5E-01
Cherry	1.954	3.6E-02	9.8%	2.697	1.5E-01

Figure 59. The permittivity of various types of wood at 3.6 GHz (Krupka personal communication 2004).

B. Gap Correction in Dielectric Materials

B.1 Coaxial Capacitor Model for Dielectric Materials

Consider a capacitor consisting of layers of dielectric and layers of air in a coaxial line [59]. The dimensions are shown in Figure 60. We treat the system as capacitors in series, so

$$\frac{1}{C_m} = \frac{1}{C_1} + \frac{1}{C_2} + \frac{1}{C_3}. \tag{241}$$

We know that for a coaxial line the radial electric field distribution is given by

$$E_r = \frac{V}{\ln(\frac{b}{a})r}, \tag{242}$$

and the potential difference between the conductors is given by

$$V = -\int_a^b E(r)dr. \tag{243}$$

The capacitance of a coaxial line of length L is given by

$$C = \frac{2\pi\epsilon L}{\ln\frac{R_2}{R_1}}; \tag{244}$$

141

Table 15. Dielectric measurements on various building materials between 700 MHz and 10 GHz.

Material	Freq.(GHz)	Temp.(C)	ϵ'_r	$\tan\delta$	Method	Density(g/cc)
White marble	1.42	22 ± 0.5	8.64	5.44×10^{-4}	SPR	2.68
Stained ceramic tile	1.44	22 ± 0.5	3.52	2.52×10^{-3}	SPR	1.65
White marble	2.02	22 ± 0.5	8.63	5.09×10^{-4}	SPR	2.68
Stained ceramic tile	2.04	22 ± 0.5	3.50	2.54×10^{-3}	SPR	1.65
Green granite	2.03	22 ± 0.5	7.75	1.44×10^{-2}	SPR	3.02
White marble	3.21	22 ± 0.5	8.61	5.99×10^{-4}	SPR	2.68
Stained ceramic tile	3.31	22 ± 0.5	3.56	2.82×10^{-3}	SPR	1.65
Green granite	3.31	22 ± 0.5	7.76	1.93×10^{-2}	SPR	3.02
White marble	5.44	22 ± 0.5	8.51	1.13×10^{-3}	SPR	2.68
Stained ceramic tile	5.50	22 ± 0.5	3.24	3.78×10^{-3}	SPR	1.65
Green granite	5.39	22 ± 0.5	6.92	1.92×10^{-2}	SPR	3.02
White marble	9.59	22 ± 0.5	8.56	1.05×10^{-3}	SPR	2.68
Stained ceramic tile	9.81	22 ± 0.5	3.24	3.77×10^{-3}	SPR	1.65
Glazed tile	9.80	22 ± 0.5	5.28	7.92×10^{-3}	SPR	
Unglazed tile	9.90	22 ± 0.5	3.79	4.11×10^{-3}	SPR	
Green granite	9.41	22 ± 0.5	6.90	1.46×10^{-2}	SPR	3.02
Red brick	9.56	22 ± 0.5	10.78	4.95×10^{-3}	SPR	
Dry pine wood	1.46	22 ± 0.5	1.84	9.11×10^{-2}	SPR	
Linoleum tile	0.71	22 ± 0.5	5.93	3.96×10^{-3}	SPR	
Asphalt shingle	0.71	22 ± 0.5	3.64	2.01×10^{-2}	SPR	
Plywood	0.71	22 ± 0.5	2.91	1.08×10^{-1}	SPR	
Gypsum board	0.71	22 ± 0.5	2.81	1.89×10^{-2}	SPR	

thus, for a system of three capacitors in series we have

$$\frac{\ln\frac{R_4}{R_1}}{\epsilon'_{rm}} = \frac{\ln\frac{R_2}{R_1}}{\epsilon'_{r1}} + \frac{\ln\frac{R_3}{R_2}}{\epsilon'_{rc}} + \frac{\ln\frac{R_4}{R_3}}{\epsilon'_{r1}}, \tag{245}$$

where $\epsilon'_{rc}, \epsilon'_{rm}$ are the relative corrected and measured values of the real part of the permittivity and ϵ'_{r1} is the real part of the permittivity of the air gap. The corrected permittivities are

$$\epsilon'_{rc} = \frac{\ln\left(\frac{R_4}{R_1}\right)\epsilon_{rg}(1+\tan^2\delta_{ig}) - \ln\left(\frac{R_4 R_2}{R_3 R_1}\right)\epsilon_{rm}(1+\tan^2\delta_{im})}{(\ln\left(\frac{R_3}{R_2}\right))(1+\tan^2\delta_{ig})(1+\tan^2\delta_{im})\left(\frac{\ln\left(\frac{R_4}{R_1}\right)^2\epsilon_{rg}}{(\ln\left(\frac{R_3}{R_2}\right))^2\epsilon_{rm}(1+\tan^2\delta_{im})} + \frac{\ln\left(\frac{R_4 R_2}{R_3 R_1}\right)^2\epsilon_{rm}}{(\ln\left(\frac{R_3}{R_2}\right))^2\epsilon_{rg}(1+\tan^2\delta_{ig})}\right)}. \tag{246}$$
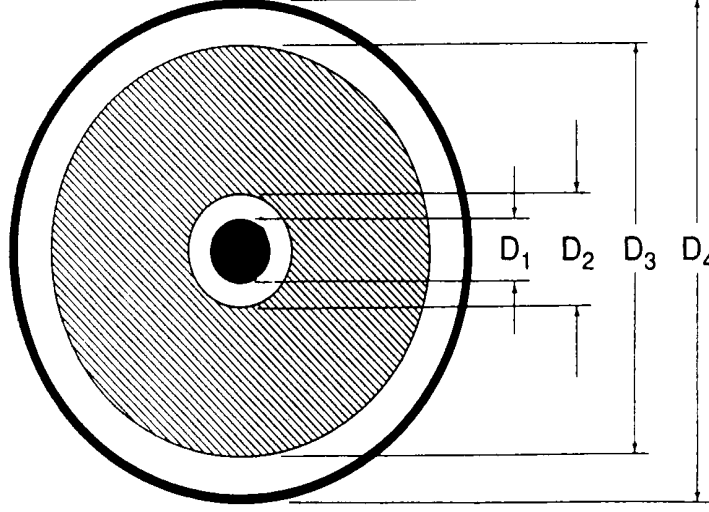
Figure 60. A coaxial specimen in holder with air gaps near conductors with diameters denoted by D_i.

The corrected imaginary part is

$$\epsilon'_{ic} = \epsilon_{rc}\tan\delta_{ic} = \frac{-\ln\left(\frac{R_4}{R_1}\right)\epsilon_{rg}(1+\tan^2\delta_{ig})\tan\delta_{im} + \ln\left(\frac{R_4 R_2}{R_3 R_1}\right)\epsilon_{rm}(1+\tan^2\delta_{im})\tan\delta_{ig}}{\left(\ln\left(\frac{R_3}{R_2}\right)\right)(1+\tan^2\delta_{ig})(1+\tan^2\delta_{im})\left(\frac{\ln\left(\frac{R_4}{R_1}\right)^2\epsilon_{rg}}{(\ln\left(\frac{R_3}{R_2}\right))^2\epsilon_{rm}(1+\tan^2\delta_{im})} + \frac{\ln\left(\frac{R_4 R_2}{R_3 R_1}\right)^2\epsilon_{rm}}{(\ln\left(\frac{R_3}{R_2}\right))^2\epsilon_{rg}(1+\tan^2\delta_{ig})}\right)}. \tag{247}$$

An approximate expression is given by

$$\epsilon'_{rc} = \epsilon'_{mr}\frac{L_2}{L_3 - \epsilon'_{rm}L_1}, \tag{248}$$

$$\tan\delta_c = \tan\delta_m[1 + \epsilon'_{rm}\frac{L_1}{L_2}], \tag{249}$$

where

$$L_1 = \ln\frac{R_2}{R_1} + \ln\frac{R_4}{R_3}, \tag{250}$$

$$L_2 = \ln\frac{R_3}{R_2}, \tag{251}$$

$$L_3 = \ln\frac{R_4}{R_1}. \tag{252}$$

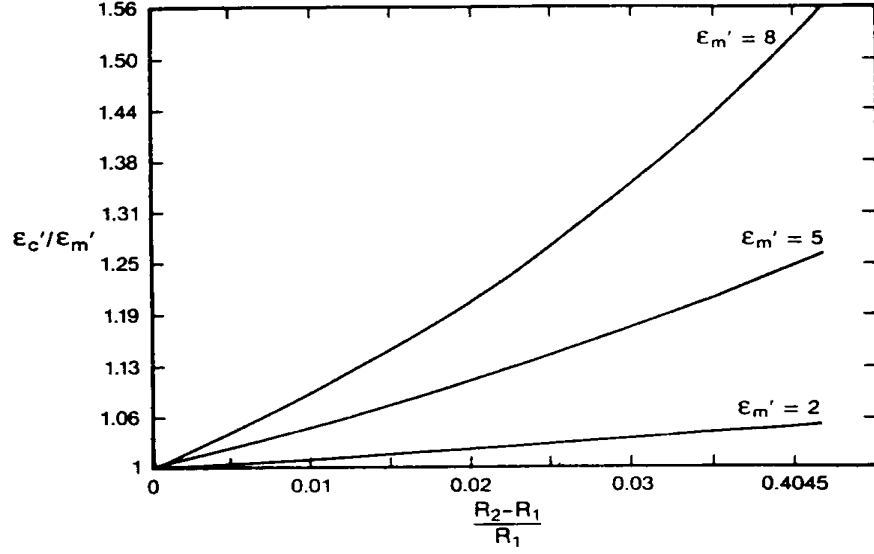Equation (248) breaks down when $\epsilon'_{rm} \geq L_3/L_1$. Correction data are shown in Figure 61.

Figure 61. The gap correction calculated for various values of ϵ_r', where R_2, R_1 are the radii of the inner conductor and specimen, respectively.

B.2   Rectangular Waveguide Model

In rectangular waveguide the electric field has two components. The first component E_x is across the thin dimension and is sensitive to gaps at the sample-waveguide interface. The H_z component has a discontinuity at the sample-air interface. This causes an increased sensitivity to sample-length errors. For the case of a rectangular guide of narrow dimension b with specimen thickness $b - w$ and air gap width w(see Figure 62),

$$\epsilon_{rc} = \frac{b\epsilon_{rg}(1 + \tan^2\delta_{ig}) - w\epsilon_{rm}(1 + \tan^2\delta_{im})}{(b-w)(1 + \tan^2\delta_{ig})(1 + \tan^2\delta_{im})(\frac{b^2\epsilon_{rg}}{(b-w)^2\epsilon_{rm}(1+\tan^2\delta_{im})} + \frac{w^2\epsilon_{rm}}{(b-w)^2\epsilon_{rg}(1+\tan^2\delta_{ig})})} \tag{253}$$

$$\epsilon_{ic} = \epsilon_{ic}\tan\delta_{rc} = \frac{-b\epsilon_{rg}(1 + \tan^2\delta_{ig})\tan\delta_{im} + w\epsilon_{rm}(1 + \tan^2\delta_{im})\tan\delta_{ig}}{(b-w)(1 + \tan^2\delta_{ig})(1 + \tan^2\delta_{im})(\frac{b^2\epsilon_{rg}}{(b-w)^2\epsilon_{rm}(1+\tan^2\delta_{im})} + \frac{w^2\epsilon_{rm}}{(b-w)^2\epsilon_{rg}(1+\tan^2\delta_{ig})})}$$
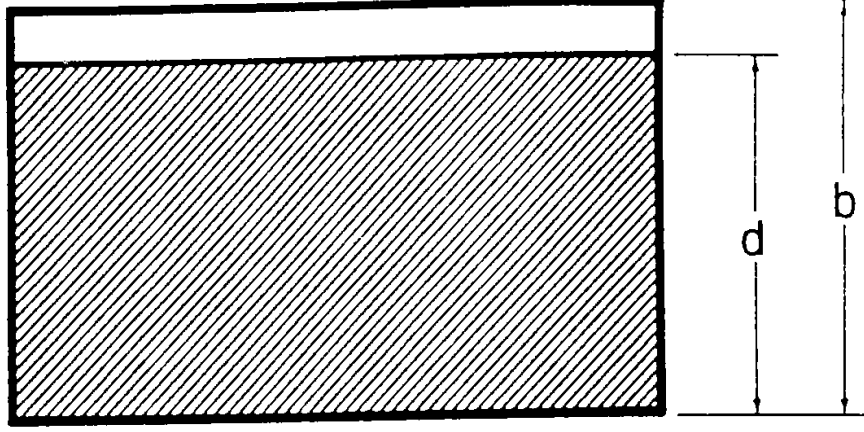$$\tag{254}$$

144

Figure 62. specimen in rectangular waveguide.

C.   Gap Correction for Magnetic Materials

C.1   Coaxial Capacitor Model for Magnetic Materials

For the calculation of the gap correction for the permeability a pure inductance model is useful. We model the transmission line as a series of inductors for the E-field gap

$$\mathcal{L}_m = \mathcal{L}_c + \mathcal{L}_{air}, \tag{255}$$

where c, m, and air denote corrected value, measured value, and air space. Therefore the corrected value is

$$\mathcal{L}_c = \mathcal{L}_m - \mathcal{L}_{air}. \tag{256}$$

The inductance is the flux penetrating the circuit divided by the current flowing in the circuit

$$\mathcal{L} = \frac{\phi}{I}, \tag{257}$$

where

$$\phi = \int \vec{B} \cdot d\vec{S}. \tag{258}$$

Ampere's law gives

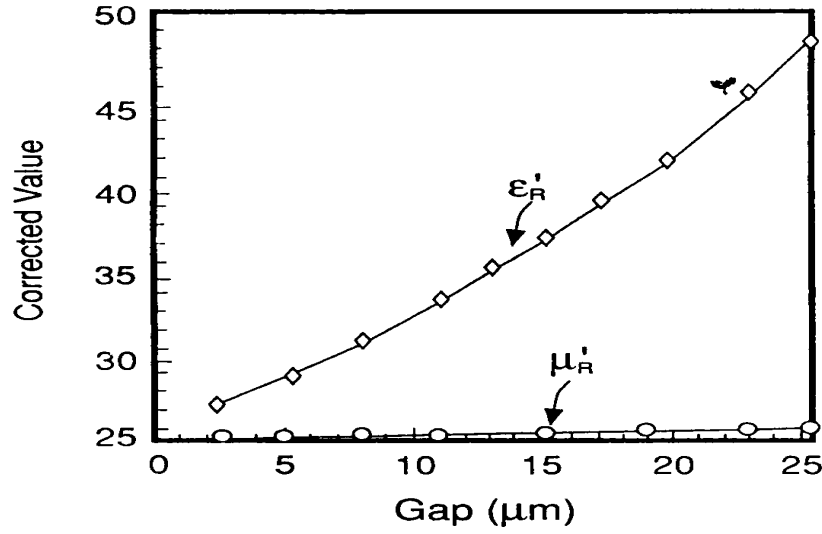$$\int \mathbf{H} \cdot d\vec{l} = I, \tag{259}$$

145

Figure 63. Corrected permeability and permittivity as a function of inner conductor gap for a 7 mm specimen. The gap around the outer conductor is assumed to be zero. In this case the uncorrected (measured) value was $\mu'_r = 25$, $\epsilon'_r = 25$.

which yields

$$B_\phi = \frac{\mu' I}{2\pi r}. \tag{260}$$

Therefore

$$\phi = \frac{1}{2\pi} \mu' I \ln b/a, \tag{261}$$

so

$$\mathcal{L} = \frac{1}{2\pi} \mu' \ln b/a. \tag{262}$$

Therefore we can write for the corrected permeability

$$\mu'_{cR} = \frac{\mu'_{mR} \ln R_4/R_1 - [\ln R_2/R_1 + \ln R_4/R_3]}{\ln R_3/R_2}, \tag{263}$$

$$\mu''_{cR} = \mu''_{mR} \frac{\ln(R_4/R_1)}{\ln(R_3/R_2)}. \tag{264}$$

Gap correction data are given in Figure 63. The corrections for permeability in coaxial line are much less than for permittivity. This is due to the fact the azimuthal magnetic field is continuous across the discontinuity, whereas the radial electric field is discontinuous across the discontinuity.
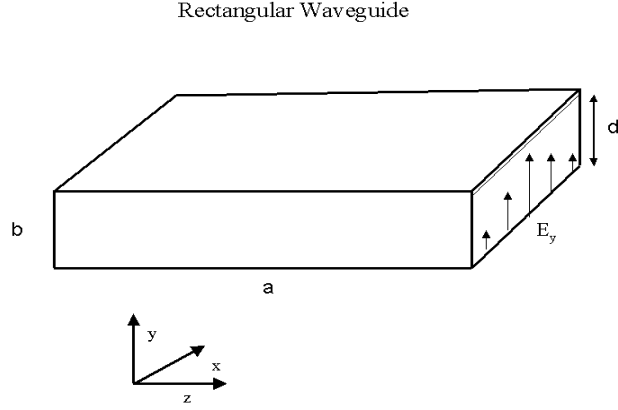
146

Rectangular Waveguide

Figure 64. Rectangular waveguide.

$$. \tag{265}$$

C.2 Waveguide Model for Magnetic Materials

The TE$_{10}$ fields is rectangular waveguide are

$$E_y = -\frac{i\omega a}{\pi} H_0 \sin\frac{\pi x}{a}, \tag{266}$$

$$H_x = \frac{ik\omega a\mu}{\pi} H_0 \sin\frac{\pi x}{a}, \tag{267}$$

$$H_z = H_0 \cos\frac{\pi x}{a}. \tag{268}$$

By looking at the fields we see that the electric field is perpendicular to the X-Y plane and therefore the permittivity is strongly influenced by the gap. The magnetic fields go to zero at the Y-Z and X-Z planes, so the correction for permeability should not be large unless there are significant gaps. For magnetic materials, the z component of the magnetic field is discontinuous across the sample faces. Therefore we expect a strong dependence of uncertainty in sample length on the uncertainty in permeability.

147

C.3 Magnetic Corrections for Gaps in the X-Z and Y-Z Planes

For magnetic materials in waveguide for the TE_{10} mode, gaps in the X-Z plane are not severe because the magnetic field circles around, and is tangential to small gaps (as shown in Figure 64). The corrections can be obtained using inductances in series. These are

$$\mu'_{cR} = \mu'_{mR}\left(\frac{b}{d}\right) - \left(\frac{b-d}{d}\right), \tag{269}$$

$$\mu''_{cR} = \mu''_{mR}\left(\frac{b}{d}\right). \tag{270}$$

C.4 Magnetic Corrections for Gaps Across the X-Y Plane

These corrections can be obtained using inductances in parallel. As a result, uncertainties in the sample length can be amplified because of the discontinuity in the permeability from the sample to air. These corrections for permeability would be of the same form as for the electric-field correction in the previous section.

C.4.1 Mitigation of the Effects of Air Gaps

We can minimize the effects of air gaps by placing a conducting material in the air gap. This material may be a conducting paint or a conducting grease. The conducting material will change the line impedance and line loss to a degree. However, for relatively small gaps, the improvements in dielectric and magnetic property measurements far outweigh any changes in the line impedance. The loss measurement will be influenced by this procedure. The effects of gaps in the X-Z plane on the permittivity can be reduced if the gap is filled with a of low-loss material with a high-permittivity. This works since the gap correction acts as capacitances in series.

D. Permittivity and Permeability Mixture Equations

Many lossy materials can be fit with a modified Debye response

$$\epsilon^*(\omega) = \epsilon_\infty + \frac{\epsilon_s - \epsilon_\infty}{1 + (i\omega\tau)^{1-\alpha}} - i\frac{\sigma_{dc}}{\omega\epsilon_0}, \tag{271}$$

148

ϵ_∞ is the optical permittivity, ϵ_s is the static permittivity, and τ is the relaxation time. If $\alpha = 0$, then the response is Debye with dc conductivity and if $\alpha \neq 0$ it is a Cole-Cole response. Robert [271] has shown that Cole-Cole fits the relaxation data of concrete data very well.

We can readily estimate the permittivity of a mixture of a number of distinct materials. The effective permittivity of a mixture ϵ_{eff} of constituents with permittivity ϵ_i and volume fractions θ_i can be approximated in various ways. For an arbitrary number of constituents the following mixture equations apply [272]:

$$\frac{\epsilon'_{eff} - \epsilon'_1}{3\epsilon'_1} = \frac{\theta(\epsilon'_2 - \epsilon'_1)}{(\epsilon'_2 + 2\epsilon'_1)}. \tag{272}$$

The Bruggeman equation [273] is useful for binary mixtures:

$$\theta_1 \frac{\epsilon'_{eff} - \epsilon'_1}{\epsilon'_1 + 2\epsilon'_{eff}} = \theta_2 \frac{\epsilon'_2 - \epsilon'_{eff}}{\epsilon'_2 + 2\epsilon'_{eff}}, \tag{273}$$

or the Maxwell-Garnett mixture equation [273] can be used:

$$\frac{\epsilon'_{eff} - \epsilon'_2}{\epsilon'_{eff} + 2\epsilon'_2} = \theta_1 \frac{\epsilon'_1 - \epsilon'_2}{\epsilon'_1 + 2\epsilon'_2}, \tag{274}$$

where ϵ'_1 is the permittivity of the matrix and ϵ'_2 is the permittivity of the filler [246].

Over the years a number of phenomenological equations have been developed to model liquids with permanent dipole moments. One of the most general of these is the Havriliak-Negami equation [18]

$$\epsilon^*_r = \epsilon_\infty + \frac{\epsilon_s - \epsilon_\infty}{[1 + (j\omega\tau)^{1-\alpha}]^\beta}. \tag{275}$$

In the special case where $\alpha = 0$, $\beta = 1$, the classical Debye distribution is obtained. The Cole-Cole distribution is obtain when $\beta = 1$. The Cole-Davidson model is obtained when $\alpha = 0$. In the cases of the Cole-Cole and Debye models, if ϵ'_r is plotted versus ϵ''_r a semicircle is realized. Cole-Cole plots can be very informative for many liquids. Since we know that to a very good approximation many liquids are described by this model, we can use the distribution to extrapolate dc permittivity, thereby minimizing electrode-polarization effects.